Structure, Adsorption Mechanisms, and Vibrational Exciton Formation at Proxy Marine Interfaces

DISSERTATION

Presented in Partial Fulfillment of the Requirements for the Degree Doctor of Philosophy in the Graduate School of The Ohio State University

By

Kimberly A. Carter-Fenk, M.S.

Graduate Program in Chemistry

The Ohio State University

2021

Dissertation Committee:

Prof. Dr. Heather C. Allen, Advisor

Prof. Dr. Bern Kohler

Prof. Dr. Sherwin J. Singer

Prof. Dr. Donald Y. Yau

Abstract

Marine aqueous interfaces constitute one of the most prevalent surfaces in the biosphere and the atmosphere, and understanding the physicochemical processes at these interfaces is of significant importance for informing Earth system models. In the following chapters, surfactant organization and morphology on aqueous solutions of high ionic strength are explored as a proxy for the organic films coating sea spray aerosol (SSA) surfaces and the sea surface microlayer (SSML). First, a proxy film mixture comprised of the saturated fatty acids myristic acid (C_{14}), palmitic acid (C_{16}), and stearic acid (C_{18}) was selected to study sea spray aerosol film morphology as a function of atmospheric acidification. The nascent SSA proxy film is fluid and flexible, whereas the acidified film is more rigid; as a result, the nascent SSA proxy film folds upon collapse, and the acidified film fractionates into three-dimensional structures with compression. Next, the influence of surfactant organization on one-dimensional surface-sensitive infrared spectroscopy was examined. Decreasing intermolecular distances between a soluble perfluorooctanoic acid film and an insoluble arachidic acid (C_{20}) monolayer cause vibrational exciton delocalization across the surfactants, manifesting in alkyl and fluoroalkyl signal reduction and deviations from the Beer-Lambert law. The aqueous electrolyte composition in part modulates surfactant intermolecular spacing, affecting the extent of vibrational delocalization. Consequently, quantitative analyses involving alkyl and fluoroalkyl one-dimensional vibrational peak intensities must be approached with caution. Lastly, surfactant-mediated cooperative adsorption of a soluble polysaccharide to a proxy sea surface microlayer is studied. Seawater

divalent cations facilitate ionic bridges between the marine-relevant, anionic polysaccharide alginate and a partially deprotonated palmitic acid monolayer. Calcium promotes the strongest bridging interactions, and palmitic acid headgroup protonation blocks alginate co-adsorption. This work characterizes a potentially important mechanism driving polysaccharide enrichment in the SSML, and thus, in SSA.

Dedication

To Kevin and Penelope

In loving memory of Patch

Acknowledgements

Graduate school often felt like a solitary effort, but in reality that was never the case. My spouse Kevin Carter-Fenk is largely the reason that I even finished this dissertation in the first place. He offered innumerable helpful insights on my projects, and Chapter 4 of this dissertation is the result of one of our conversations. Kevin shouldered extra responsibilities around the house when I had migraines, and he has been an unending source of encouragement and support throughout graduate school. I would like to thank my family for supporting me and my education. Through sending me food, holiday decorations, and doing my car maintenance and repairs, they helped me maintain a semblance of normal life. I would also like to thank Kevin's family for their encouragement and support and for providing a home away from home when Kevin and I needed a break. Additionally, I want to thank my good friends Olivia Clevenger, Dr. Danielle Spinden DeFiore, Sarah Cali, Madeline Lipkin, and Olivia Martinez-Murphy for the joy and encouragement they have brought to my life.

In the Allen lab, I would first like to thank my advisor, Dr. Heather Allen, for her mentorship and guidance throughout my graduate career. She gave me a considerable amount of freedom in my scientific pursuits, and I greatly enjoyed the opportunities to be creative and to follow my interests. I am immensely grateful for the efforts of an incredibly talented team of undergraduate researchers: Michelle Fiamingo, Jeongin Kim, and Audrey Milligan. They motivated and inspired me even when projects weren't going well, and they pushed me into new and exciting directions. I would like to thank all members of the Allen lab, past and present, for their uplifting en-

ergy, insightful conversations, and comradery throughout this process. Ka Chon Ng volunteered to train me on the SHG when I needed some last-second measurements for a reviewer; and he, Tehseen Adel, Dr. Stephen Baumler, Abbie Enders, and Dr. Jennifer Neal consistently performed invisible labor to help keep the lab running smoothly for everyone in the group. I am indebted to Mickey Rogers and Maria Vazquez de Vasquez for their friendship, support, and help throughout my graduate career. Mickey would often stay with me during late-night lab sessions and bring me treats, and she made the difficult parts of graduate school much less arduous.

I received extensive support and feedback through the Center for Aerosol Impacts on Chemistry of the Environment (CAICE), and I would especially like to thank all of the CAICE students and postdoctoral researchers. I was also very lucky to make good friends and colleagues in Abigail Dommer and Liora Mael. Their friendship, collaboration, and pet photos/videos always brightened my day. Finally, I would like to thank all of my previous scientific mentors (in chronological order): the late Mr. Richard Koehler, Dr. Issmat Kassem, Dr. Gireesh Rajashekara, Dr. Daral Jackwood, Dr. Nicholas Shaw, Dr. Paul Bonvallet, and Dr. Paul Edmiston. I would not be here writing this section if it were not for their efforts and investment in my success as a student and as a researcher.

Vita

August 17, 1993	Born - Wooster, OH, USA
May 22, 2012	Triway High School, Wooster, OH, USA
May 16, 2016	B.A. Chemistry, The College of Wooster, Wooster, OH, USA
August 2016 - August 2017	GAANN Fellow, Department of Chemistry & Biochemistry, The Ohio State University, Columbus, OH, USA
August 2017 - Present	Graduate Research & Teaching Associate, Department of Chemistry & Biochemistry, The Ohio State University, Columbus, OH, USA
December 16, 2018	M.S. Chemistry, Department of Chemistry & Biochemistry, The Ohio State University, Columbus, OH, USA

Publications

Carter-Fenk, K. A.; Dommer, A. C.; Fiamingo, M. E.; Kim, J.; Amaro, R. E.; Allen, H. C. Calcium Bridging Drives Polysaccharide Co-Adsorption to a Proxy Sea Surface Microlayer. *ChemRxiv*, **2021**.

Carter-Fenk, K. A.; Carter-Fenk, K.; Fiamingo, M. E.; Allen, H. C.; Herbert, J. M. Infrared Hide-and-Seek: Vibrational Excitons Conceal Surfactants at the Air/Water Interface. *ChemRxiv*, **2020**.

Neal, J. F.; Rogers, M. M.; Smeltzer, M. A.; **Carter-Fenk, K. A.**; Grooms, A. J.; Zerkle, M. M.; Allen, H. C. Sodium Drives Interfacial Equilibria for Semi-Soluble Phosphoric and Phosphonic Acids of Model Sea Spray Aerosol Surfaces. *ACS Earth and Space Chemistry*, **2020**, *4*, 1549-1557.

Carter-Fenk, K. A.; Allen, H. C. Collapse Mechanisms of Nascent and Aged Sea Spray Aerosol Proxy Films. *Atmosphere*, **2018**, *12*, 1-16.

Edmiston, P. L.; **Carter, K. A.**; Graham, A. L.; Gleason, E. J. Chemisorption of Microcystins to a Thiol and Amine Functionalized Organosilica. *Separation and Purification Technology* **2018**, *197*, 244–252.

Field of Study

Major Field: Chemistry

Table of Contents

List of Figures

List of Tables

List of Abbreviations

Abbreviations

AA	Arachidic Acid
*ai*VEM	*ab initio* Vibrational Exciton Model
Alg	Alginate
AMOEBA	Atomic Multipole Optimized Energetics for Biomolecular Simulation
AU	Arbitrary Units
BAM	Brewster Angle Microscopy
BBO	Beta Barium Borate
BMS	Beam Splitter
CA	Cetyl Alcohol
CAICE	Center for Aerosol Impacts on Chemistry of the Environment
CCD	Charge-Coupled Device
CCN	Cloud Condensation Nuclei
CMC	Critical Micelle Concentration
DFT	Density Functional Theory
DMPC	1,2-Dimyristoyl-*sn*-glycero-3-phosphocholine
DOM	Dissolved Organic Matter
DPPA	1,2-Dipalmitoyl-sn-glycero-3-phosphatidic Acid
DPPE	1,2-Dipalmitoyl-phosphatidylethanolamine
EDF2	Empirical Density Functional 2
EDTA	Ethylenediaminetetraacetic Acid
EF	Enrichment Factor
FTIR	Fourier-Transform Infrared
FWHM	Full Width at Half Maximum
G	Gaseous
GL	Glan-Laser
G-TC	Gas-Tilted Condensed
HeNe	Helium-Neon
HWP	Half-Wave Plate
IN	Ice Nuclei
INP	Ice Nucleating Particle
IR	Infrared
IRRAS	Infrared Reflection-Absorption Spectroscopy
L	Lens

LE	Liquid Expanded
LPF	Long-Pass Filter
M	Mirror
MA	Myristic Acid
MBL	Marine Boundary Layer
MCT	Mercury Cadmium Telluride
MD	Molecular Dynamics
MMA	Mean Molecular Area
NDF	Neutral Density Filter
NSF	National Science Foundation
1D	1-Dimensional
PA	Palmitic Acid
PFAS	Perfluoroalkyl Substances
PFO	Perfluorooctanoate
PFOA	Perfluorooctanoic Acid
PFOS	Perfluorooctanesulfonic Acid
POM	Particulate Organic Matter
PTFE	Polytetrafluoroethylene
RA	Reflectance-Absorbance
RESPA	Reversible Reference System Propagator Algorithm
SA	Stearic Acid
SHG	Second Harmonic Generation
SP	Surface Pressure
SPF	Short-Pass Filter
SSA	Sea Spray Aerosol
SSML	Sea Surface Microlayer
SW	Seawater
TC	Tilted Condensed
TEP	Transparent Exopolymer Particles
3D	3-Dimensional
2D	2-Dimensional
UC	Untilted Condensed
VSFG	Vibrational Sum Frequency Generation

Chapter 1

Introduction

1.1 Chemistry in the Marine Boundary Layer

Oceans cover 71% of Earth's surface[1] and emit approximately 3.5×10^{12} kg of sea spray aerosol (SSA) per year into the marine boundary layer (MBL),[2] making the oceans one of the most significant sources of natural aerosol emissions on the planet. SSA acts as a shuttle for chemical exchange between the ocean and the atmosphere such that the matter within SSA can be deposited on land or elsewhere in the ocean. Chemical components within SSA are then transformed via reactivity with trace atmospheric gases and via photochemical reactions in the MBL.[3–5] SSA influence Earth's climate by changing atmospheric optical properties and albedo,[6–8] serving as cloud condensation nuclei[9–15] and ice nucleating particles,[16–23] and by providing a surface for heterogeneous chemical reactions.[5,24–28] Interfacial composition of SSA plays both a direct and indirect role in affecting climate, and the composition of nascent SSA is controlled by the interfacial composition of the air/sea interface.[29–33] Consequently, studying the physicochemical processes driving SSA interfacial composition is critically important for developing a better understanding of marine influences on climate.

SSA is formed via bubble bursting at the air/sea interface, also known as the sea

surface microlayer (SSML). The SSML constitutes a thin, gelatinous layer approximately 1-1,000 μm in depth.[34–36] Chemical composition of the SSML is different from that of the underlying seawater; surface-active organic matter adsorbs to the air/sea interface, and other soluble ions and organic matter are thought to interact with the insoluble organic molecules primarily through electrostatic interactions.[36–40] Breaking waves on the ocean surface entrain air into the water column, and these air bubbles scavenge dissolved organic matter (DOM) in seawater and in the SSML along the way back to the surface.[41] DOM adheres to the bubble surfaces and becomes incorporated into SSA upon bubble bursting.[42]

Size-fractionated SSA exhibits size-dependent trends in its composition. Broadly speaking, submicron fine SSA has a smaller O:C ratio while supermicron jet drop SSA has a larger O:C ratio. The differences in composition are due to the source of material from the bubble. Bubble bursting produces hundreds of film drops from the bubble film cap and a smaller number of jet drops from the cavity at the base of the bubble.[5,43] The film caps of bubbles are highly enriched in surface-active organic matter, whereas the composition at the bottom of the bubbles contains more water-soluble and particulate organic matter (POM).[5,44–47] Hence, film drops contain more water-insoluble organic compounds, and jet drops contain more water-soluble organic compounds.

Field measurements revealed that SSA particles are coated in surfactant films, and saturated medium- to long-chain fatty acids are the most abundant surfactants within these surface films.[48–50] Of the fatty acids, palmitic acid (C_{16}) is the most prevalent in both the SSML and in SSA (mostly $\leq$ 2.5 μm in diameter) due to its production in marine phytoplankton.[49,51,52] A laboratory mesocosm experiment also confirmed these field measurement results.[53] Saturated fatty acids between 8 and 24 carbons in length were the most abundant surfactants in the SSML and in SSA. In SSA with diameters $\leq$ 2.5 μm, the most prevalent fatty acids in order of decreasing

abundance were palmitic acid, stearic acid (C_{18}), myristic acid (C_{14}), and lauric acid (C_{12}). Palmitic acid and stearic acid constituted about two-thirds of the quantified fatty acids.

Anthropogenic surfactants are also highly enriched in the SSML and in SSA because of their large surface activities.[54–57] Perfluoroalkyl substances (PFAS) are of particular concern due to their ubiquity, environmental persistence, and detrimental impacts on human health.[58,59] Through laboratory experiments, PFAS enrichment factors (EFs) were quantified in SSA particles,

$$\text{Aerosol EF} = \frac{([X]/[\text{Na}^+]_{\text{SSA}})}{([X]/[\text{Na}^+]_{\text{SW}})} , \tag{1.1}$$

in which $[X]$ is the concentration of PFAS and $[\text{Na}^+]$ is the concentration of sodium cations in SSA and in seawater (SW).[60,61] The PFAS compounds tested were somewhat enriched in the SSML ($\text{EF} = 1.1 - 49$) and highly enriched in SSA, and PFAS enrichment increased with decreasing particle diameter. The two most abundant PFAS compounds, perfluorooctanoic acid (PFOA) and perfluorooctanesulfonic acid (PFOS), EFs of the largest (> 10.16 μm) and smallest ($0.029 - 0.99$ μm) SSA particles increased from $\sim 1,800$ to $\sim 17,100$ and from ~ 200 to $\sim 62,100$, respectively. Hydrocarbon fatty acids of comparable chain length exhibited submicron SSA EFs up to $\sim 1,000$,[62] indicating that PFAS are more surface-active than their hydrocarbon analogs. Recent studies have started to investigate PFAS competition with other natural surfactants at model SSML and SSA interfaces.[63,64] However, more work needs to be done to fully understand natural marine DOM impacts on PFAS EFs.

Monomolecular films comprised of a single type of insoluble surfactant have been studied most extensively,[65–69] but soluble compounds and large biomacromolecules in SSA have not been well-characterized. At the sea surface microlayer (SSML), polysaccharides can aggregate into nanometer- and micron-sized gels that influence the sea

surface microbial loop and the interfacial reactivity of the SSML.[70–74] Marine gels are three-dimensional polymer networks hydrated by seawater. Chemical or physical cross-links create the network, but a variety of factors influence the particular gel structure that is spontaneously assembled.[75] Covalently-linked gels generally cannot disperse, but gels that are interlinked via ionic and hydrophobic interactions are much more responsive to changes in chemical environment.[76] Marine gels are generally cross-linked by Ca^{2+} ion bonds with a random tangled topology, and this organization can be altered by changes in temperature and pH. Brewster angle microscopy reveals that filtered dissolved organic matter (DOM) less than or equal to 200-nm in size self-assembles following second-order kinetics.[70,77] Free polymeric DOM most likely reaches a critical concentration at the air-water interface, leading to polymer rafts that collapse into nanogels; these nanogels then diffuse into the bulk subphase and further aggregate to form microgels. Characterizing the organization, dynamic surface tension, and composition of these marine gels is particularly important for better prediction of their enrichment and reactivity in SSA.

Saccharides are particularly abundant in the MBL and comprise a large portion of DOM and POM in marine aerosol. Oligo- and polysaccharides are more abundant than monosaccharides, but the molecular assembly and speciation of these polymers in SSA is largely unknown.[78] Additionally, the chemical and structural transformations of oligo- and polysaccharides in the MBL is not understood. A previous field campaign in the North Atlantic and the Arctic measured tropospheric particle organic mass consisting of 68% and 37% carbohydrates, respectively.[79] A Pacific Ocean field campaign collected particles that consisted of a larger fraction in the submicron regime with higher organic mass fractions. The Pacific particles also contained more insoluble carbohydrates, indicative of marine POM. Arctic marine aerosol collected during this study mostly consisted of inorganic cuboid (sea salt) cores coated in carboxylic-acid containing polysaccharides, suggesting that the carbohydrates in the

Arctic particles most likely came from oceanic DOM.[80] While informative, these field studies lacked molecular specificity in regards to the precise monomer composition of the carbohydrates detected in the marine aerosol.

Laboratory mesocosm experiments have partially closed this gap in understanding of saccharide composition in marine aerosol.[78] Glucose was primarily found in the oligo- and polysaccharide form; galactose, mannose, xylose, fructose, arabinose, rhamnose, and ribose were only detected within sugar polymers. These sugars comprised 4-20% of the organic mass in fine SSA (diameter $\leq 2.5\mu$m), and 65% of the average saccharide mass was from glucose and galactose. A greater portion of the organic mass within coarse SSA (2.5-10 μm in diameter) was attributed to saccharides; however, only glucose, galactose, arabinose, rhamnose, and fucose monomers were detected. Arabinose, rhamnose, and fucose are structural saccharides characteristic of cell wall material, transparent exopolymer particles (TEP), and POM. Insoluble POM likely moves to the base of the bubble formed at the air-sea interface prior to bubble bursting. Consequently, POM is entrained in larger coarse SSA droplets. The saccharides in fine SSA, conversely, were characteristic of energy storage carbohydrates mostly found in marine DOC. Water soluble saccharides are hypothesized to adsorb to insoluble surfactants at the air-water interface. Therefore, the saccharides partitioned to the bubble film are transferred to fine SSA. Molecular interactions between the saccharides and other sea surface bubble organic material likely provides the mechanism through which different types of carbohydrates are distributed within various SSA size regimes. Thus, understanding the precise interaction and enrichment mechanisms is important for better predictions of SSA organic composition.

1.2 Motivation

Significant uncertainty remains in the representation of cloud and aerosol processes in global climate models.[81] This uncertainty arises from poor constraints on natural aerosol processes due to the lack of measurements prior to the Industrial Revolution.[82] Thus, in order to effectively characterize and predict anthropogenic influences on radiative forcing of climate, the contributions of natural aerosol in pristine environments must be parameterized. While we cannot go back in time to make these measurements, we can attempt to replicate a pristine environment in the laboratory.

The National Science Foundation Center for Aerosol Impacts on Chemistry of the Environment (NSF-CAICE) was established to fill this gap in our understanding of natural aerosol properties. This collaborative center combines the efforts of environmental scientists, physical and analytical chemists, and theoreticians to elucidate the fundamental physicochemical processes occurring in SSA. As a member of CAICE, I aim to characterize interfacial organization and adsorption processes responsible for organic enrichment in the SSML and in SSA. The choices of chemical systems studied are informed by measurements of laboratory-generated phytoplankton blooms collected by CAICE collaborators in a wave channel at Scripps Institution of Oceanography. This work combines surface science, spectroscopy, and computational chemistry to describe interfacial surfactant film organization at model marine aqueous interfaces. A polysaccharide adsorption mechanism is also studied in detail to better inform the physicochemical processes driving saccharide enrichment in SSA. The goal of these fundamental measurements of proxy marine surfaces is to inform Earth system model parameterization.[37,38,83–85]

1.3 Dissertation Highlights

Chapter 2 provides an introduction to the fundamental theory behind the experimental techniques used throughout this dissertation. A description of surface tensiometry, Brewster angle microscopy (BAM), infrared reflection-absorption spectroscopy (IRRAS), and second harmonic generation (SHG) spectroscopy is included as well.

Chapter 3 describes the morphology of a sea spray aerosol proxy film comprised of a mixture of the marine-abundant fatty acids myristic acid (MA), palmitic acid (PA), and stearic acid (SA) at the molar ratio of 3 SA:4 PA:2 MA. The SSA proxy film differs in phase behavior and monolayer collapse from that of its individual fatty acid components. Secondly, the proxy film exhibits intermediate rigidity at seawater pH and folds upon film compression, whereas at low pH the film becomes highly rigid and forms 3D nuclei upon monolayer collapse. Thus, subphase composition and pH play a significant role in modulating SSA film morphology, which in turn impacts SSA reflectivity in the atmosphere.

Chapter 4 describes the observation of vibrational exciton formation between soluble and insoluble surfactants at the air/water interface. Vibrational delocalization across a soluble perfluorooctanoic acid (PFOA) film and an insoluble arachidic acid (AA) monolayer was observed through deviations from Beer-Lambert behavior with decreasing average intermolecular distances between surfactants. Aqueous subphase electrolyte composition modulates surfactant intermolecular distance, thereby affecting the extent of vibrational delocalization across the interfacial film. Theoretical PFOA IRRAS spectra obtained through molecular dynamics simulations and vibrational exciton calculations agree nearly quantitatively with experiment. Consequently, quantitative analyses of 1D vibrational mode peak intensities at the air/water interface must be approached with caution due to vibrational delocalization promoted by the surface.

Chapter 5 describes a mechanism through which the marine-relevant, anionic

polysaccharide alginate cooperatively adsorbs to a proxy SSML aqueous interface comprised of an insoluble palmitic acid monolayer. Divalent cations from seawater facilitate ionic bridges between the fatty acid and alginate carboxylate moieties. Of the seawater divalent cations, Ca^{2+} promotes the strongest bridging interactions, whereas Mg^{2+} only weakly bridges the alginate and monolayer headgroups due to the strong Mg^{2+} hydration shell. Palmitic acid protonation breaks apart the bridging interactions, and Na^{+} does not facilitate alginate co-adsorption. Consequently, a physical explanation for polysaccharide enrichment in SSA is elucidated, and the results provide potentially useful parameters for Earth system models.

Chapter 2

Theory and Instrumentation

2.1 Interfacial Phenomena

Surfactant films at aqueous surfaces are the primary focus of this dissertation. As such, an overview of the chemistry and physics of surfactant films and the adsorption models used in later chapters will be presented. Influence of the aqueous electrolyte composition on the properties of interfacial films will also be discussed.

2.1.1 Surface Tension

Attractive intermolecular interactions decrease the potential energy of molecules, thereby leading to molecules within a condensed phase medium being spaced such that the potential energy is minimized.[86,87] However, at the liquid/vapor interface, there are fewer neighboring molecules in the gaseous phase (Fig. 2.1). Consequently, interfacial molecules are higher in energy than their bulk counterparts. Work W must be carried out to bring a molecule from the bulk to the surface and to create new surface area A:

$$dW = \gamma dA \ . \tag{2.1}$$

The proportionality constant γ represents the surface energy, and it can also be defined by the force f opposing the lateral displacement x of the interface:

$$f dx = \gamma dA \ . \tag{2.2}$$

It is important to note that the surface energy only equals the surface tension when both the bulk and interface reach equilibrium. Decreasing temperature increases surface tension, and the surface tension at temperature T can be approximated if the surface tension at temperature T_0 is known:

$$\gamma(T) = \gamma(T_0) + \left.\frac{\partial \gamma}{\partial T}\right|_{T=T_0} (T - T_0) \ . \tag{2.3}$$

Thus, the term $\partial\gamma/\partial T$ is a negative quantity, and it is equal to the surface entropy.[87]

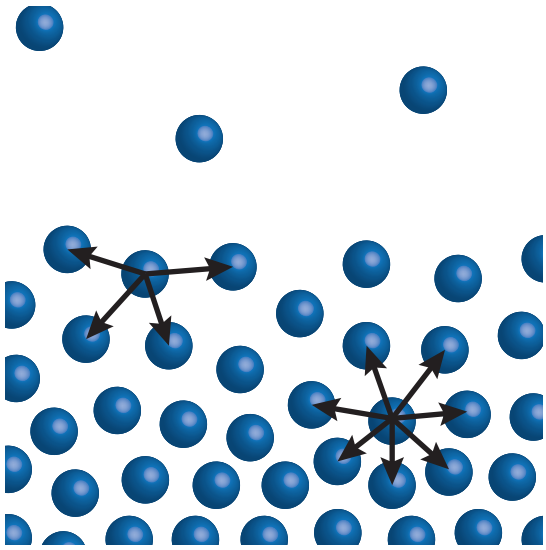

Figure 2.1: Schematic of intermolecular forces at the liquid-vapor interface.

2.1.2 Surfactants and Micelles

Surfactants, a contraction of the phrase "surface-active agents," comprise a class of amphiphilic molecules of biological, environmental, and industrial importance. These

compounds partition to the air/water interface with the hydrocarbon/fluorocarbon tails oriented toward the air phase until the critical micelle concentration (CMC) is reached, or the concentration at which additional surfactants aggregate into micelles in the bulk aqueous phase.[87,88] It is generally understood that surfactants lower surface tension until the CMC is reached, and surface tension remains nearly constant at concentrations greater than the CMC. Intermolecular interactions between ionic surfactant headgroups, the solvation shell, and counterions drive surface tension depression.[89] Additionally, inorganic ions have a "salting-out" effect on surfactants and can either expand or contract ionic surfactant films.[67,88,90,91] Surface tensiometry (Section 2.3.1) and rheometry,[92,93] surface potentiometry,[94,95] and Brewster angle microscopy[96,97] (Section 2.3.2) are robust tools for extracting thermodynamic properties of surfactant films, but these methods lack molecular specificity. Vibrational spectroscopy[98] (Section 2.3.3) and neutron reflectometry[99,100] offer molecular specificity for studying surfactant film composition and structure at the air/water interface.

Micelles are aggregates of $\sim 30 - 100$ surfactant molecules normally around 3-6 nm in diameter.[87] The surfactant alkyl/fluoroalkyl tails are directed inwards such that the hydrophilic headgroups are solvated by the aqueous phase. At surfactant concentrations below the CMC, most of the surfactant molecules are spaced to exist as monomers or low number aggregates. Increasing the surfactant concentration increases the number of monomers, but it also increases the number of aggregates and micelles. Upon reaching the CMC, the number of monomers plateaus, and additional surfactants aggregate into micelles.

Temperature has a small impact on ionic surfactant aggregation, but electrolytes exert a much greater influence.[87] The ionic surfactants simply become insoluble below a particular temperature known as the Krafft point. Due to electrostatic repulsion between the charged headgroups, ionic surfactants generally have higher CMCs in comparison to nonionic surfactants. Addition of salt screens the repulsive forces,

thereby lowering the CMC.

2.1.3 Adsorption Models

Surface tension is often used as a quantitative measure of surfactant adsorption to the air/water interface. As stated in Section 2.1.2, surfactant adsorption lowers aqueous surface tension with increasing concentration. The Gibbs equation can be derived from thermodynamics to relate surface tension to excess interfacial concentrations of surfactant relative to the bulk aqueous phase. Although the Gibbs adsorption equation will not be derived here, a complete derivation can be found in Ref. 101. Experimental surface tension data can be fitted to the Gibbs equation

$$\Gamma = -\frac{C}{RT}\left(\frac{\partial\gamma}{\partial C}\right)_T , \tag{2.4}$$

in which Γ is the surfactant surface excess, C is the surfactant concentration in bulk aqueous solution, R is the gas constant, T is the temperature, and γ is the surface tension of the surfactant solution.

To better quantify differences in ionic surfactant interfacial concentration induced by ions dissolved in aqueous solution, a modified form of the Gibbs adsorption isotherm can be used.[102,103] Surface tension data is fitted to the Szyszkowski equation,[104]

$$\gamma = \gamma_0\left[1 - a \times \ln\left(\frac{C}{b} + 1\right)\right] , \tag{2.5}$$

where γ_0 is the surface tension of the aqueous subphase solution and a and b are fitted parameters. The Szyszkowski equation sufficiently fits a wide range of ionic surfactant concentrations between low and near-CMC values.[103,105,106] The first derivative of the

Szyszkowski equation (Eq. 2.5),

$$\gamma_0 \frac{d\left[1 - a \times \ln\left(\frac{C}{b} + 1\right)\right]}{dC} = -\frac{a\gamma_0}{C + b} \ , \tag{2.6}$$

can be substituted into Eq. 2.4 to produce the Langmuir-Szyszkowski equation:[106–108]

$$\Gamma = \frac{a\gamma_0}{RT}\frac{C}{C + b}. \tag{2.7}$$

In this expression, the $a\gamma_0/RT$ term is equivalent to the maximum surface excess ($\Gamma_{\max}$) in the Langmuir equation:

$$\Gamma = \Gamma_{\max}\frac{C}{K + C} \ . \tag{2.8}$$

In the Langmuir equation, K represents the equilibrium adsorption constant. The b term in Eq. 2.7 analogously represents equilibrium adsorption and describes the free energy of transfer from the bulk solution to the interface.

The Langmuir-Szyszkowski equation employs the assumptions of an infinitely thin, flat interface with monolayer coverage and ideal interactions between the surfactant molecules.[87] However, recent experiments have shown that the surfactant interface is actually quite diffuse, and the electrolyte composition can extend the interfacial depth.[90,91,109,110] Increasing physical relevance is generally accompanied by increasing model complexity, sometimes with only marginal increases in accuracy. A detailed discussion of adsorption models can be found in Refs. 111 and 112.

2.1.4 Gibbs and Langmuir Monolayers

The previous sections (Sections 2.1.2 and 2.1.3) have focused on soluble Gibbs surfactant monolayers in which surface area compression does not change the surface tension

or surface coverage; rather, the equilibrium between bulk and surface is maintained due to surfactant dissolution into the subphase.[87,88] Soluble surfactants are generally dissolved in aqueous solution, and Gibbs monolayers are formed via adsorption to the air/water interface. Insoluble Langmuir monolayers are spread onto the aqueous surface using a syringe, and the amount of amphiphile present is assumed to be equivalent to the amount spread. In order to form a monolayer, however, the intermolecular interactions between the hydrophilic headgroups and the underlying aqueous subphase must be greater than the cohesive forces between the surfactants themselves. Thus, Langmuir monolayers form when the interfacial area is large enough for all the molecules to spread onto the surface.

Due to molecular confinement at the air/water interface, Langmuir monolayers undergo two-dimensional phase transitions. Changing intermolecular area alters the intermolecular interactions between the insoluble surfactants, leading to changes in monolayer organization. These two-dimensional phase states are often described with their analogous three-dimensional state terminology: gas, liquid, and solid.[113] Throughout this dissertation, additional terminology will be used to distinguish between changes in the lipid tilt angle as a function of monolayer compression, which is summarized in Fig. 2.2. The liquid phase can be divided into the liquid expanded and (liquid) tilted condensed phases, and the solid phase is synonymously referred to as the untilted condensed phase.[86,87,114,115]

In a gaseous (G) film, the surfactants are spread far apart from one another such that the mean molecular area (MMA) is very large. Because the area/molecule (A) is large, changes in surface tension are generally less than 0.50 mN/m. Due to the large intermolecular distances, van der Waals interactions between the amphiphiles are negligible. As a result, the gaseous monolayer obeys the two-dimensional ideal gas equation:

$$\pi A = k_B T \ . \tag{2.9}$$

In this equation, surface pressure is defined as

$$\pi = \gamma_0 - \gamma \ . \tag{2.10}$$

The molecules have a kinetic energy of $\frac{1}{2}k_BT$ for each degree of freedom where k_B is the Boltzmann constant, so the kinetic energy is equal to k_BT in the two-dimensional plane. Changes in surface pressure arise from collisions due to translational kinetic energy.[86,87]

Compression of the insoluble monolayer to smaller MMA values increases the lateral interactions between the amphiphiles, causing a first-order transition into the liquid state. In the liquid expanded (LE) phase, the area/molecule is still much larger than the size of the individual molecules. The headgroups are highly hydrated, and the surfactants come into contact with one another. However, there is no long-range lateral organization in the hydrocarbon/fluorocarbon tails. The LE phase can be described by the two-dimensional van der Waals equation of state,

$$\left(\pi + \frac{a}{A^2}\right)(A - b) = k_BT \ , \tag{2.11}$$

where a is the van der Waals constant that that parameterizes the strength of the attractive potential, and b is a constant that represents the excluded or unavailable area per mole of molecules.[88] These constants can be defined mathematically in which

$$a = \frac{\pi C N_0^2}{4\sigma_d^4} \tag{2.12}$$

and

$$b = \frac{1}{2}\pi N_0 \sigma_d^2 \ . \tag{2.13}$$

In Eqs. 2.12 and 2.13, C is the London dispersion force coefficient, N_0 is the number of molecules, and σ_d is the molecular diameter modeled as a hard sphere.

Further monolayer compression causes a first-order phase transition into the tilted condensed (TC) phase, also called the liquid condensed (LC) phase. Amphiphiles in the TC phase exhibit long range order in the hydrophobic tails, and the tails are tilted relative to surface normal. The headgroups are still hydrated, but the film is relatively stiff. Transition into the untilted condensed (UC) phase pushes the amphiphiles into their tightest conformations and maximizes monolayer lateral organization. The hydrophobic tail tilt angles decrease, and the headgroups are largely dehydrated.[87]

Eventually the monolayer cannot be compressed to a smaller MMA due to repulsive exchange interactions. Thus, the monolayer is destabilized and collapses into three-dimensional structures. Monolayer rigidity dictates the collapse surface pressure and collapse mechanism. Rigid or highly ordered monolayers collapse at high surface pressures via fracturing in which the material either forms multilayer aggregates in the air phase or desorbs as aggregates into the aqueous subphase. Fluid monolayers collapse at low surface pressures and lose material by desorption into the subphase. Monolayers with an intermediate rigidity can fold. The monolayer remains intact and buckles to form protrusions into the subphase, and the protrusions are nucleated at random defects across the monolayer. As the monolayer is compressed, the fraction of monolayer in the folds increases relative to the flat regions. Consequently, the surface pressure plateaus once folds are formed. Unlike fracturing and film desorption collapse mechanisms for rigid and fluid monolayers, the folding collapse mechanism is reversible; increasing the MMA simply decreases the fraction of monolayer in the folds and increases the amount in the flat regions.[116–118]

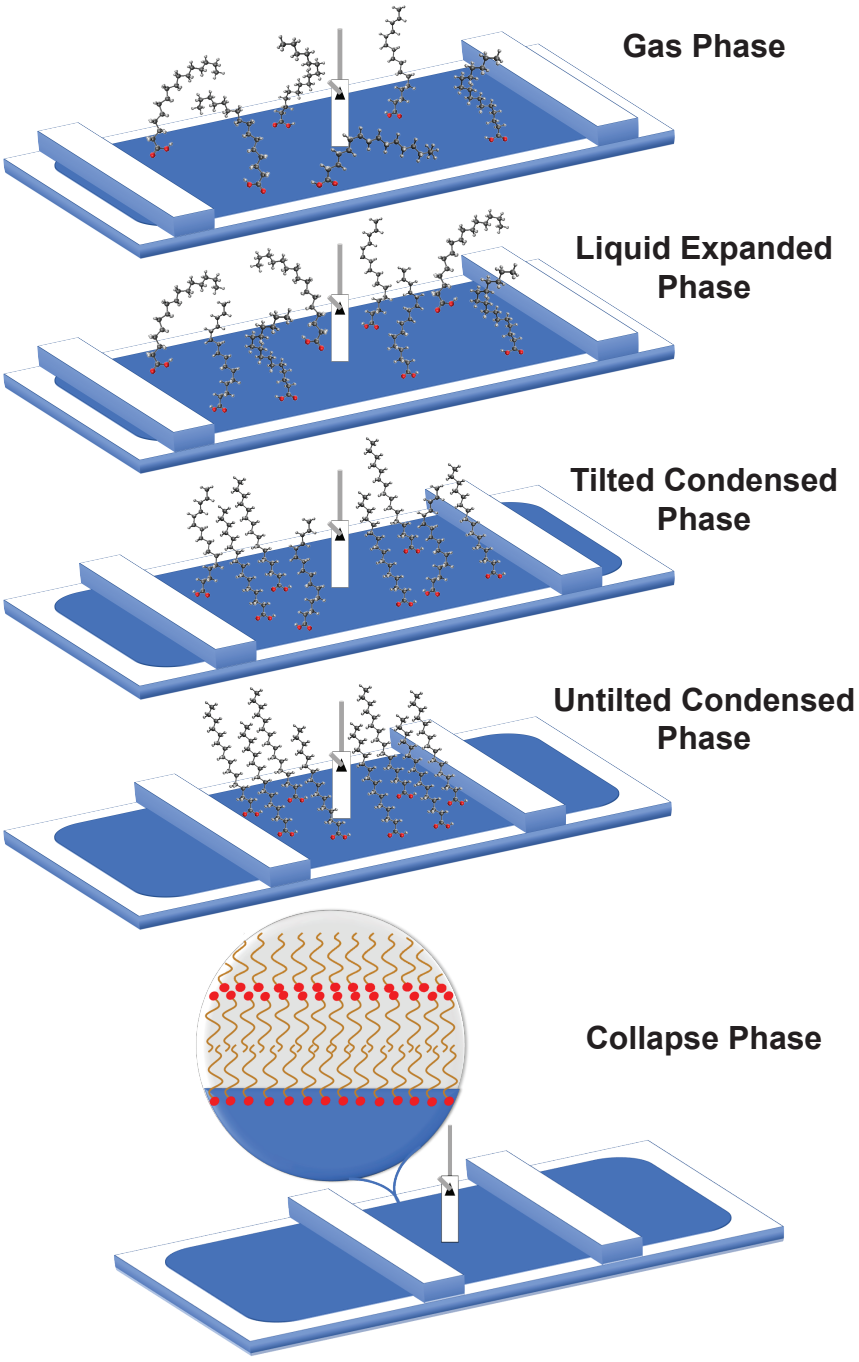

Figure 2.2: Two-dimensional phases of a palmitic acid Langmuir monolayer at the air/water interface.

2.2 Spectroscopic Theoretical Background

This section introduces the fundamental theory behind the spectroscopy and microscopy experiments presented in later chapters. An emphasis is placed on the reflection of light from a dielectric medium to further inform the reflection techniques used in surface-sensitive experiments. Secondly, the theory of infrared spectroscopy and vibrational excitons will be summarized.

2.2.1 Light in a Bulk Medium

The response of a dielectric medium to an electromagnetic field is of significant concern for spectroscopy in the condensed phase. A dielectric medium alters the electric permittivity ϵ and the magnetic permeability μ relative to the values in vacuum, ϵ_0 and μ_0, respectively. Permittivity and permeability are often reported as unitless constants corresponding to the ratio of the values in a dielectric relative to the values in vacuum:

$$\epsilon_r = \frac{\epsilon}{\epsilon_0} \tag{2.14}$$

and

$$\mu_r = \frac{\mu}{\mu_0} \ . \tag{2.15}$$

Relative permittivity, also known as the dielectric constant, describes the factor by which the electric field is decreased between point charges embedded in a dielectric medium relative to vacuum. Thus, a medium with a high permittivity polarizes more in response to an applied electric field. Similar to permittivity, relative permeability describes the extent of magnetic polarization that a dielectric medium experiences in response to an applied magnetic field relative to vacuum.

Refractive index is also a useful quantity for characterizing the speed of light

through a dielectric medium. The phase speed of light in a medium,

$$\nu = \frac{1}{\sqrt{\epsilon\mu}} \ , \tag{2.16}$$

can be rearranged to produce the absolute index of refraction n:

$$n = \frac{c}{\nu} = \pm\sqrt{\frac{\epsilon\mu}{\epsilon_0\mu_0}} = \pm\sqrt{\epsilon_r\mu_r} \ . \tag{2.17}$$

Because water and air are largely transparent in the infrared, $\mu_r \approx 1$, so the refractive index simplifies to

$$n = \sqrt{\epsilon_r} \ . \tag{2.18}$$

This relationship works well for some gases; however, ϵ_r and therefore n are frequency dependent due to dissipative absorption and nonresonant scattering, an effect known as dispersion. Only vacuum is nondispersive, and all materials are dispersive to some extent. For an isotropic medium, dispersion can be described by the classical mechanical oscillator model,

$$n^2(\omega) = 1 + \frac{Nq_e^2}{\epsilon_0 m_e} \sum_j \left(\frac{f_j}{\omega_{0j}^2 - \omega^2 + i\gamma_j\omega} \right) \ , \tag{2.19}$$

in which N is the number of molecules per unit volume, q_e is the charge of an electron, m_e is the mass of an electron, f_j is the strength of oscillating bound electron j, ω is the frequency of the applied harmonic wave, ω_{0j} is the resonant frequency of oscillator j, and γ_j is the damping term of oscillator j. At frequencies below resonance, the oscillator displacements are nearly in-phase with the applied electric field, so the dielectric constant and refractive index are greater than one.[119]

The refractive index can also be expressed as the complex function

$$\tilde{n} = n - i\kappa \tag{2.20}$$

to account for attenuation of light in the dielectric medium.[120] In this equation, κ represents the extinction coefficient for light propagating through the medium. Like n, κ is dependent upon the frequency of light. The extinction coefficent is related to the absorption coefficient α through the following equation:

$$\alpha = \frac{2\omega\kappa}{c} = 2\left(\frac{2\pi}{\lambda}\right)\kappa = \frac{4\pi\kappa}{\lambda} \ . \tag{2.21}$$

In an absorbing dielectric medium, the decrease in irradiance I per unit length z into the medium is expressed as

$$\frac{dI(z)}{dz} = -\alpha I(z) \ . \tag{2.22}$$

Integrating Eq. 2.22 yields the expression

$$I(z) = I_0 e^{-\alpha z} \tag{2.23}$$

in which I_0 is the irradiance of light at $z = 0$. When the quantity αz in Eq. 2.23 is equal to 1.0, the irradiance decreases by a factor of e^{-1} relative to I_0 which is defined as the penetration depth D_p. Thus, the penetration depth of light in a dielectric medium can be modeled through the following equation:

$$D_p = \frac{1}{\alpha} = \frac{\lambda}{4\pi\kappa} \ . \tag{2.24}$$

2.2.2 Light at a Dielectric Interface

A plane wave of light incident upon the interface of a dielectric medium is split into two waves: a reflected wave propagated into the first phase and a transmitted wave propagated through the second phase. Assuming that the reflected and transmitted light are also plane waves, expressions can be derived from Electromagnetic Theory for the direction and amplitude of propagation. Complete derivations have been

presented elsewhere,[119,121] so a summary of the important results will be presented here.

The Law of Reflection states that the angle of incidence θ_i is equal to the angle of reflection θ_r

$$\theta_i = \theta_r \tag{2.25}$$

in which the angles are defined relative to surface normal. The Law of Refraction, also known as Snell's Law, is slightly more complicated:

$$\tilde{n}_1 \sin\theta_i = \tilde{n}_2 \sin\theta_t \ . \tag{2.26}$$

In this expression, θ_t is the angle of transmission relative to surface normal, $\tilde{n}_1$ is the complex refractive index corresponding to the medium of incidence and reflection, and $\tilde{n}_2$ is the complex refractive index corresponding to the medium of transmission. If $\kappa = 0$, then the law simplifies to

$$n_1 \sin\theta_i = n_2 \sin\theta_t \ . \tag{2.27}$$

From Snell's Law and Electromagnetic Theory, equations can be derived to describe the reflection and transmission of light at the interface of two dielectric media as a function of θ_i and the linear polarization of light.[119–121] These equations, known as the Fresnel equations, are solved for two orthogonal linear polarizations, defined as s and p. The p polarization corresponds to the polarization of a wave's electric field parallel with the plane of incidence (perpendicular to the surface plane), and s polarization corresponds to the electric field polarization normal to the plane of incidence (parallel to the surface plane). This is a sufficient description because any polarization state can be resolved into a combination of the two orthogonal linear polarizations. The reflection (r_s and r_p) and transmission (t_s and t_p) coefficients are

expressed as follows:

$$r_s = \frac{\tilde{n}_1 \cos\theta_i - \tilde{n}_2 \cos\theta_t}{\tilde{n}_1 \cos\theta_i + \tilde{n}_2 \cos\theta_t} \ , \tag{2.28}$$

$$t_s = \frac{2\tilde{n}_1 \cos\theta_i}{\tilde{n}_1 \cos\theta_i + \tilde{n}_2 \cos\theta_t} \ , \tag{2.29}$$

$$r_p = \frac{\tilde{n}_2 \cos\theta_i - \tilde{n}_1 \cos\theta_t}{\tilde{n}_1 \cos\theta_t + \tilde{n}_2 \cos\theta_i} \ , \tag{2.30}$$

and

$$t_p = \frac{2\tilde{n}_1 \cos\theta_i}{\tilde{n}_1 \cos\theta_t + \tilde{n}_2 \cos\theta_i} \ . \tag{2.31}$$

The coefficients describe the ratio of the complex amplitude of the propagated wave relative to that of the incoming wave.

The ratio of the reflected and transmitted power to the incident power is defined as the reflectance R and transmittance T, respectively:[119,121]

$$R_s = r_s^2 \ , \tag{2.32}$$

$$T_s = \left(\frac{\tilde{n}_2 \cos\theta_t}{\tilde{n}_1 \cos\theta_i}\right) t_s^2 \ , \tag{2.33}$$

$$R_p = r_p^2 \ , \tag{2.34}$$

and

$$T_p = \left(\frac{\tilde{n}_2 \cos\theta_t}{\tilde{n}_1 \cos\theta_i}\right) t_p^2 \ . \tag{2.35}$$

The transmittance functions are more complicated because power is only proportional to the squared amplitude when the wave impedances of the dielectric media are the same. As a result, it is often simpler to take advantage of energy conservation to solve for transmittance:

$$R_s + T_s = 1 \tag{2.36}$$

and

$$R_p + T_p = 1 \ . \tag{2.37}$$

For unpolarized light, the total reflectance is described by

$$R = \frac{1}{2}(R_s + R_p) = |r|^2 \ . \tag{2.38}$$

Reflectance is the quanity measured in all reflectance instruments.

2.2.3 Infrared Spectroscopy

To determine the general form for vibrational transition intensities and selection rules observed in infrared spectroscopy, it is a useful exercise to consider a simple diatomic molecule. Derivation of the quantum harmonic oscillator model will be presented due to the later use of the harmonic oscillator approximation in *ab initio* vibrational frequency calculations. The following discussion will use the notation presented by Bernath[122] and Willock.[123]

Considering a diatomic molecule A–B, the kinetic energy T can be written as

$$T = \frac{1}{2}m_A v_A^2 + \frac{1}{2}m_B v_B^2 \tag{2.39}$$

in which m_A and m_B represent the atomic masses, and v_A and v_B represent the atomic velocities. The nuclei motion can be separated into center-of-mass and internal components using internal coordinates,

$$\boldsymbol{r} = \boldsymbol{r}_B - \boldsymbol{r}_A \ , \tag{2.40}$$

and the center-of-mass position is defined as

$$\boldsymbol{R} = \frac{m_A \boldsymbol{r}_A + m_B \boldsymbol{r}_B}{m_A + m_B} = \frac{m_A \boldsymbol{r}_A + m_B \boldsymbol{r}_B}{M} \tag{2.41}$$

Solving for $\boldsymbol{r}_A$ and $\boldsymbol{r}_B$ in terms of $\boldsymbol{R}$ and $\boldsymbol{r}$ yields the following expressions:

$$\boldsymbol{r}_A = \boldsymbol{R} - \frac{m_B}{M}\boldsymbol{r} \tag{2.42}$$

and

$$\boldsymbol{r}_B = \boldsymbol{R} + \frac{m_A}{M}\boldsymbol{r} \ . \tag{2.43}$$

Thus, Eqs. 2.42 and 2.43 can be substituted into the kinetic energy expression (Eq. 2.39) to produce

$$T = \frac{1}{2}m_A\left(\frac{\partial \boldsymbol{R}}{\partial t} - \frac{m_B}{M}\frac{\partial \boldsymbol{r}}{\partial t}\right)\cdot\left(\frac{\partial \boldsymbol{R}}{\partial t} - \frac{m_B}{M}\frac{\partial \boldsymbol{r}}{\partial t}\right) + \frac{1}{2}m_B\left(\frac{\partial \boldsymbol{R}}{\partial t} + \frac{m_A}{M}\frac{\partial \boldsymbol{r}}{\partial t}\right)\cdot\left(\frac{\partial \boldsymbol{R}}{\partial t} + \frac{m_A}{M}\frac{\partial \boldsymbol{r}}{\partial t}\right) \tag{2.44}$$

which can be simplified to

$$T = \frac{1}{2}M\left|\frac{\partial \boldsymbol{R}}{\partial t}\right|^2 + \frac{1}{2}\mu\left|\frac{\partial \boldsymbol{r}}{\partial t}\right|^2 \ . \tag{2.45}$$

In Eq. 2.45, μ is the reduced mass:

$$\mu = \frac{m_A m_B}{m_A + m_B} \ . \tag{2.46}$$

Upon transforming the kinetic energy expression in Eq. 2.45 into terms of momentum p rather than velocity, the two-particle Hamiltonian H can be written as

$$H = \frac{p_R^2}{2M} + \frac{p_r^2}{2\mu} + V(r) \tag{2.47}$$

in which $V(r)$ is the potential energy as a function of interatomic distance r. The center of mass component of the potential energy ($p_R^2/2M$) can be ignored because it only shifts the total energy. Consequently, the quantum mechanical expression for a vibrating rotor is

$$\frac{-\hbar^2}{2\mu}\nabla^2\psi + V(r)\psi = E\psi \ . \tag{2.48}$$

From Eq. 2.48, the Cartesian coordinates can be replaced with polar spherical coordinates, and the angular momentum operator $\hat{J}$ can be substituted to produce the expression

$$\frac{-\hbar^2}{2\mu}\left(\frac{1}{r^2}\frac{\partial}{\partial r}r^2\frac{\partial\psi}{\partial r}\right) + \frac{1}{2\mu r^2}\hat{J}^2\psi + V(r)\psi = E\psi \ . \tag{2.49}$$

The wavefunction can be represented with the spherical harmonic function Y_{JM} such that

$$\psi = R(r)Y_{JM}(\theta,\phi) \ . \tag{2.50}$$

As a result, Eq. 2.50 can be substituted into Eq. 2.49 to solve for the one-dimensional radial Schrödinger equation:

$$\frac{-\hbar^2}{2\mu r^2}\frac{d}{dr}r^2\frac{dR}{dr} + \left(\frac{\hbar^2 J(J+1)}{2\mu r^2} + V(r)\right)R = ER \ . \tag{2.51}$$

Substituting $S(r) = rR(r)$ into Eq. 2.51 produces the simplified expression

$$\frac{-\hbar^2}{2\mu r^2}\frac{d^2S}{dr^2} + \left(\frac{\hbar^2 J(J+1)}{2\mu r^2} + V(r)\right)S = ES \ . \tag{2.52}$$

From here, a specific form of the potential energy function can be selected to determine solutions to the wavefunction S.

An Taylor series expansion about the equilibrium distance r_e,

$$V(r) = V(r_e) + \left.\frac{dV}{dr}\right|_{r_e}(r-r_e) + \frac{1}{2}\left.\frac{d^2V}{dr^2}\right|_{r_e}(r-r_e)^2 + \cdots \ , \tag{2.53}$$

is used, and $V(r_e)$ is arbitrarily set to zero. Hence, the first derivative is also zero:

$$\left.\frac{dV}{dr}\right|_{r_e} = 0 \ . \tag{2.54}$$

The harmonic oscillator approximation is invoked, so only the first nonzero term in the potential energy expansion (the second derivative) is included. Thus, the general harmonic oscillator solutions for the nonrotating diatomic molecule are

$$S = N_v H_v(x\sqrt{\alpha})e^{-\alpha x^2/2} \tag{2.55}$$

in which $x = r - r_e$ and $\alpha = \mu\omega/\hbar$. Eq. 2.55 is expressed as a product of the Gaussian function $e^{-\alpha x^2/2}$ and the Hermite polynomials $H_v(\sqrt{\alpha}x)$. The corresponding normalization factor N_v for the v^{th} vibrational level is written as

$$N_v = \left(\frac{1}{2^v v!}\left(\frac{\alpha}{\pi}\right)^{1/2}\right)^{1/2} \tag{2.56}$$

in which the angular frequency ω is expressed as

$$\omega = \left(\frac{k}{\mu}\right)^{1/2} \ . \tag{2.57}$$

The ground state $v = 0$ is written as

$$S_0 = \left(\frac{\alpha}{\pi}\right)^{1/4} (x\sqrt{\alpha})e^{-\alpha x^2/2} \tag{2.58}$$

because $H_0 = 1$, and higher order Hermite polynomials model the vibrationally excited states $v = 1, 2, 3, \cdots n$. The eigenvalues for the nonrotating harmonic oscillator are

$$E_v = h\nu\left(v + \frac{1}{2}\right) = \hbar\omega\left(v + \frac{1}{2}\right) \ . \tag{2.59}$$

Frequency ν is

$$\nu = \frac{1}{2\pi}\left(\frac{k}{\mu}\right)^{1/2} , \tag{2.60}$$

and k corresponds to the spring constant. Thus, the harmonic oscillator has an equal spacing of $\hbar\omega$ between the quantized energy levels.

The diatomic model is also useful for deriving the infrared vibrational selection rules. The transition dipole moment integral $\boldsymbol{M}_{v'v''}$ determines the intensity of a vibrational transition:

$$\boldsymbol{M}_{v'v''} = \int \psi'^{*}_{\text{vib}} \boldsymbol{\mu}(r) \psi''_{\text{vib}} dr \ . \tag{2.61}$$

The double and single primes represent the lower and upper levels of a vibrational transition, respectively. A Taylor series expansion about $r = r_e$ can also be applied to the dipole moment $\mu(r)$:

$$\boldsymbol{\mu} = \boldsymbol{\mu}_e + \left.\frac{d\boldsymbol{\mu}}{dr}\right|_{r_e} (r - r_e) + \frac{1}{2}\left.\frac{d^2\boldsymbol{\mu}}{dr^2}\right|_{r_e} (r - r_e)^2 + \cdots \ . \tag{2.62}$$

Plugging Eq. 2.62 into Eq. 2.61 produces

$$\boldsymbol{M}_{v'v''} = \boldsymbol{\mu}_e \int \psi'^{*}_{\text{vib}} \psi''_{\text{vib}} dr + \left.\frac{d\boldsymbol{\mu}}{dr}\right|_{r_e} \int \psi'^{*}_{\text{vib}} (r - r_e) \psi''_{\text{vib}} dr + \cdots \tag{2.63}$$

in which the first term is zero because ψ'_{vib} and ψ''_{vib} are orthogonal. As a result, the second term dominates the infrared spectrum, and the intensity I of a vibrational absorption or emission is

$$I \propto |\boldsymbol{M}_{v'v''}|^2 \propto \left|\frac{d\boldsymbol{\mu}}{dr}\right|^2_{r_e} \tag{2.64}$$

given the harmonic oscillator approximation. Therefore, the harmonic oscillator wavefunctions (Eq. 2.58) can be substituted into the wavefunctions in the integral

$\int \psi'^{*}_{\text{vib}}(r - r_e)\psi''_{\text{vib}}dr$. Finally, using the recursion relationship

$$2xH_n(x) = H_{n+1}(x) + 2nH_{n-1}(x) \ , \tag{2.65}$$

the integral can be solved to generate

$$\langle v'|r - r_e|v\rangle = \left(\frac{\hbar}{2m\omega}\right)^{1/2} (\sqrt{v+1}\delta_{v',\ v+1} + \sqrt{v}\delta_{v',\ v-1}) \ . \tag{2.66}$$

Because the Kronecker delta function in Eq. 2.66 dictates that $v' = v+1$ or $v-1$, this result provides the vibrational selection rule of $\Delta v = \pm 1$ for the quantum harmonic oscillator.

2.2.4 Vibrational Exciton Theory

Fundamentally, an exciton is the delocalization of an excited state. Frenkel proposed the idea that an exciton is the superposition of excited states on local sites.[124] Hexter extended this approach to vibrationally excited states coupled through their resonant transition dipole moments, known as vibrational excitons.[125] Resonant transition dipole moment coupling between near-degenerate vibrational modes causes energy level splitting, leading to vibrational state wavefunction mixing. The total vibrational energy of an excitonic state is a sum of the energies corresponding to the uncoupled vibrational modes and the pairwise coupled modes on each molecule:

$$\langle \Psi|\hat{H}|\Psi\rangle = \sum_{Ri} \omega_R^i + \sum_{R>S} \sum_{\substack{i\in R \\ j\in S}} \gamma_{RS}^{ij} \ . \tag{2.67}$$

In this equation, ω_R^i represents the frequency of the noninteracting vibrational mode i on molecule R, and γ_{RS}^{ij} represents the interaction frequency of modes i and j where i is a mode on molecule R and j is a mode on molecule S. The excitonic Hamiltonian

$\hat{H}$ is calculated in the product basis

$$\Psi_I = \sum_R \sum_i k_R^i \psi_R^i \prod_{R \neq S} \psi_S \tag{2.68}$$

in which Ψ_I is the wavefunction of excited state I of the full molecular system, k_R^i is a coefficient obtained during diagonalization that transforms the local mode basis to the exciton basis, ψ_R^i is the wavefunction of the first excited state i of molecule R, and ψ_S is the wavefunction of the ground-state of molecule S.

The excitonic Hamiltonian typically describes the coupling of vibrational modes via classical transition dipole moment interactions. The total vibrational Hamiltonian takes the form of

$$\hat{H} = \hat{H}_0 + \hat{V} \tag{2.69}$$

in which $\hat{H}_0$ and $\hat{V}$ correspond to the uncoupled and coupled Hamiltonians, respectively. More specifically, $\hat{H}_0$ is expressed as the sum over all the noninteracting vibrationally excited states i on molecule R, and $\hat{V}$ is the sum over all the pairwise coupled vibrationally excited states i and j on molecules R and S:[126]

$$\hat{H} = \sum_{Ri} \hat{H}_R^i + \frac{1}{2} \sum_{R>S} \sum_{\substack{i \in R \\ j \in S}} \hat{V}_{RS}^{ij} \ . \tag{2.70}$$

Because $E_{RS} = E_{SR}$, the coefficient of 1/2 is necessary before the sum of the coupled Hamiltonian. The expression for the full coupled Hamiltonian is written as

$$\boldsymbol{V}_{RS}^{ij} = \sum_{R>S} \sum_{\substack{i \in R \\ j \in S}} -\frac{1}{4\pi\epsilon_0} \boldsymbol{\mu}_R^i \cdot \frac{3(\boldsymbol{\mu}_S^j \cdot \boldsymbol{r}_{RS}) \cdot \boldsymbol{r}_{RS} - (\boldsymbol{r}_{RS} \cdot \boldsymbol{r}_{RS}) \cdot \boldsymbol{\mu}_S^j}{r_{RS}^5} \tag{2.71}$$

in which $\boldsymbol{r}_{RS}$ is the vector connecting the centers-of-mass of molecules R and S, and r_{RS} is the distance.[127–129] The harmonic oscillator approximation is invoked for the transition dipole moments $\boldsymbol{\mu}_R^i$ and $\boldsymbol{\mu}_S^j$.

2.3 Instrumental Methods

Details about the instrumentation and experimental configurations can be found in the Methods sections of the following chapters. Here, a brief description of each method and its underlying theory is presented.

2.3.1 Surface Tensiometry

Surface tensiometry is a useful tool for quantifying interfacial surface excess and thermodynamic properties of Gibbs and Langmuir monolayers. The Wilhelmy plate technique is used to measure surface tension throughout this dissertation, so it will be discussed briefly. A Wilhelmy plate can be made of any material provided that it is fully wetted by the aqueous subphase, and the plate is generally a few square centimeters in area.[87,113] Platinum is often used because of its durability, ease of cleaning, and low reactivity; residual organic contaminants are removed by firing the platinum plate in a Bunsen burner until red hot. Plates made out of filter paper can also be used, and these plates are disposed after use. The Wilhelmy plate is hung from a hook attached to a tensiometer, and the plate is placed to make contact with the aqueous surface (Fig. 2.3).

Net forces F_{net} acting on the Wilhelmy plate are the sum of the gravitational force F_g, the buoyancy force F_b, and the surface tension γ:

$$F_{\text{net}} = F_g + F_b + \gamma \ . \tag{2.72}$$

Using known experimental parameters, Eq. 2.72 is then expressed as

$$F_{\text{net}} = \rho_p lwt + 2\gamma(t + l)\cos\theta - \rho_0 gtwh \tag{2.73}$$

in which ρ_p is the density of the Wilhelmy plate, l is the length of the plate, w is

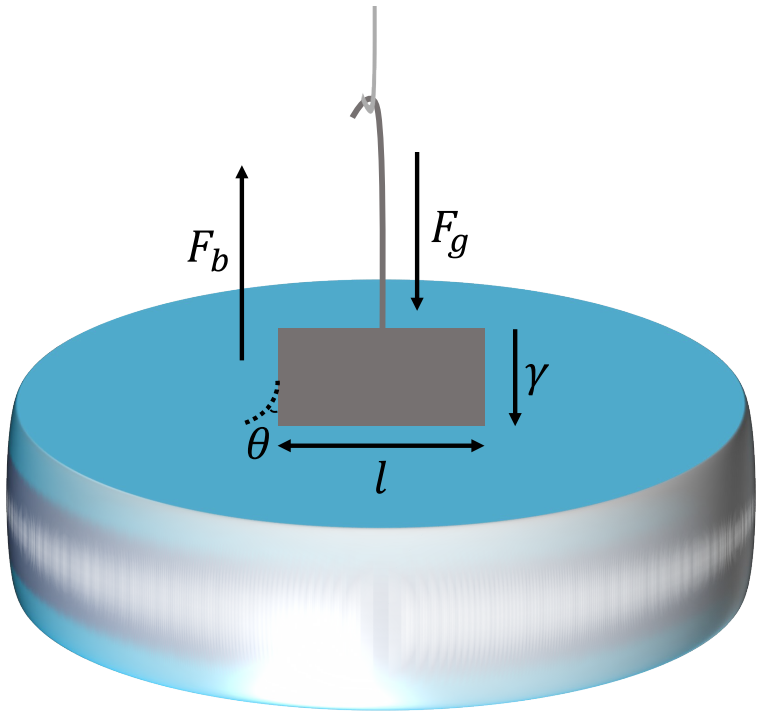

Figure 2.3: Diagram of the Wilhelmy plate method for measuring surface tension at the air/water interface. F_b represents the buoyancy force, F_g is the gravitational force, γ is the surface tension, l is the length of the plate, and θ is the contact angle between the aqueous subphase and the plate.

the width of the plate, t is the thickness of the plate, θ is the contact angle between the subphase and the plate, ρ_0 is the subphase density, and h is the immersion depth of the Wilhelmy plate into the subphase.[113] Eq 2.73 can be simplified with several assumptions. Because the Wilhelmy plate is so thin, t can be neglected ($t \to 0$). Secondly, complete wetting can be assumed such that $\theta = 0$, so $\cos\theta = 1$. As a result, Eq. 2.73 simplifies to

$$F_{\text{net}} \approx 2\gamma l \ . \tag{2.74}$$

As stated in Section 2.1.4, Gibbs monolayers are prepared by allowing dissolved surfactants to adsorb to the air/water interface. Thus, the surface tension is simply measured on a poured surfactant solution in a glass dish. For insoluble Langmuir monolayers, the aqueous subphase is poured into a Langmuir trough coated in a hydrophobic substance, such as polytetrafluoroethylene (PTFE). Two hydrophilic

barriers are placed on top of the trough, and a computer controls the compression rate across the surface. To prepare an insoluble monolayer, the surfactant is first dissolved in a volatile organic solvent and deposited dropwise onto the surface using a syringe. The solvent is allowed to evaporate, and then the barriers are compressed at a set rate to reduce the available interfacial area. Meanwhile, the Wilhelmy plate attached to the tensiometer measures surface tension as a function of barrier compression (Fig. 2.2). The data for Langmuir monolayers are often presented as surface pressure-area isotherms in which surface pressure (Eq. 2.10) is plotted against MMA.[87]

2.3.2 Brewster Angle Microscopy

Brewster angle microscopy (BAM) is a background-free imaging technique for studying thin films on flat surfaces. It has been used extensively as a noninvasive method for directly visualizing organic films at the air/water interface.[130,131] Film morphological properties such as molecular density, film thickness, molecular tilt angle, lipid domain optical anisotropy, and monolayer phase transitions have been characterized using this technique.[96,132–148] The optical design is relatively simple (Fig. 2.4), and the instrument can be constructed at low cost.[149,150]

BAM takes advantage of the minimized reflectance of p-polarized light at the Brewster angle of the interface between the two isotropic media to isolate the film signal from the background.[151] Incident light of intensity I_0 is partially reflected (I_R) and partially transmitted at the interface according to the Fresnel equations, and the reflectance is equal to

$$R = \frac{I_R}{I_0} \tag{2.75}$$

As described in Section 2.2.2, the reflected light is polarization-dependent:

$$R_p = \left(\frac{\tan(\theta_i - \theta_t)}{\tan(\theta_i + \theta_t)} \right)^2 \tag{2.76}$$

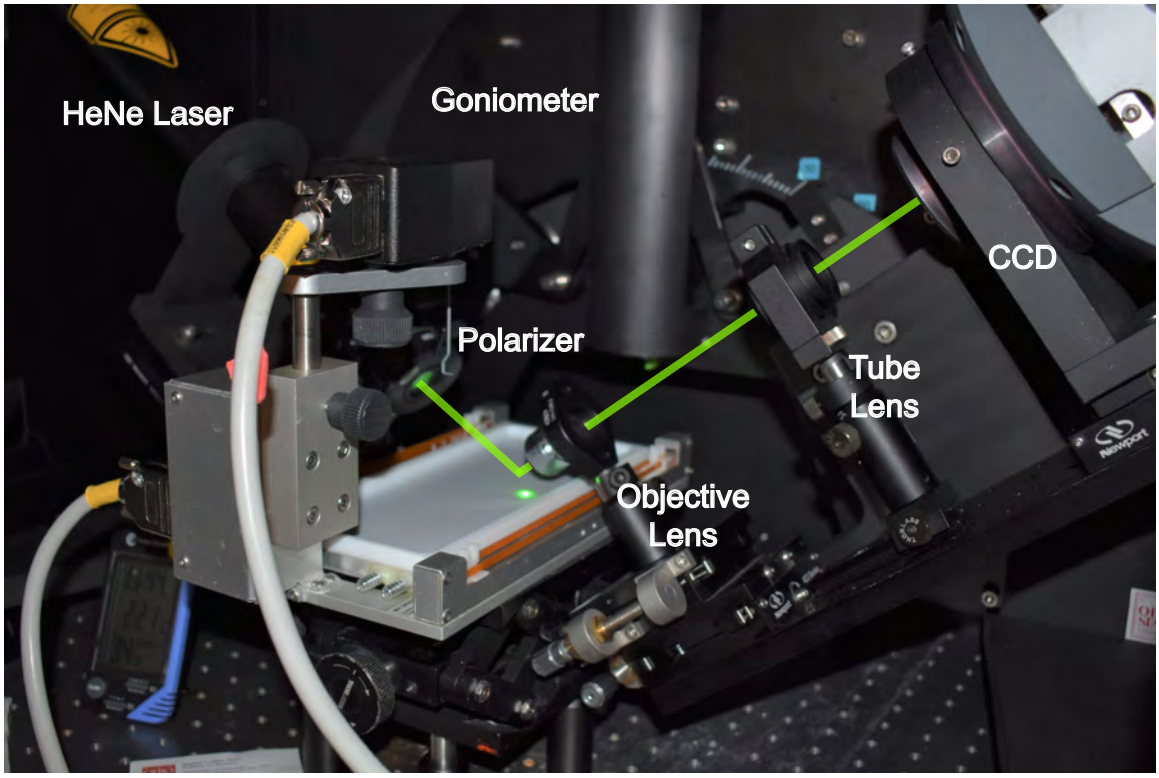

Figure 2.4: Optical setup of the Brewster angle microscope in the Allen lab.

and

$$R_s = \left(\frac{\sin(\theta_i - \theta_t)}{\sin(\theta_i + \theta_t)} \right)^2 . \tag{2.77}$$

R_p approaches zero when the denominator of Eq. 2.77 becomes infinite, or when $\theta_i + \theta_t = \pi/2$. The angle of incidence at which $R_p = 0$ is known as the Brewster angle θ_B ($\theta_i = \theta_B$), and θ_B can be solved from Snell's law (Eq. 2.27). Because $\theta_t = \pi/2 - \theta_B$, Snell's law can be rearranged to produce the expression for the Brewster angle:

$$\theta_B = \tan^{-1} \left(\frac{n_2}{n_1} \right) . \tag{2.78}$$

Thus, using $n_2 = 1.333$ for pure water at 550 nm[152] (close to our BAM laser wavelength of 543 nm) and $n_1 = 1$ for air, $\theta_B = 53.12°$ for the air/water interface.

In performing a BAM experiment, the goniometer (Fig. 2.4) is adjusted such that the laser is positioned at θ_B for the air/water interface. The laser is already mostly

p-polarized (500:1), and the plane-polarized light is further filtered by a polarizer before the light reaches the surface. A thin film has a different index of refraction, so p-polarized light will be reflected from the regions of the interface covered by the thin film. Consequently, only light is reflected from the thin film and focused onto the CCD camera. For real interfaces, R_p decreases to a minimum value as opposed to becoming exactly zero. The index of refraction does not abruptly change from n_1 to n_2 at real interfaces; rather it changes gradually over a finite depth into the surface. Additionally, surface roughness and optical anisotropy caused by preferential molecular orientation at the interface prevent R_p from vanishing.[151,153]

2.3.3 Infrared Reflection-Absorption Spectroscopy

Infrared reflection-absorption spectroscopy (IRRAS) is a surface-sensitive technique for measuring resonant vibrational modes at the air/water interface. It has been used extensively to study monolayer film structure and properties.[154–156] Many studies have focused on monolayer conformational analysis and phase transitions via the frequencies and peak intensities of the C–H alkyl tail vibrational modes.[63,157–173] Improvements in the instrument signal-to-noise in regions with significant water vapor bands allowed for studies of amphiphilic protonation and cationic interactions with the monolayer headgroups.[40,65,67–69,174–180] Additionally, IRRAS has been used to study a variety of complex interfacial phenomena such as binding and protein adsorption to proxy biological membranes.[181–196]

IRRAS is a particularly useful tool for measuring thin films adsorbed at the air/water interface due to the significant signal-to-noise enhancement relative to bulk absorption measurements. The spectroscopic technique provides rich structural information about the interfacial film and its surrounding molecular environment. Additionally, the entire mid-IR range (500-4000 cm^{-1}) can be collected in one spectral acquisition, and the instrument setup involves simple modification of a commercial

FTIR with two gold mirrors for adjusting the angle of incidence (Fig. 2.5). The spectra are plotted as reflectance-absorbance (RA)

$$\mathrm{RA} = -\log\left(\frac{R}{R_0}\right) \tag{2.79}$$

in which R corresponds to the reflectance from the interfacial film, and R_0 corresponds to the reflectance from the aqueous subphase.[154,155,188] Reflectance-absorbance is negative when the film reflectance is greater than the subphase reflectance ($R/R_0 > 1$) and positive when the film reflectance is less than the subphase reflectance ($R/R_0 < 1$).

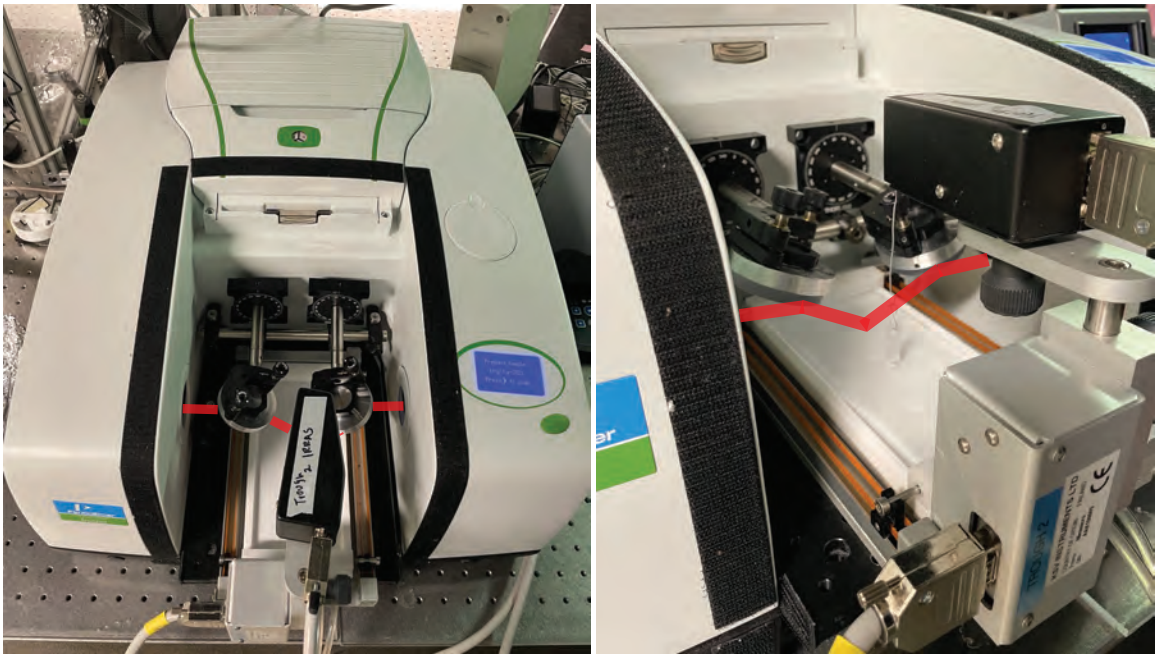

Figure 2.5: Optical setup of the infrared reflection-absorption spectrometer in the Allen lab. The two images depict a commercial FTIR spectrometer modified with two gold mirrors mounted inside the instrument to direct the incident infrared beam toward the liquid surface and to direct the reflected beam to the MCT detector. The setup can accommodate a Langmuir trough and attached surface tensiometer to control monolayer surface pressure and phase state.

The reflectance of the aqueous subphase can be calculated using Eq. 2.38. However, the addition of a film complicates the Fresnel equations due to the presence of a second interface. In this configuration, some light is reflected from the air/film inter-

face, and some light is transmitted to the film/water interface. Light can then propagate into the water subphase, and some light will be reflected from the film/water interface to the air/film interface. At the air/film interface, light can be reflected back to the film/water interface, or the light can propagate into the air phase, and so on. Each successive pass through the film phase and propagation into the air phase decreases in amplitude. Thus, the resultant reflected wave is represented as an infinite series of partial waves.[120]

To appropriately model the contributions of an absorbing, anisotropic film at the air/water interface, the complex refractive indices must be used to account for absorption in each medium. For example, an insoluble fatty acid film has significant CH_2 stretching transition dipole moments parallel to the surface. As a result, the extinction coefficient κ in $\tilde{n}_2$ (Eq. 2.20) has significant x and y components in the frequency region corresponding to the CH_2 stretching modes. While changes in the film optical properties could in theory be modeled through the complex refractive index as a function of interfacial depth ($\tilde{n}_z$), there is a lack of experimental data to effectively parameterize this inhomogeneity.[155]

The first reflection and transmission coefficients from the air/film interface are equal to r_{12} and t_{12} where the subscripts one and two correspond to the air and film phases, respectively. The reflected light from the film/water interface will then have an amplitude of $t_{12}r_{23}$ in which the subscript three corresponds to the water subphase. Upon reaching the air/film interface once again, some of this light will be transmitted into the air phase, yielding a partial wave amplitude of $t_{12}r_{23}t_{21}$. However, this partial wave will be out of phase from the first reflected wave propagating through the air phase; consequently, the phase factor $e^{-in_p\beta}$ must be added to the amplitude coefficient. The phase angle β, expressed as

$$\beta = 2\pi\left(\frac{d}{\lambda}\right)\tilde{n}_2\cos\theta_2 \ , \tag{2.80}$$

accounts for the wave phase change after a single passage through the film, and d corresponds to the film thickness. The numerical coefficient n_p represents the number of times that the wave passes through the film. Hence, the complex amplitude expression $t_{12}r_{23}t_{21}e^{-i2\beta}$ would describe the second partial wave.[120]

This iterative process of describing the partial waves generates an infinite geometric series of complex reflectivity coefficients. Rearranging the terms produces the sum corresponding to the total reflectance,

$$R = r_{12}+t_{12}t_{21}r_{23}e^{-i2\beta}[1+(r_{21}r_{23}e^{-i2\beta})^1+(r_{21}r_{23}e^{-i2\beta})^2+(r_{21}r_{23}e^{-i2\beta})^3+\cdots] \,, \quad (2.81)$$

which can be simplified to

$$R = r_{12} + \frac{t_{12}t_{21}r_{23}e^{-i2\beta}}{1 - r_{21}r_{23}e^{-i2\beta}} \quad (2.82)$$

via the geometric series expansion

$$\frac{1}{1-x} = 1 + x + x^2 + x^3 + \cdots \qquad (x^2 < 1) \,. \quad (2.83)$$

Using the relationships

$$r_{ba} = -r_{ab} \quad (2.84)$$

and

$$t_{ba} = \frac{1 - r_{ab}^2}{t_{ab}} \quad (2.85)$$

corresponding to any medium a and any medium b, Eq. 2.82 can be further simplified to

$$R = \frac{r_{12} + r_{23}e^{-i2\beta}}{1 + r_{12}r_{23}e^{-i2\beta}} \,. \quad (2.86)$$

The total transmittance can also be derived using this strategy:

$$T = \frac{t_{12}t_{23}e^{-i\beta}}{1 + r_{12}r_{23}e^{-i2\beta}} \ . \tag{2.87}$$

Conveniently, similar expressions to Eqs. 2.86 and 2.87 can obtain linearly polarized values for the reflectance and transmittance of a film at the air/water interface:[120]

$$R_p = \frac{r_{12,p} + r_{23,p}e^{-i2\beta}}{1 + r_{12,p}r_{23,p}e^{-i2\beta}} \ , \tag{2.88}$$

$$R_s = \frac{r_{12,s} + r_{23,s}e^{-i2\beta}}{1 + r_{12,s}r_{23,s}e^{-i2\beta}} \ , \tag{2.89}$$

$$T_p = \frac{t_{12,p}t_{23,p}e^{-i\beta}}{1 + r_{12,p}r_{23,p}e^{-i2\beta}} \ , \tag{2.90}$$

and

$$T_s = \frac{t_{12,s}t_{23,s}e^{-i\beta}}{1 + r_{12,s}r_{23,s}e^{-i2\beta}} \ . \tag{2.91}$$

From the modified Fresnel equations described above (Eqs. 2.88-2.91), one can predict that IRRAS reflectance-absorbance is dependent upon the angle of incidence, incoming polarization of IR light, complex indices of refraction as a function of wavelength for each phase, and vibrational transition moment orientation relative to the plane of incidence.[155,188] These parameters affect both the detected intensities and the sign of the peaks. For s-polarized incident light, the vibrational modes corresponding to the film remain negative at all angles of incidence. For p-polarized light, the peaks are negative at angles of incidence below the Brewster angle and positive at angles above the Brewster angle.[167,197] It is important to note that both positive and negative peaks can be observed at a constant angle of incidence, however.[68,172,197,198]

2.3.4 Second Harmonic Generation Spectroscopy

Second harmonic generation (SHG) spectroscopy is a nonlinear surface-specific technique in which two photons with the same frequency interact to produce a photon with twice the energy (half the wavelength) of the two initial photons. The degree of polarization of a dielectric medium in response to an applied electric field can be described by the Taylor series expansion

$$P = P_0 + \epsilon_0 \chi^{(1)} E + \epsilon_0 \chi^{(2)} E^2 + \epsilon_0 \chi^{(3)} E^3 + \cdots \tag{2.92}$$

in which P is the polarization density, E is the electric field, and χ is the electric susceptibility.[119] For linear spectroscopy at low applied electric fields, only the first order term is relevant. However, for high electric fields, such as those used in nonlinear spectroscopy, the polarizability begins to saturate and the higher order terms become relevant. Thus, the second harmonic field $E(2\omega)$ is proportional to the second-order polarization $P^{(2)}(2\omega)$ from the oriented molecules at the interface:[199,200]

$$E(2\omega) \propto P^{(2)}(2\omega) = \chi^{(2)} E(\omega) E(\omega) \ . \tag{2.93}$$

The inherent surface specificity arises from the second-order nonlinear susceptibility tensor $\chi^{(2)}$ which is zero in centrosymmetric media. Intensity I is proportional to E^2, so the SHG electric field can be determined from experimental measurements through the relationship

$$E(2\omega) \propto \sqrt{I(2\omega)} \ . \tag{2.94}$$

The SHG spectrometer used in this dissertation probes a nonresonant response from the anisotropic dipolar alignment at the air/water interface. Although a detailed description of the optical setup can be found in Section 4.2, the instrument (Fig. 2.6) will be described here briefly. After generation of the ∼50 fs pulses centered at

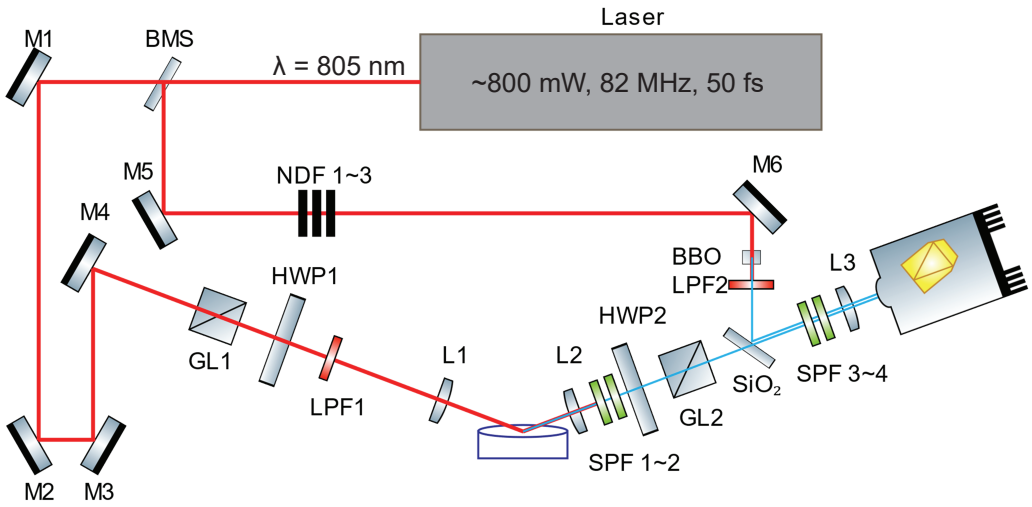

Figure 2.6: Schematic of the optical setup of the second harmonic generation (SHG) spectrometer in the Allen lab. BMS is the beam splitter, M is a mirror, NDF is a neutral density filter, BBO is a beta barium borate crystal, GL is a Glan-laser polarizer, HWP is a half-wave plate, LPF is a long-pass filter, SPF is a short-pass filter, and L is a lens. The optical components of this schematic were obtained from the ComponentLibrary created by Alexander Franzen and licensed under a Creative Commons Attribution-NonCommercial 3.0 Unported License.

805 nm, the pulses are split into a reference channel and a sample channel. The SHG reference is generated by a beta barium borate (BBO) nonlinear optical crystal, and the SHG signal is filtered and redirected toward the detector. In the sample channel, the beam is moved out of the plane of the laser table and into the reflection plane of incidence such that the beam is directed downward toward the liquid surface. Glan-laser polarizers and half-wave plates before and after the sample stage allow for careful selection of linear polarization prior to interacting with the liquid surface and following reflection. A series of filters and lenses align the signal beam parallel with the reference beam going into detector. Lastly, the signal and reference beams are focused through a monochromator slit and onto a CCD.

Chapter 3

Collapse Mechanisms of Nascent and Aged Sea Spray Aerosol Proxy Films

3.1 Introduction

Sea spray aerosol (SSA), generated from breaking waves at the ocean surface, constitutes one of the largest sources of aerosol emissions on the planet.[2] The greatest degree of uncertainty in climate models is the representation of aerosols, of which the magnitude of radiative forcing by natural aerosol emissions is poorly constrained.[82] Aerosols directly affect climate by absorbing and scattering solar radiation, and aerosols indirectly influence the global radiative budget by acting as cloud condensation nuclei (CCN) and ice nuclei (IN) in the atmosphere.[201] The ability of SSA to nucleate ice,[17–22,202–204] seed clouds,[7,9,11,13–15,205,206] and participate in atmospheric chemical reactions[24–27] is dependent upon the size, chemical composition, and phase state of SSA particles.[207–211] Additionally, given that a large fraction of aerosols have high surface-area-to-volume ratios, molecular organization at the air/water interface of SSA is especially relevant in inducing these atmospheric reactions and nucleation processes.[62,212–218] Hence, developing and characterizing the interfacial composition, organization, and reactivity of SSA proxy systems is crucial for improved predictions

of aerosol impacts on climate.[37,83,85]

The chemical diversity of nascent SSA is caused in part by the production mechanism and the biological productivity of the source seawater.[2,45,47,219,220] Organic matter that is transferred to SSA is derived from marine biota, primarily from phytoplankton blooms.[29,30,44,46,221–225] Surface active material such as lipids, proteins, and polysaccharides[5,53,62,78,226,227] partition to the air/sea interface where they can be encapsulated into bubbles and burst to form SSA particles between 10 nm and 5 μm in diameter.[2,46,228] Supermicron SSA composition more closely resembles that of upper surface seawater, so larger SSA particles contain more oxygenated compounds and have a higher fraction of soluble organic material, including short- to medium-chain fatty acids. Submicron SSA composition tends to be enriched in aliphatic compounds, such as long-chain fatty acids.[5,46,53,78,229,230] In both supermicron and submicron SSA, fatty acids of moderate aliphaticity are throught to form films on SSA surfaces.[48,49,53,62] The 2D organization of these films modulate gas and water uptake into the aqueous bulk of the particle.[25,26,30,218,231,232] As a result, experiments involving ocean-relevant SSA film proxies are important for better predictions of aerosol reactivity and nucleation capability in climate models.

During phytoplankton blooms, organic enrichment within SSA is increased such that the competition for space at the SSA surface is high due to the surface activity of the marine-derived organic compounds. Fatty acids, which represent some of the most surface active components in SSA, condense to accommodate for the high surface density of organic molecules at the interface. The ability of the film (i.e., monolayer) to condense and resist transformation from the 2D film into 3D structures is dependent upon the film rigidity which is modulated by lateral interactions between the fatty acid alkyl chains and by interactions between the underlying aqueous core and carboxylic acid head groups.[113,233–236] Shorter chain fatty acids in nascent SSA are expected to be more soluble.[237,238] given that the particles have an initial seawater

pH of ∼8.2. As a result, the longer fatty acids will dominate the lateral interactions in the SSA film, making the film more rigid due to the greater sum of dispersion interactions.[113,239,240] Carboxylic acid head groups of long chain fatty acids (>C_{14}) are only partially deprotonated at high pH due to their relatively high surface pK_a values.[241,242] However, cation-head group interactions slightly moderate the pK_a increase associated with increasing alkyl chain length.[242] As SSA ages in the marine boundary layer (MBL), the particles interact with trace gases that lower the pH of the particle aqueous core. Consequently, shorter fatty acids are less soluble and more surface active, so the SSA film is fluidized.[243–246] SSA film behavior can be represented by 2D Langmuir isotherms in which a fatty acid monolayer is compressed beginning at low surface coverage, and the monolayer surface pressure is measured with decreasing surface area.[231] Film rigidity dictates the maximum monolayer surface pressure (Π_c) attainable before collapse into 3D structures,[117,118,247–249] thereby changing the phase state of the film.

SSA proxy film collapse mechanisms are examined on aqueous NaCl subphases to elucidate changes in film morphology with particle aging in the MBL. A fatty acid mixture composed of myristic acid (C_{14}, MA), palmitic acid (C_{16}, PA), and stearic acid (C_{18}, SA) at the molar ratio of 3 SA:4 PA:2 MA is studied to mimic the dominant surfactant composition in fine SSA (diameter ≤ 2.5 μm). PA and SA constitute about two-thirds of the saturated fatty acids in fine SSA, and MA is the third most abundant species.[53] The aqueous core of nascent SSA is modeled by a 0.4 M NaCl subphase at pH 8.2[1], and aged SSA is modeled with the aqueous NaCl subphase adjusted to pH 5.6 and 2.0.[250] Surface pressure–area ($\Pi - A$) isotherms are conducted to measure the SSA proxy film phase behavior, and Brewster angle microscopy (BAM) images of the SSA proxy film collapse are taken at each pH. Differences in monolayer phase behavior and collapse between the SSA proxy film and its individual components are observed, highlighting the importance of using more complex model systems to

elucidate atmospherically-relevant SSA film behavior. Additionally, changes in SSA film collapse mechanisms as a function of pH are measured. From our results, we expect that subphase composition and pH will play a major role in modulating SSA film morphology which will then impact particle trace gas uptake and nucleation ability in the MBL.

3.2 Materials and Methods

3.2.1 Materials

Myristic acid ($C_{14}H_{28}O_2$, MA, $\geq$ 99%, Sigma-Aldrich, Saint Louis, MO, USA), palmitic acid ($C_{16}H_{32}O_2$, PA, $\geq$ 99%, Sigma-Aldrich), and stearic acid ($C_{18}H_{36}O_2$, SA, $\geq$ 99%, Sigma-Aldrich) were used without further purification. Each fatty acid was dissolved in chloroform (HPLC Grade, Fisher Scientific, Fair Lawn, NJ, USA) at a concentration of 3 mM. Aliquots of the individual fatty acid solutions were mixed according to the molar ratio of 2 MA:4 PA:3 SA to produce the mixed lipid stock solution in duplicate. NaCl (Sodium chloride, 99+%, ACS reagent, Acrōs Organics, Fair Lawn, NJ, USA) was baked at 650 °C in a furnace (Fisher Scientific Isotemp® Muffle Furnace, Dubuque, IA, USA) for at least 10 h to remove residual organics.[251] The salt was dissolved in ultrapure water with a resistivity of 18.2 MΩ·cm (Milli-Q Advantage A10, EMD Millipore, Billerica, MA, USA) and with a pH of 5.6 because of acidification by atmospheric CO_2. Acidic subphases were prepared at pH 2.0 via the addition of HCl (Hydrochloric Acid, TraceMetal™Grade, Fisher Scientific). Only the 0.4 M NaCl solution could be adjusted to pH 8.2 via NaOH (Sodium Hydroxide Pellets, Mallinckrodt Analytical Reagent, Paris, KY, USA) addition. Water at pH 8.2 acidified rapidly over the course of an experiment, but the 0.4 M NaCl solution acidified more slowly. Therefore, the solution was initially prepared at pH 8.5 so that the pH would drop to 8.2 $\pm$ 0.1 while data was recorded.

3.2.2 Surface Pressure–Area Isotherms

Surface pressure–area ($\Pi - A$) isotherms were performed in triplicate on a Teflon Langmuir Mini-Micro trough (KSV NIMA, Biolin Scientific, Espoo, Finland, area 144.5 cm^2) and Delrin barriers (KSV NIMA). Both the trough and barriers were thoroughly cleaned with reagent alcohol (Histological Grade, Fisher Scientific, Fair Lawn, NJ, USA) and ultrapure water. Surface pressure was measured by the Wilhelmy plate method using a filter paper plate (Ashless Grade 41, Whatman, GE Healthcare, Chicago, IL, USA), and the paper plate was fully wetted prior to running an isotherm. The barriers were swept across the surface at the maximum compression speed (270 mm/min/barrier) to check for surface cleanliness, indicated by a surface pressure value $\leq$ 0.20 mN/m. A microsyringe (50 μL, Hamilton, Reno, NV, USA) was used to spread the lipid solution dropwise onto the aqueous subphase. Ten minutes were allowed for solvent evaporation, and then the monolayer was symmetrically compressed at a rate of 10 mm/minute (5 mm/min/barrier). All $\Pi - A$ isotherms were conducted at 21.8 $\pm$ 0.5° C and a relative humidity of 37 $\pm$ 6 %. Relative humidity is not expected to change the monolayer collapse mechanism.

3.2.3 Brewster Angle Microscopy (BAM)

Brewster angle microscope images were collected simultaneously with $\Pi - A$ isotherms using a custom-built BAM setup similar to that described previously in the literature.[192,252] Plane-polarized light at 543 nm was produced by a 1.5 mW He-Ne laser source (Meredith Instruments, Peoria, AZ, USA) with linear 500:1 polarization, and the *p*-polarized light was further purified by a Glan-laser calcite polarizer (Thorlabs, Newton, NJ, USA). The BAM was built on a goniometer and positioned along the Brewster angle of the air/water interface at 53.1°. Reflected light was then sent through a 10X infinity-corrected super long working distance objective lens (CFI60 TU Plan EPI, Nikon Instruments, Melville, NY, USA). The magnified image was fur-

ther collimated and focused using a tube lens (MXA22018, Nikon Instruments; focal length 200 mm) before being sent to the back-illuminated EM-CCD camera (iXon DV887-BV, Andor Technology USA, Concord, MA, USA; 512 × 512 active pixels, 16 μm × 16 μm pixel size). The BAM images were processed using ImageJ software (version 1.52a, National Institutes of Health, Bethesda, MD, USA)[253] and cropped from their original size of 8.2 × 8.2 mm to show only the region of highest resolution.

3.3 Results and Discussion

3.3.1 Nascent SSA Proxy Film Phase Behavior

Although cations tend to be enriched in SSA relative to their concentrations in seawater, Na^+ is not enriched.[5,78] Consequently, 0.4 M NaCl was added to the $\Pi - A$ isotherm subphase to model the Na^+ ion concentration in seawater in order to understand how the aqueous core of SSA impacts lipid organization in its organic coating.[1,254] Additionally, the pH of the subphase was adjusted to mimic that of seawater at pH 8.2.[1] $\Pi - A$ isotherms of the SSA proxy film (2 MA: 4 PA:3 SA) and its individual fatty acid components on 0.4 M NaCl at pH 8.2 are shown in Fig. 3.1. A BAM image of the SSA proxy monolayer collapse is also displayed as an inset in Fig. 3.1a. Fatty acid mixtures containing different chain lengths have been previously shown to be fully miscible[255], so the the SSA proxy film should be entirely homogeneous. However, isotherms of the individual fatty acids were measured to evaluate how their phase behavior differs from the SSA proxy film mixture. If differences are observed in phase behavior, this suggests that individual fatty acid monolayers do not fully capture MBL SSA surface organization and dynamics.

The SSA proxy monolayer (Fig. 3.1a) undergoes a 2D phase transition from a gas–tilted condensed (G-TC) coexistence phase to a tilted condensed (TC) phase at 24 Å^2/molecule, known as the lift-off point.[113,256,257] Upon further compression in the

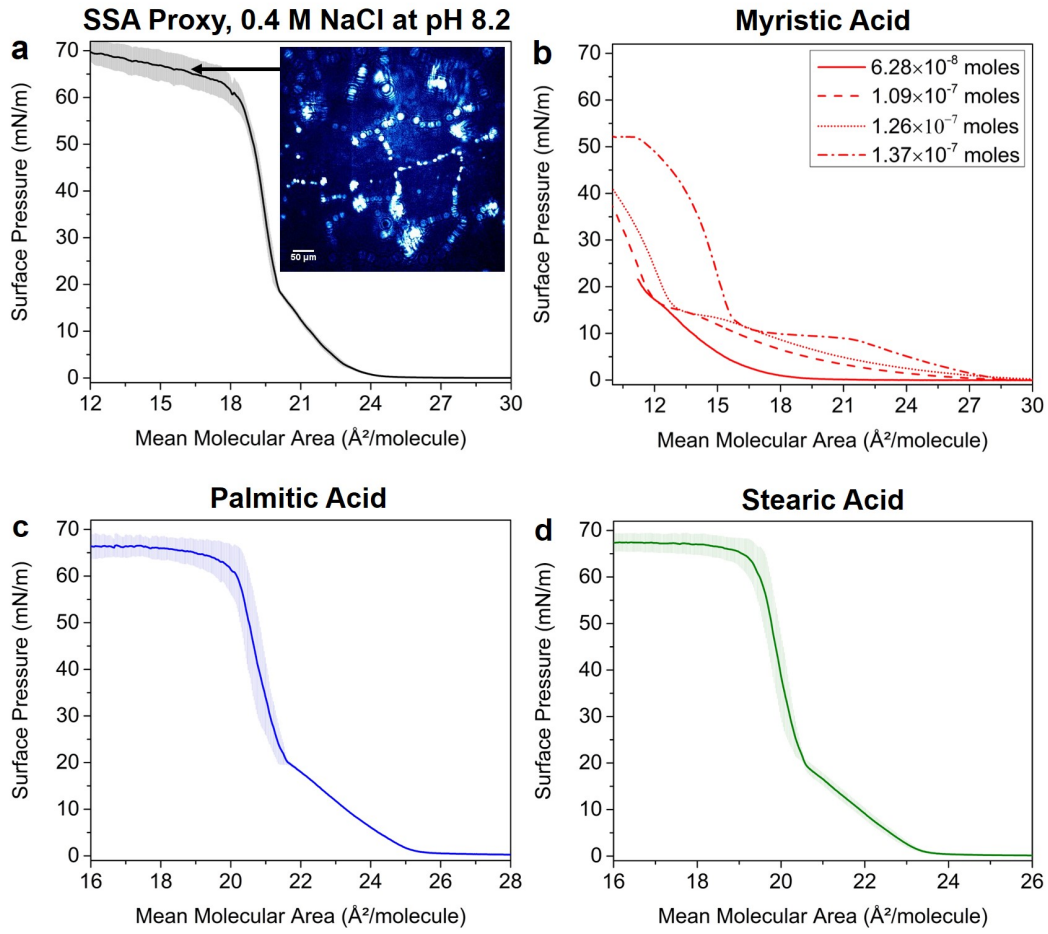

Figure 3.1: $\Pi - A$ isotherms of the sea spray aerosol (SSA) proxy film and its individual components at pH 8.2: **(a)** SSA proxy film and a Brewster angle microscope (BAM) image of the monolayer collapse; **(b)** myristic acid (MA) spread at different amounts at the air/water interface; **(c)** palmitic acid (PA); and **(d)** stearic acid (SA). The BAM image scale bar is 50 μm.

TC phase, the monolayer transitions into the untilted condensed (UC) phase at a surface pressure of 18 mN/m. The film reaches a maximum surface pressure around 70 mN/m. The existence of only one collapse pressure (Π_c) observed at ~60 mN/m also suggests that the SSA proxy film is completely miscible. A monolayer containing immiscible components have different Π_c points for each component, whereas miscible monolayers have a single Π_c that is dependent upon the molar fraction of each component in the mixture.[113,243] Such a high Π_c indicates that the SSA film on model seawater is resistant to collapse. This phase behavior could be caused in part

by Coulombic repulsion between the negatively-charged carboxylate moieties and by contact ion pair formation between the carboxylate and Na^+ cation.[67] Alternatively, a surface pressure plateau could be the result of slow relaxation kinetics caused by strong cohesive forces between the lipids.[236] Further insight into the intermolecular interactions contributing to the surface pressure plateau can be obtained from the individual fatty acid isotherms.

MA (Fig. 3.1b) is the shortest of the long chain fatty acids, yielding a smaller sum of dispersion interactions between the lipids. As a result, MA films at the air/water interface are more disordered and pack less tightly.[113,157,258] MA is partially soluble in water,[237,238] and its rate of desorption increases with carboxylic acid headgroup deprotonation because of the strong electrostatic interactions between the carboxylate moiety and water molecules. MA is largely deprotonated at pH 8.2 based on the surface pK_a value of 7.88 at 20° C,[241] so a stable monolayer could not be obtained for the model seawater subphase due to dissolution. Increasing the amount of fatty acid spread onto the air/water interface helped to overcome the diffusion-mediated desorption, but the mechanical forcing from lateral barrier compression during the $\Pi - A$ isotherm experiment promoted desorption. Hence, the monolayer was not stable, so collapse could not be reached.

Both PA (Fig. 3.1c) and SA (Fig. 3.1d) achieve a surface pressure plateau at collapse around ∼67 mN/m on 0.4 M NaCl at pH 8.2. PA and SA should be partially deprotonated on this model seawater subphase given their surface pK_a values of 8.34 at 20° C and 9.89 at 20° C, respectively.[241] However, the lipids are largely insoluble because of the greater dispersion interactions between the alkyl chains which generates a more rigid film. The PA lift-off point was measured at 25.5 $Å^2$/molecule, and SA lift-off occurred at 23.5 $Å^2$/molecule. PA and SA underwent the tilted condensed–untilted condensed (TC–UC) phase transition at ∼20 mN/m. PA and SA $\Pi - A$ isotherms are similar to the SSA proxy isotherm, suggesting that the mixture film

dynamic behavior resembles that of the individual fatty acids. The SSA proxy lift-off point is intermediate between the PA and SA lift-off points, further supporting that the monolayer mixture is miscible. Miscible monolayers have phase transitions that are dependent upon the molar fraction of each component in the mixture; thus, the monolayer mixture lift-off occurs at a pressure between that of its individual components.[113,243] While PA and SA monolayers are good models of SSA film behavior on 0.4 M NaCl at pH 8.2, the SSA proxy monolayer has a different isotherm slope at collapse which could indicate small differences in the collapse mechanisms.

SSA film rigidity partially governs the monolayer collapse mechanism into 3D structures. Fluid monolayers lose material by desorption into the aqueous subphase and have low Π_c. Rigid or highly ordered monolayers tend to collapse by forming multilayer aggregates in the air phase or by desorption into the aqueous phase, and the Π_c is often high. When the monolayer possesses intermediate rigidity, it can buckle and form protrusions into the subphase, known as a folding collapse. Defects in the monolayer act as folding nucleation sites, leading to random protrusions that coexist with the monolayer. Continuous compression after protrusion formation increases the fraction of monolayer in the folds relative to the flat regions such that a constant Π_c is maintained. Monolayer folding is a reversible process unlike film desorption and fracturing, so the monolayer molecular organization is maintained throughout dynamic compression and expansion.[116–118,249,259] Changes in film morphology can affect SSA uptake of trace gases and water vapor in the MBL, so understanding SSA film collapse mechanisms is important for better predictions of SSA radiative effects and surface reactivity in climate models.

BAM was used to visualize the SSA proxy collapse structure that gives rise to the surface pressure plateau on 0.4 M NaCl at pH 8.2 (Fig. 3.1a). Small white spots approximately 5–10 μm in diameter appeared in the condensed phase at surface pressures below the Π_c (image not shown). These spots are indicative of monolayer-bound

vesicle budding.[260] At Π_c, bright white lines began to encompass many of the budding vesicles, and further compression caused the lines to become more interconnected. The presence of lines suggest a folding collapse mechanism in which the budding vesicles are likely incorporated into the folds.[118,260–262] A surface pressure plateau is also indicative of monolayer folding. Film material is incorporated into the folds with compression, and the surface pressure rises only minimally because molecular organization within the film itself does not change. Instead, the surface pressure slowly rises as new folding nuclei form upon compression.[118] This suggests that nascent SSA films are resistant to collapse into 3D structures and may be able to retain their molecular organization during dynamic compression. SSA particle shrinkage could then create an even greater aerosol surface-to-volume ratio due to film folding at the interface.

3.3.2 Effects of SSA Proxy Aqueous Composition on the Film Phase Behavior

In order to understand how SSA interfacial organization changes throughout SSA residence in the MBL, the 0.4 M NaCl aqueous subphase pH was lowered to 5.6 in the $\Pi - A$ isotherm and BAM experiments (Fig. 3.2). The SSA proxy monolayer lift-off point (Fig. 3.2a) occurs at 25 Å^2/molecule, and the film undergoes the TC–UC phase transition at ∼18 mN/m. A surface pressure plateau at collapse occurs at ∼64 mN/m. The Π_c on 0.4 M NaCl at pH 5.6 is slightly lower than the Π_c at pH 8.2 (Fig. 3.1a), indicating that the monolayer begins to fold at a lower surface pressure at pH 5.6. BAM also suggests that part of the SSA proxy monolayer on 0.4 M NaCl at pH 5.6 folds at collapse (inset in Fig. 3.1a). Small 3D nuclei begin to form in the UC phase just before the Π_c, and some of these nuclei become connected by thin white lines upon further compression at collapse. Line structures are indicative of monolayer folding.[118] However, a significant number of these small 3D nuclei do not coalesce into line structures, and the number of 3D nuclei increases with compression.

The lower collapse pressure at pH 5.6 is likely caused by a fraction of more rigid film material being incorporated into vesicles that detach from the monolayer, meaning that less of the film is incorporated into folds.[263] Changes in the SSA proxy film organization and fluidity on subphases with differing pH suggest that aerosol particle pH is important in modulating SSA film dynamics in the MBL.

While the SSA proxy monolayer folds at collapse, its individual fatty acid components do not fold on the same subphase conditions. MA (Fig. 3.2b) lifts off around 41 Å^2/molecule and enters a TC–UC coexistence phase[246,264,265] at ∼15 mN/m. The monolayer exists in the UC phase at surface pressures higher than 15 mN/m until the Π_c is reached at ∼48 mN/m, and then the surface pressure drops with further compression. PA (Fig. 3.2c) and SA (Fig. 3.2d) isotherms also exhibit a similar collapse mechanism to MA with Π_c values at ∼62 mN/m and ∼67 mN/m, respectively, and their surface pressures decrease after collapse. The other PA and SA phase transitions remain relatively unchanged in comparison to the individual fatty acid isotherms on 0.4 M NaCl at pH 8.2. The lift-off point is increased by 1 Å^2/molecule for both PA and SA at pH 5.6, and the TC–UC phase transition is increased by ∼2–3 mN/m for both fatty acids, suggesting that the monolayer is less fluid on salt water at pH 5.6 than on model seawater.

Both the $\Pi - A$ isotherms and BAM images demonstrate significant differences between the SSA proxy film collapse on aqueous NaCl as compared to ultrapure water (Fig. 3.3). A surface pressure plateau is observed at ∼64 mN/m on 0.4 M NaCl, whereas the Π_c on H_2O is ∼53 mN/m. Both line structures and 3D nuclei are observed in the BAM images on salt water, suggesting that NaCl introduces sufficient fluidity to promote a folding collapse mechanism. On water at pH 5.6 (Fig. 3.2 inset), the SSA proxy film initially forms small 3D nuclei at a surface pressure less than the Π_c. The 3D nuclei aggregate into larger, irregular structures upon reaching monolayer collapse. Both the formation of larger 3D aggregates and the

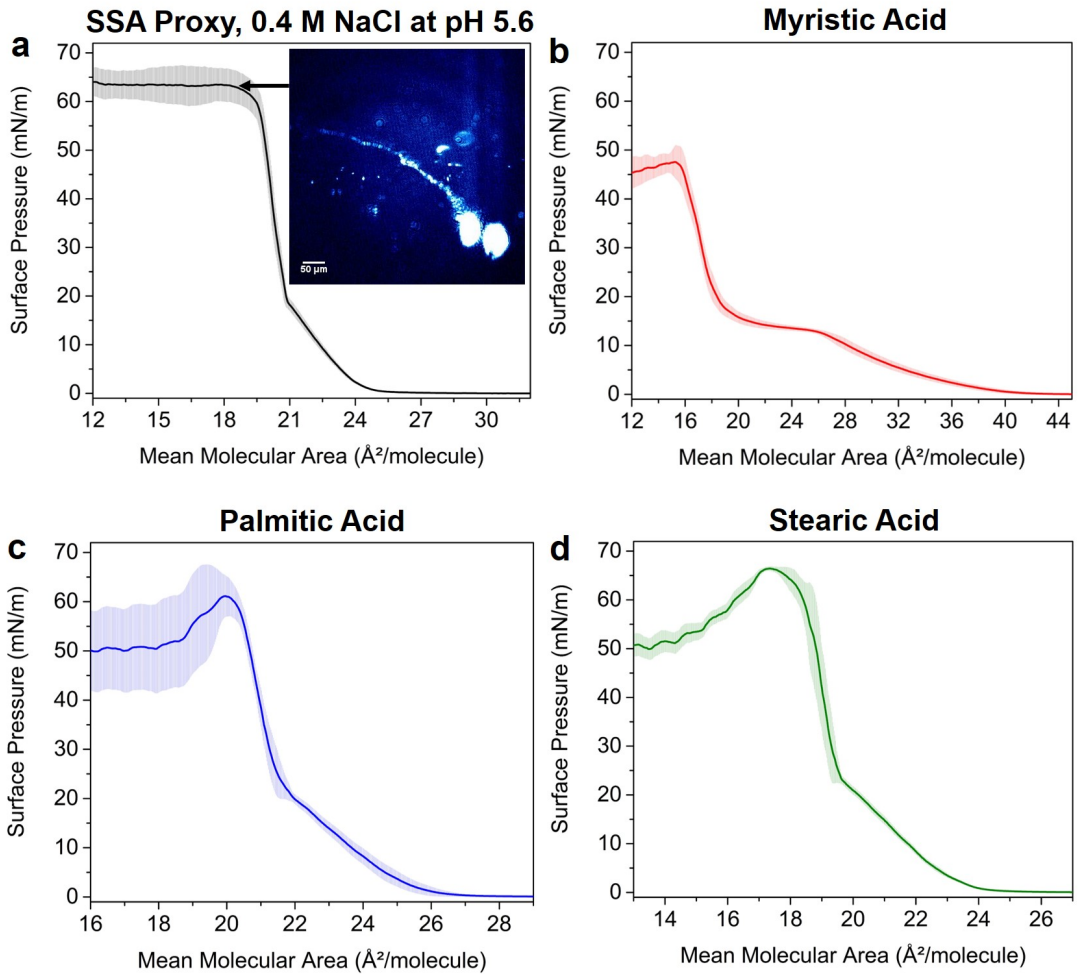

Figure 3.2: $\Pi - A$ isotherms of the SSA proxy film and its individual components at pH 5.6: **(a)** SSA proxy film and a BAM image of the monolayer collapse, **(b)** myristic acid (MA), **(c)** palmitic acid (PA), and **(d)** stearic acid (SA). The BAM image scale bar is 50 μm.

decrease in surface pressure following further compression indicates that the SSA proxy monolayer on water fractionates upon reaching Π_c. Although the monolayer is partially deprotonated at pH 5.6, the dispersion interactions between the alkyl chains are likely greater than the subphase–head group interactions. Consequently, the film is more rigid and readily breaks when the size and concentration of 3D nuclei becomes sufficiently large.[236] Thus, a folding collapse is likely water mediated and promoted by contact ion pair interactions between the carboxylate head group and Na^+ ion which fluidize the monolayer sufficiently.[67,266] At pH 5.6, the head groups are still

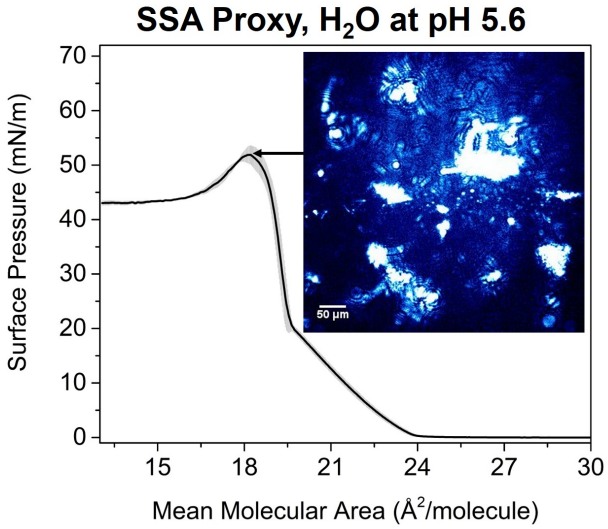

Figure 3.3: $\Pi - A$ isotherm of the SSA proxy film on H_2O at pH 5.6 and a BAM image of the monolayer collapse. The BAM image scale bar is 50 μm.

deprotonated such that these ion pairs form easily, but the partial protonation likely decreases the magnitude of these subphase-head group interactions which increases the rigidity of the film.

3.3.3 Aged SSA Proxy Film Phase Behavior

When the SSA proxy film is completely protonated on 0.4 M NaCl at pH 2.0, the $\Pi - A$ isotherm and BAM image indicate that the film no longer folds at collapse (Fig. 3.4). The lift-off point is significantly higher at 28 Å^2/molecule, caused by decreased MA solubility at low pH. Like the other SSA proxy isotherms, the TC–UC phase transition occurs around ∼20 mN/m. Upon monolayer collapse, the $\Pi - A$ isotherm reaches a Π_c of ∼58 mN/m before the surface pressure decreases. BAM images reveal that the film forms 3D nuclei 5–10 μm in diameter and that the nuclei do not aggregate even beyond the Π_c. This collapse structure suggests that the monolayer is too rigid to fold due to weaker subphase–head group interactions, so the film collapses into 3D vesicles. Consequently, SSA acidification in the MBL is expected to induce significant changes in film organization, particularly during seasons of high biological productivity.

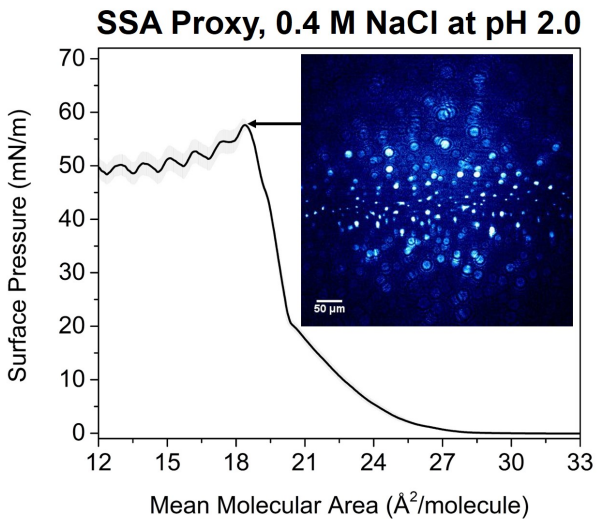

Figure 3.4: $\Pi - A$ isotherm of the SSA proxy film on 0.4 M NaCl at pH 2.0 and a BAM image of the monolayer collapse. The BAM image scale bar is 50 μm.

3.3.4 SSA Film Collapse Mechanisms and Their Atmospheric Implications

A comparison of the collapse pressures for the SSA proxy mixture and its individual fatty acid components on various subphase conditions is plotted in Fig. 3.5. Resistance to a 2D to 3D transformation increases with increasing pH. The SSA proxy mixture on 0.4 M NaCl exhibits the highest Π_c at pH 8.2, and the Π_c steadily decreases with subphase acidification. However, the Π_c of the SSA proxy film on ultrapure water at pH 5.6 is significantly lower than that of the film on salt water at the same pH, indicating that both salt and pH are important in stabilizing the 2D monolayer at the air/water interface. Additionally, the strength of the dispersion interactions between the alkyl chains of the fatty acids are important in controlling film rigidity. MA exhibited the most fluid monolayer because of the weaker dispersion interactions, albeit the monolayer was unstable. SA was highly rigid as shown by the nearly identical collapse surface pressures at both pH 5.6 and 8.2. PA and SA had collapse surface pressures close to that of the SSA proxy mixture, but the individual fatty acids alone were not able to completely reproduce the collapse behavior at all pH

values. Therefore, while the lateral dispersion interactions are crucial in regulating film rigidity, the subphase–head group interactions modulated by pH and salt are the most important factors in determining the collapse mechanism for the SSA proxy film. Further studies are needed to evaluate how other marine-relevant salts and organic compounds impact the mechanical properties of the SSA proxy film.

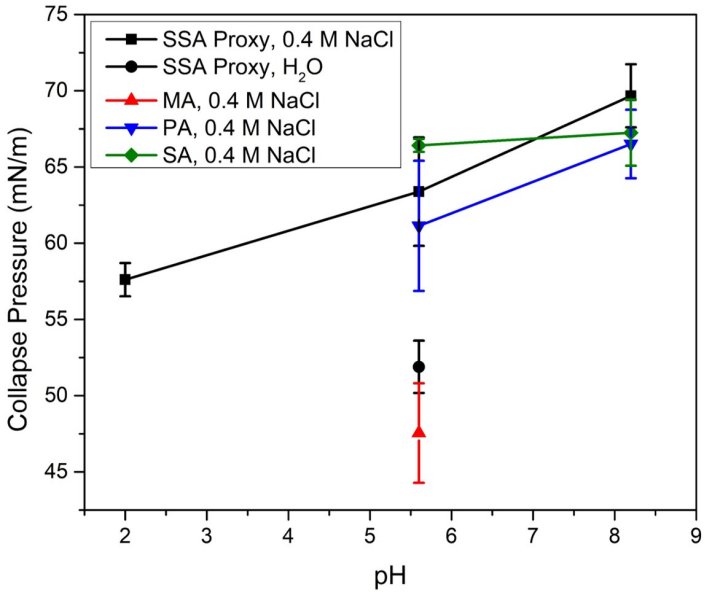

Figure 3.5: Collapse pressures of the SSA proxy film and its individual fatty acid components plotted as a function of subphase pH.

Probable film collapse mechanisms on SSA surfaces in the MBL are summarized in Fig. 3.6. The organic coating of nascent SSA is likely to fold upon particle contraction during periods of high marine biological activity. As a result, nascent SSA is dynamic and retains its interfacial molecular organization. However, as the particle interacts with trace gases in the MBL and acidifies, the film becomes more rigid. Monolayer folding is still observed, but 3D nuclei also begin to form at the surface as the interfacial area is reduced. Folding ceases when the monolayer is fully protonated, and only the 3D nuclei are observed. This change in collapse indicates that the SSA film fractionates and undergoes significant reorganization at low pH. Monolayers on acidic subphases, such as the films on aged SSA, are less dynamic and less resistant

to 3D transformations, so some film material is removed from the surface when the available area is too small. It is therefore reasonable to assert that interfacial reactivity and the nucleation ability of SSA particles change as the interfacial molecular environment is altered via pH and salt concentration, thereby yielding different impacts on climate upon aerosol aging in the MBL. The studies described herein reveal interfacial morphological changes of complex SSA proxy systems as a function of pH to better understand SSA surfaces.

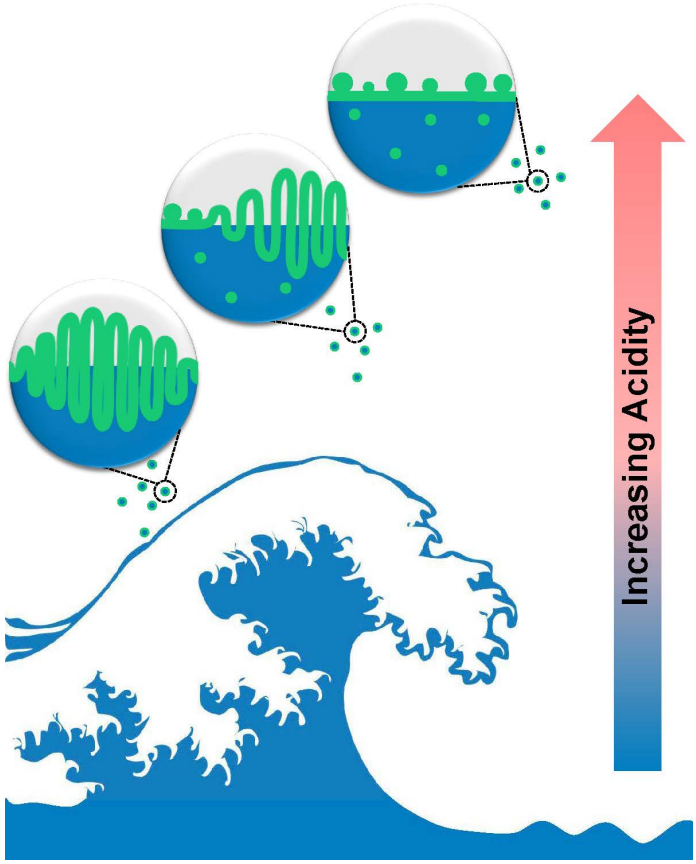

Figure 3.6: Illustration of the proposed SSA proxy film collapse mechanisms throughout particle residence in the marine boundary layer (MBL). Increased acidity is associated with longer aging in the MBL. The light gray circles correspond to zoomed-in schematics of the collapsed SSA proxy film. Nascent SSA films (bottom circle) fold at collapse. Upon subphase acidification (middle circle), the collapsed film folds and forms 3D nuclei simultaneously. After a significant amount of aging (top circle), the film no longer folds and only forms 3D nuclei at collapse.

Chapter 4

Vibrational Excitons Conceal Surfactants at the Air/Water Interface

4.1 Introduction

Elucidating structure at the air/water interface is important to understanding chemical reactivity in biological, environmental, and industrial systems. Surfactants comprise an abundant class of amphiphilic molecules that partition at the air/water interface with vibrational modes that are typically well-separated from those of water, offering a sensitive probe of interfacial adsorption and organization via vibrational spectroscopy.[98] Moreover, surfactant molecules spontaneously aggregate into micelles at high concentrations,[88] and strong vibrational couplings play a central role in the spectra of self-aggregating nanostructures.[267] Vibrational excitons emerge from the coupling of quasi-degenerate vibrational states and have the effect of depleting local signal intensity in one-dimensional (1D) spectroscopic measurements.[268] Even though *global* infrared intensity is conserved by a sum rule, the apparent depletion of local signal strength can lead to misinterpretation of the results of 1D-IR experiments. The effects of exciton coupling on 1D-IR spectra have been well documented in bulk liquid water, proteins, and DNA; but the influence of the air/water interface on these

couplings has yet to be explored.[269–275]

Two-dimensional (2D) vibrational spectroscopic techniques are the only methods immune to this problem because they probe vibrational coupling directly, although the resulting spectra are sometimes too convoluted to analyze. To date, only three studies have investigated vibrational coupling between alkyl chains of a surfactant monolayer.[276–278] Bredenbeck *et al.*[276,277] first observed vibrational coupling between the terminal methyl and methylene groups of a dodecanol monolayer at the air/water interface using 2D vibrational sum frequency generation spectroscopy (VSFG). A wealth of structural information is present within the off-diagonal C–H peaks in 2D vibrational spectra, but accessing many of these details can be unintuitive.

One-dimensional vibrational spectroscopic techniques such as surface-sensitive infrared reflection-absorption spectroscopy (IRRAS) and surface-selective VSFG are simpler to dissect than their 2D analogues and have been much more widely adopted for the analysis of surfactant organization at interfaces. Soluble surfactant adsorption and film surface density are measured through vibrational band peak intensities in which hydrocarbon C–H and C–D modes are most commonly tracked.[109,168,179,279,280] The orientation of surfactant terminal methyl groups is frequently assessed via 1D VSFG and by calculating ratios of CH_3 peak intensities obtained by probing the system with different polarizations of light.[68,281] An analogous analysis using the CH_2 peak intensities from 1D IRRAS spectra is used to assess hydrocarbon chain conformational order at interfaces.[63,154,157,282] A method was recently developed to estimate the total intermolecular interactions in a surfactant monolayer at the air/water interface using the intensity ratio amplitude of the second-order Fermi resonance signals generated by VSFG.[283] All of the above analyses rely upon alkyl chain peak intensities, which are susceptible to signal strength reduction via vibrational coupling.

To investigate the influence of vibrational excitons on 1D vibrational spectra, IRRAS spectra and surface tension measurements of perfluorooctanoic acid (PFOA)

at the air/water interface were collected, and the experimental data was compared to theoretical spectra generated from molecular dynamics (MD) simulations combined with an *ab initio* vibrational exciton model (*ai*VEM). Both theory and experiment reveal signal intensity depletion in the C–F vibrational modes at PFOA concentrations near but below the critical micelle concentration. Signal depletion due to vibrational excitons is also observed in the C–H peaks of an insoluble arachidic acid monolayer upon lateral compression, suggesting that the formation of vibrational excitons is a general feature of 1D vibrational spectra of surfactants at interfaces. This study therefore serves as a cautionary tale against structural analyses using alkyl- and fluoroalkyl-chain vibrational mode peak intensities.

4.2 Methods

4.2.1 Chemicals

Pentadecafluorooctanoic acid (PFOA, 96%, ACROS Organics™) and arachidic acid (AA, $\geq$ 99%, Sigma-Aldrich) were used as received. All glassware was cleaned in a piranha acid bath. Solutions were prepared in ultrapure water with a resistivity of 18.2 MΩ·cm (Milli-Q Advantage A10, EMD Millipore), and NaCl (Sodium chloride, 99.5%, for biochemistry, ACROS Organics™) was baked in a furnace at 650° C for at least 10 h to remove residual organic impurities.[284] PFOA was dissolved in ultrapure water and in an aqueous 0.47 M NaCl solution, and the pH of all PFOA solutions was measured at 5.8 ± 0.1 due to acidification by atmospheric CO_2. AA was dissolved in chloroform (Reagent ACS, 99.8+%, ACROS Organics™) at 1.0 mM. The ultrapure water and 0.47 M NaCl aqueous solution subphases for AA measurements contained 4 μM ethylenediaminetetraacetic acid (EDTA, 99.995% trace metals basis, Sigma-Aldrich) and were pH adjusted with sodium hydroxide pellets (NaOH, 98%, extra pure, ACROS Organics™) to pH 12.5 ± 0.1.

4.2.2 Surface Tensiometry

PFOA surface tension measurements were collected in borosilicate glass petri dishes using a force tensiometer (Sigma 703D, Biolin Scientific) and the Wilhelmy plate method. A platinum Wilhelmy plate was cleaned with ethanol and ultrapure water and fired until red hot with a Bunsen burner. PFOA solution surfaces were allowed to equilibrate for 3 minutes prior to recording the surface tension, and all measurements were repeated at least five times. Curve fitting of Eq. (2.5) was performed using the Nonlinear Curve Fit Tool in OriginPro 9.0 (OriginLab 9).

Surface pressure-area isotherms of AA were conducted in triplicate using a Teflon Langmuir trough and Delrin barriers (Biolin Scientific), and surface tension was measured with a platinum Wilhelmy plate. Surface cleanliness, indicated by a surface pressure value $\leq$0.2 mN/m, was assessed by sweeping the barriers across the subphase at the maximum compression speed (270 mm/min/barrier). AA was spread dropwise onto the aqueous subphase, and the chloroform solvent was allowed to evaporate for 10 minutes. The barriers were symmetrically compressed at a rate of 5 mm/min/barrier during the isotherm, and the data were averaged.

4.2.3 Infrared Reflection-Absorption Spectroscopy

Infrared-reflection absorption spectroscopy (IRRAS) was conducted using a Fourier transform infrared spectrometer (Spectrum 100, PerkinElmer) equipped with a liquid nitrogen-cooled HgCdTe (MCT) detector. Spectra were collected with unpolarized light in the single-beam mode as an average of 400 scans. The incident beam direction inside the spectrometer was modified by a planar gold mirror at a 48° angle of incidence relative to surface normal, and the reflected light was redirected toward the detector with a second gold mirror. Energy values were recorded every 0.5 cm^{-1} between 450 and 4000 cm^{-1}, and the spectral resolution was 4 cm^{-1}. Each experiment was repeated in at least triplicate and analyzed using OriginPro 9.0. For analysis

of the PFOA C–F vibrational modes, the baseline was subtracted from each spectrum by fitting a line between endpoints 1118 and 1266.5 cm^{-1}, and the peak area of each baseline-subtracted spectrum was integrated between these endpoints. The C–H spectral region of AA was baseline-subtracted by fitting a line between endpoints 2800 and 3000 cm^{-1}, and the peak area was integrated between the same endpoints. Figures contain averaged, baseline-subtracted spectra.

4.2.4 Second Harmonic Generation Spectroscopy

A custom-built SHG spectrometer was used for these measurements, and the instrument design has been described previously.[195] Sub-50 fs pulses centered at 805 nm were generated using an ultrafast oscillator (Tsunami, Spectra-Physics) with an output power of ∼900 mW and a repetition rate of 82 mHz. A beam splitter directed 90% of the laser output power into a signal channel, and the remaining 10% was directed to a reference channel where a BBO crystal (90015087, Newport) generated the reference SHG signal. The signal channel consisted of a Glan-laser polarizer (10GR08-AR16, Newport), a half-wave plate (10RP52, Newport), and a long-pass filter (690LP RapidEdge, Omega Optical). Linear *p*-polarization was selected for the incoming beam polarization to maximize the measured signal intensity. The laser pulses were focused onto the aqueous surface, and the reflected SHG photons were collimated through a focusing lens. The collimated signal then passed through two short-pass filters (450SP RapidEdge, Omega Optical), a half-wave plate (WPH10M-405, Thorlabs), and a Glan-laser polarizer (GLB10-405, Thorlabs). Linear *p*-polarization was also selected for the SHG signal polarization for maximum signal intensity. A silica plate aligned the reference beam parallel with the signal beam, and both beams were focused through a monochromator slit (Shamrock 303i, Andor) and onto an EMCCD camera (Newton DU970N-BV EMCCD, Andor). Second harmonic images were collected with an exposure time of 90 s and 200× electron multiplication. The CCD

background intensity was subtracted from the SHG signal and reference intensities, and the SHG sample signal was normalized to the reference. The normalized SHG signal intensities were then converted to electric field values by taking the square root of the intensity values. The SHG electric field data points plotted in Fig. 4.2 are the averages of triplicate measurements, and the error bars represent one standard deviation from the mean.

4.2.5 Brewster Angle Microscopy

A custom-built BAM setup is equipped with a 1.5 mW He-Ne laser (Meredith Instruments) mounted to a goniometer that positions the laser at the Brewster angle of the air/water interface, 53.1° relative to surface normal. The laser outputs 543 nm light with linear 500:1 polarization, and the *p*-polarized light is further purified by a Glan-laser calcite polarizer (Thorlabs). The light reflected from the air/water interface is directed through a 10X infinity-corrected super long working distance objective lens (CFI60 TU Plan EPI, Nikon Instruments) followed by a tube lens (MXA22018, Nikon Instruments; focal length 200 mm) to collimate and focus the light at the back-illuminated EM-CCD camera (iXon DV887-BV, Andor Technology USA; 512 × 512 active pixels, 16 μm × 16 μm pixel size). BAM images were cropped from their original size of 8.2 × 8.2 mm using ImageJ software[253] to show the region of highest resolution.

4.2.6 Molecular Dynamics

AMOEBA parameters for anionic PFOA were obtained by Kevin Carter-Fenk (Herbert group) using a standard protocol as described in his dissertation (2021) and in Ref. 285. Simulations were carried out in the canonical ensemble using slab boundary conditions, with a simulation cell size of 9.5 × 9.5 × 29.5 nm^3. The temperature was maintained every 0.1 ps at 298 K using a Bussi thermostat,[286] with a step size

of 2 fs maintained via the RESPA integrator.[287] All simulations were run using a locally-modified version of Tinker-HP, v. 1.1.[288] Our neat water simulations contain a 1:1 ratio of Na^+:PFOA in order to maintain charge neutrality for application of periodic boundary conditions via Ewald summation. NaCl simulations use a 3:1 ratio of Na^+:PFOA and 2:1 Cl^-:PFOA ratio to achieve charge balance, for a net 2:1 concentration ratio of NaCl:PFOA. The net concentration of PFOA was set to 200 molecules in a 9.5 nm^3 box, with enough water to provide a density of ≈ 1 g/cm^3.

4.2.7 Quantum Chemistry Calculations

Vibrational spectra of PFOA were obtained by Kevin Carter-Fenk (Herbert group) using a vibrational exciton model as described in his dissertation (2021) and in Ref. 285. The exciton model requires normal mode frequencies and transition dipole moments for each monomer. These are computed at the EDF2/6-31G(d) level[289] (using Q-Chem v. 5.3),[290] and scaled by a factor of 0.9805.[291]

4.3 Results and Discussion

4.3.1 PFOA Adsorption Measurements

Vibrational exciton formation in soluble surfactant films at the air/aqueous interface of ultrapure H_2O and 0.47 M NaCl solution was studied with surface-sensitive IRRAS. The specific concentration of NaCl was chosen to match the Na^+ concentration in seawater, and the soluble surfactant PFOA [$CF_3(CF_2)_6COOH$] was selected due to its surface activity and large perfluoroalkyl transition dipole moments. Additionally, PFOA is a strong acid ($pK_a < 1$ by recent estimates),[292,293] so the surfactant is fully deprotonated in the bulk and at the surface of ultrapure water (pH = 5.8). IRRAS spectra are analyzed in the C–F region ($\sim$1100–1300 cm^{-1}) and the spectra

are plotted as reflectance-absorbance (RA),

$$\mathrm{RA} = -\log\left(\frac{R_\mathrm{m}}{R_0}\right), \tag{4.1}$$

where R_m is the reflectivity of the PFOA film and R_0 is the reflectivity of the aqueous subphase without PFOA.

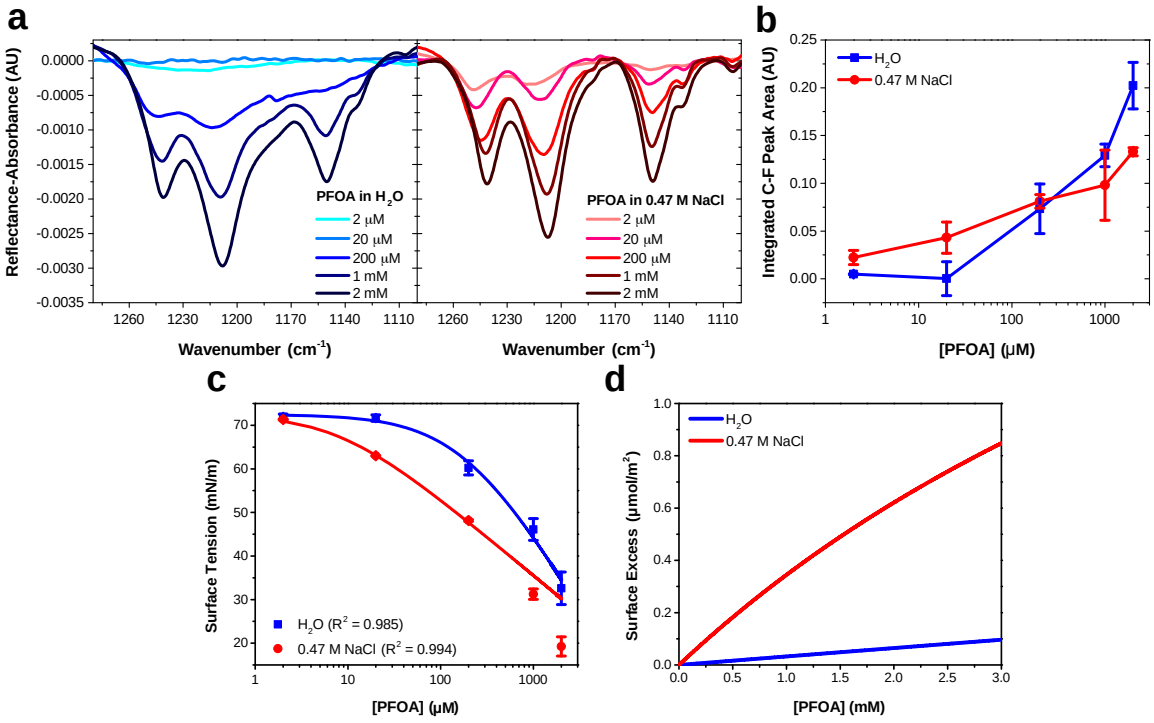

Figure 4.1: Perfluorooctanoic acid (PFOA) adsorption to the water and 0.47 M NaCl (aq) interface. (**a**) Infrared reflection-absorption spectroscopy (IRRAS) of the C–F vibrational mode region as a function of PFOA bulk concentration. (**b**) Integrated peak area corresponding to the C–F vibrational modes as a function of the bulk PFOA concentration. Lines connecting the data points are drawn to guide the eye. (**c**) Surface tension measurements as a function of PFOA bulk concentration. The curved lines connecting the data are fits to the Szyszkowski equation (Eq. 2.5) and the adjusted R^2 values are included in the legend. (**d**) The calculated PFOA surface excess (Eq. 2.7) as a function of bulk concentration. All error bars correspond to one standard deviation from the mean.

Three main peaks are present in the C–F vibrational mode region of the IRRAS spectra of PFOA in Fig. 4.1a. (Peak assignments are described in Appendix A.) The peaks red-shift with increasing bulk PFOA concentration, indicative of increasing adsorption and intermolecular interactions between interfacial PFOA molecules. The

aqueous subphase composition has a significant impact on the C–F peak intensities, lineshapes, and frequencies. For example, C–F peaks are not observable for PFOA dissolved in ultrapure water at 2 μM or 20 μM, suggesting that NaCl enhances PFOA adsorption at low concentrations. Peak integration of the C–F vibrational modes (Fig. 4.1b) further illustrates that NaCl enhances PFOA adsorption at low concentrations. A PFOA concentration of 200 μM brings about an inflection point in this trend wherein the integrated IRRAS peak area of the two aqueous solutions is nearly the same, and at concentrations $>$ 200 μM the integrated peak area actually becomes larger in H_2O than in 0.47 M NaCl.

In response to this apparent deviation from Hofmeister "salting-out" effects,[91,294] surface tension measurements were collected to further investigate PFOA interfacial adsorption and surface excess for comparison to the IRRAS spectra. Although surface tension does not provide any molecule-specific information, it does yield robust quantitative measurements of surfactant adsorption to the air/water interface. Enhanced surfactant concentration at the surface, relative to the bulk, results in a lower surface tension than that of H_2O and corresponds to a positive surface excess. The average surface tension of H_2O was measured at 72.57 $\pm$ 0.22 mN/m at 21.1 $\pm$ 0.5 °C, consistent with the reference surface tension values of 72.75 mN/m at 20 °C and 71.99 mN/m at 25 °C.[295]

Fig. 4.1c illustrates a surface tension depression with increasing bulk PFOA concentration. Surface tension measurements for each aqueous subphase solution were fitted to the Szyszkowski equation (Eq. 2.5).[103,104] The results of the fitting (Fig. 4.1c) show that the magnitude of surface tension depression induced by interfacial PFOA adsorption is highly dependent upon the presence of salt,[103,296–299] as the 0.47 M NaCl solution exhibits decreased surface tension across all bulk PFOA concentrations, relative to H_2O. To quantify the differences in PFOA surface excess induced by the aqueous subphase, the Langmuir-Szyszkowski equation (Eq. 2.7) was used to com-

pute the surface excess, Γ.[103,107] Fitted parameters a and b from Eq. 2.5 were used in Eq. 2.7 to obtain the calculated surface excess in Fig. 4.1d. The aqueous NaCl solution supports an order of magnitude larger PFOA surface excess than H_2O, with 10–12$\times$ the surface excess of H_2O for solutions containing 2 mM PFOA and 2 μM PFOA, respectively.

Second harmonic generation (SHG) spectroscopic measurements of the interfacial electric field (Fig. 4.2) also confirm enhanced PFOA surface activity in the NaCl solution, consistent with Hofmeister series "salting-out." Unlike hydrogenated alkyl surfactants, perfluorinated alkyl surfactants decrease the interfacial electric field relative to that of water.[300,301] Thus, as the PFOA interfacial concentration increases, the SHG electric field decreases. Aqueous NaCl enhances the surface activity of PFOA, leading to SHG electric field and surface tension depression as a function of PFOA bulk concentration. The interfacial electric field of PFOA in ultrapure water decreases minimally at 2 and 20 μM, matching the minimal decrease in surface tension shown in Fig. 4.1c. PFOA adsorption at the surface of both ultrapure water and 0.47 M NaCl aqueous solution converge upon a minimum SHG electric field value near 0.4 AU, suggesting PFOA saturation within the SHG probe region. However, the SHG signal also nears the limit of detection within this high PFOA concentration regime, making the full adsorption isotherm difficult to measure. Surface tension and infrared reflection-absorption spectroscopy (IRRAS) have deeper probe depths than SHG, so it is plausible that the SHG measurements are only sensitive to the first interfacial monolayer of PFOA. IRRAS interfacial probe depth corresponds to the IR penetration depth in water at the wavelengths of interest (Eq. 2.24), so the IR penetration depth is $\sim$ 19 μm in the C–F vibrational mode region.[302] Consequently, the IRRAS probe depth more closely matches that of the surface tension measurements than the SHG measurements, and the surface tension and IRRAS measurements likely detect multiple layers of PFOA interfacial adsorption.

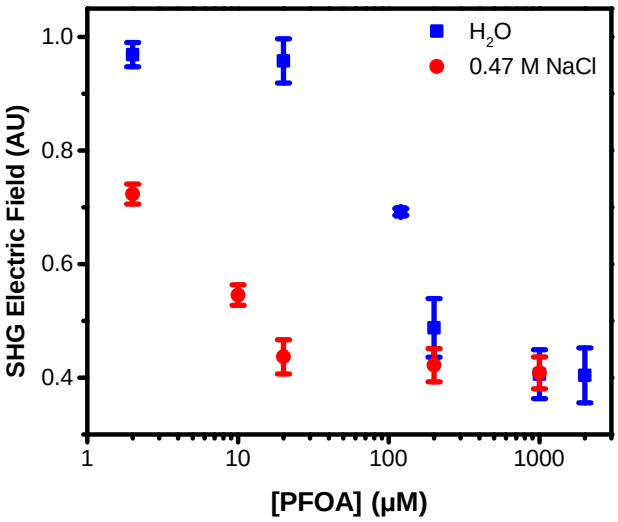

Figure 4.2: Second harmonic generation (SHG) spectroscopic measurements of perfluorooctanoic acid (PFOA) adsorption at the air-aqueous interface of ultrapure water and 0.47 M NaCl solution. Error bars represent one standard deviation from the mean.

While IRRAS is sensitive to changes in PFOA adsorption due to variable surfactant concentration and aqueous subphase composition, the spectroscopic measurements produce opposite trends relative to the surface tension measurements at concentrations of PFOA exceeding 200 μM. Surface tensiometry indicates that the NaCl subphase enhances PFOA surface adsorption relative to H_2O across all PFOA concentrations, whereas the IRRAS integrated C–F peak area implies that NaCl provides an initial enhancement of PFOA surface adsorption, followed by an anomalous decline in surface adsorption at PFOA concentrations $>$ 200 μM. Aggregation of PFOA could result in C–F vibrational coupling, explaining the surfactant concentration-dependent discrepancies between the IRRAS and surface tension data. The 0.47 M NaCl subphase also enhances shoulder features in the IRRAS spectra at 1133 cm^{-1} and 1105 cm^{-1}, which could be a signature of energy splittings characteristic of vibrational excitons.

The same anomaly was observed for IRRAS and surface tension measurements of PFOA interfacial adsorption to a 10 mM $CaCl_2$ subphase (Fig. 4.3). The PFOA

C–F modes are plotted in Fig. 4.3a, and the integrated peak area (Fig. 4.3b) is compared with that of PFOA in ultrapure water. As PFOA bulk concentration increases from 2 μM to 2000 μM, the C–F peak intensities increase. Additionally, the C–F peaks broaden and red-shift with increasing concentration, indicative of increased intermolecular interactions between interfacial PFOA molecules. Similar to the spectroscopic observations of PFOA adsorption to the 0.47 M NaCl aqueous solution interface, the Ca^{2+} cations salt-out the PFOA surfactants and increase PFOA surface activity at low concentrations, as shown by the greater integrated C–F peak areas for the aqueous $CaCl_2$ subphase at [PFOA] $<$ 1000 μM. At 1000 μM PFOA, the water and 10 mM $CaCl_2$ subphase integrated peak areas are approximately the same, and the integrated peak area of PFOA in water is greater than that of the aqueous $CaCl_2$ subphase at 2000 μM PFOA. The same trend reversal in the integrated C–F peak areas was observed between the water and 0.47 M NaCl (aq) subphases at PFOA concentrations exceeding 200 μM (Fig. 4.1b), indicating that the phenomenon is not specific to a particular salt or concentration.

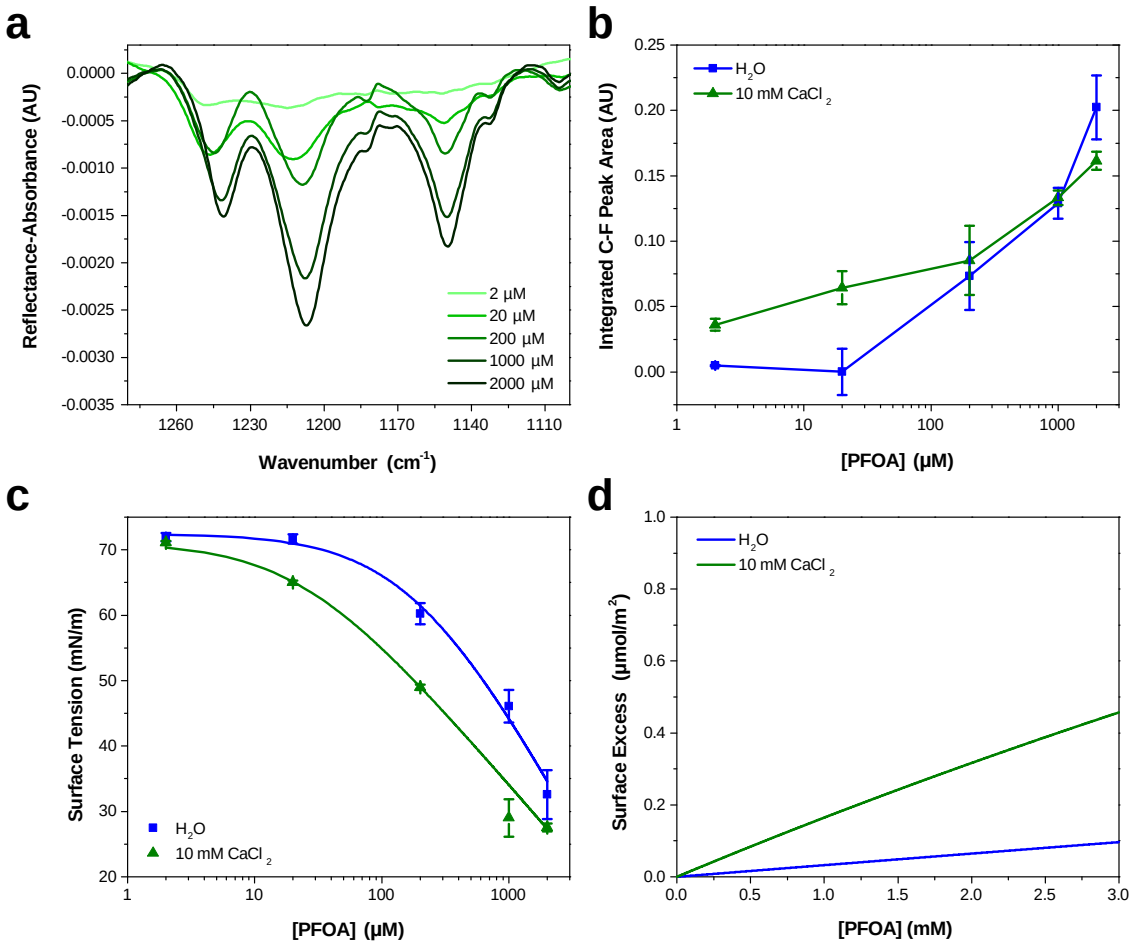

Figure 4.3: Perfluorooctanoic acid (PFOA) adsorption to the ultrapure water and 10 mM $CaCl_2$ aqueous solution interface. (**a**) Infrared reflection-absorption spectroscopy (IRRAS) of the C–F vibrational mode region as a function of PFOA bulk concentration. (**b**) Integrated peak area corresponding to the C–F vibrational modes as a function of the PFOA bulk concentration. Lines connecting the data points are drawn to guide the eye. (**c**) Surface tension measurements as a function of PFOA bulk concentration. The curved lines connecting the data points are fits to the Szyszkowski equation (Eq. 2.5). (**d**) Calculated PFOA surface excess from Eq. 2.7 as a function of bulk concentration. All error bars correspond to one standard deviation from the mean.

Surface tension measurements were conducted to further investigate the anomalous IRRAS measurements. Lowered surface tension values of the PFOA solutions relative to that of the aqueous subphase alone indicate surfactant interfacial adsorption. The surface tension of PFOA in 10 mM $CaCl_2$ aqueous solution was lower across all PFOA concentrations (2-2000 μM) relative to that of PFOA in water (Fig. 4.3c), indicating enhanced surface activity in the presence of salt. To better quantify PFOA ad-

sorption, surface excess was calculated from the Langmuir-Szyszkowski equation; the surface tension measurements of each aqueous subphase were fit to the Szyszkowski equation (Eq. 2.5), and the fitted parameters were used in Eq. 2.7 to obtain PFOA surface excess (Fig. 4.3d). PFOA surface excess in 10 mM $CaCl_2$ was approximately 5× greater than PFOA surface excess in H_2O. The PFOA surface excess in 0.47 M NaCl was approximately twice as large as the 10 mM $CaCl_2$ subphase surface excess, indicating that the Ca^{2+} ion has a significant effect on PFOA partitioning at the air/water interface despite the ionic strength of the NaCl solution subphase being over 15× greater than the $CaCl_2$ solution subphase ionic strength.

The surface tension measurements of PFOA in 10 mM $CaCl_2$ are in agreement with the IRRAS measurements at PFOA concentrations less than 1000 μM; however, the trends diverge at PFOA concentrations greater than 1000 μM. This discrepancy in the surface tension and IRRAS measurements at high PFOA concentrations was also observed between the 0.47 M NaCl and water subphases. Thus, the disagreement between surface tension and IRRAS measurements cannot be attributed solely to the ionic composition, concentration, or ionic strength of the aqueous solution. Instead, ions impact the intermolecular spacings between PFOA molecules, thereby modulating the extent of vibrational coupling between surfactants and the magnitude of IRRAS signal reduction in the C–F vibrational mode region.

The infrared cross section is examined to prominently exemplify deviations from the Beer-Lambert law (Fig. 4.4). In the absence of vibrational coupling, the integrated peak area would increase linearly with surface excess, allowing for the extraction of an effective infrared cross section from a linear fit of the data. The integrated peak area of PFOA in water is nearly linear with surface excess, suggesting nearly ideal "gas-phase" absorption behavior. However, even in neat water there are deviations from ideal absorption at higher concentrations, suggesting that this phenomenon is concentration dependent. This concentration dependence is amplified in the presence

of electrolytes, which induce significant nonlinearity in the C–F peak area as a function of PFOA surface excess. Concentration dependence could suggest that the deviations from ideal absorption are caused by PFOA$\cdots$PFOA interactions. The origin of these strong deviations from Beer-Lambert absorption is investigated in the context of the exciton hypothesis in the next section.

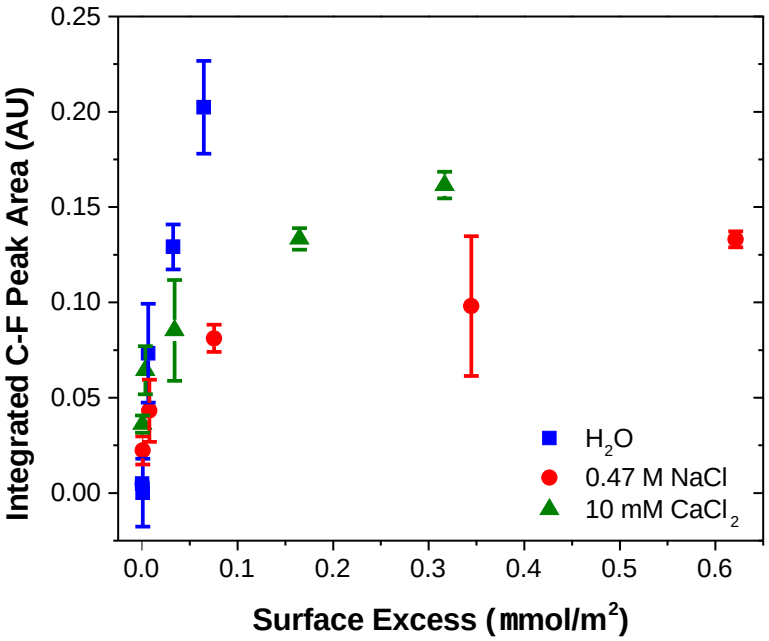

Figure 4.4: Integrated C–F peak area of infrared reflection-absorption spectroscopic (IRRAS) measurements of perfluorooctanoic acid (PFOA) surface excess at the air-aqueous interface of ultrapure water, 0.47 M NaCl, and 10 mM $CaCl_2$. Error bars represent one standard deviation from the mean.

4.3.2 Molecular Dynamics Simulations

In collaboration with the Herbert group, we begin the theoretical investigation by obtaining reliable structures of PFOA at the air/water interface using classical MD simulations based on the AMOEBA polarizable force field.[303] The equilibration timescale for aqueous PFOA is on the order of minutes (as implied by the measured surface tension equilibration time), well beyond the timescales accessible to simulation. In view of this, we allowed simulations of the neat water and NaCl (aq) interfaces to equilibrate for as long as computationally feasible (2.5 ns) to minimize deviations

from equilibrium.

The radial distribution function (RDF) between the terminal (CF_3) carbon atoms in PFOA is shown in Fig. 4.5. The initial peak at 7.5 Å is larger in the NaCl solution, implying that the PFOA tails are more structured in NaCl solution than in water. Neither the experiments nor simulations show any evidence of micellization; however a higher propensity for soluble surfactants to form micelles in saline solution is well documented,[87] supporting the notion that PFOA molecules aggregate more closely in the presence of NaCl. While we are not expressly concerned with micellization, the propensity for molecules to self-aggregate has important consequences for delocalization of the vibrational wavefunctions, as the vibrational couplings decay rapidly ($\sim R^{-3}$) with distance.

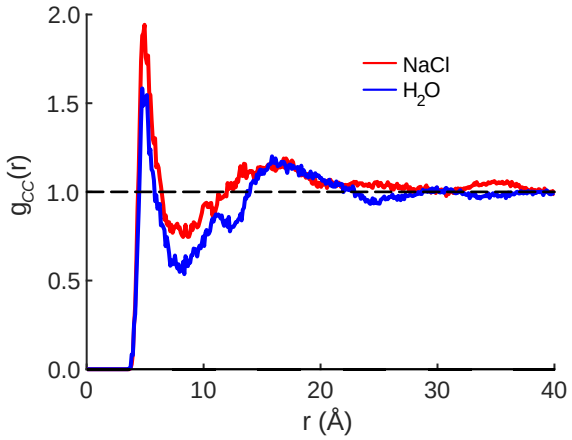

Figure 4.5: Radial distribution functions for the terminal (CF_3) carbon atoms in PFOA.

4.3.3 Vibrational Exciton Model Spectrum

We modeled vibrational excitons following the theoretical groundwork laid by others,[125,268,304] parameterizing our model with *ab initio* harmonic vibrational frequencies for PFOA, taken from 25 snapshots spanning 250 ps of MD simulation. We couple every vibrational mode of all 200 PFOA molecules at each snapshot via the *ab initio*-derived transition dipole moments. Non-interacting vibrational modes of each PFOA

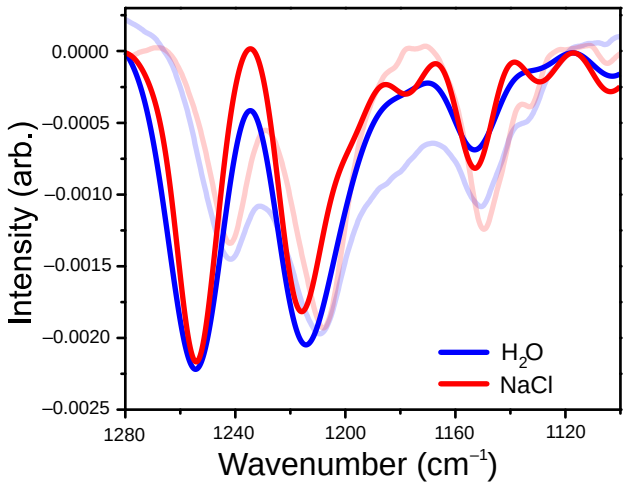

Figure 4.6: Exciton model spectra (opaque) overlaid with experimental spectra of 1 mM PFOA (transparent). Each band in the exciton spectra is plotted as a Gaussian lineshape, the width of which is set to the 2σ standard deviation in wavenumbers across 25 MD snapshots.

molecule are computed in vacuum and the couplings are computed without dielectric screening, yielding a final spectrum that reflects the intermolecular coupling of gas-phase PFOA monomers within a solution-phase distribution of positions. Solvent effects are omitted for simplicity, computational efficiency, and to gauge whether they are needed to reproduce the experimental spectrum. Vibrational coupling to the solvent is frequently invoked in cases of odd or difficult-to-explain spectral features, and use of a minimalist model allows us to probe whether coupling to the solvent is actually important.

The *ai*VEM spectra in Fig. 4.6 show exceptionally good agreement with experiment. All center wavelengths are in quantitative agreement (Table 4.1). Aside from the overestimate of the intensity of the high-energy band, the exciton model spectrum does a remarkable job of reproducing the fine details of the experimental spectrum, including asymmetry of the central band and the appearance of shoulders at 1180, 1130, and 1105 cm^{-1} that are all more pronounced in NaCl than in water. Importantly, the loss of intensity upon introduction of NaCl that is observed in the integrated peak areas is reproduced in the exciton model spectrum.

Table 4.1: Center Wavenumbers (in cm^{-1}) of Major Features in IRRAS Spectra of PFOA.

Subphase	ω_1			ω_2			ω_3		
	*ai*VEM	Expt.	Δ^a	*ai*VEM	Expt.	Δ^a	*ai*VEM	Expt.	Δ^a
H_2O	1254.0	1241.7	12.3	1214.0	1209.5	4.5	1153.0	1150.5	2.5
NaCl	1254.0	1242.0	12.0	1216.0	1208.0	8.0	1153.0	1149.7	3.3

[a]Absolute difference with respect to experiment ($\Delta = |\omega_{\,ai\text{VEM}} - \omega_{\text{expt}}|$).

Omission of solvent effects in the *ai*VEM allows us to isolate the origins of several important factors that influence the IRRAS spectra of PFOA. First, the appearance of shoulders in the NaCl spectrum is characteristic of exciton splitting and emerges due to vibrational coupling between C–F modes. These shoulders reflect a smearing out of the vibrational density of states by virtue of delocalization of the vibrational wavefunction. This means that vibrational bands with nearby shoulders (*e.g.*, the center band at ~ 1210 cm^{-1} and the low-energy band at ~ 1150 cm^{-1}) couple most strongly, as indicated also by their more dramatic changes in intensity between subphases. The intensity of the high-energy band changes the least between subphases, and does not appear to split or give rise to shoulders. This implies that the high-energy modes are spectators to the exciton delocalization. Emergence of shoulders and signal depletion in the experimental NaCl spectrum can both be attributed directly to vibrational excitons.

Combining the structural insights from MD simulations, experimental surface tension measurements, and the agreement of the *ai*VEM with experiment, the vibrational exciton hypothesis appears to be more likely than desorption of PFOA back into the aqueous subphase. This hypothesis explains the anomalous phenomena that are observed in IRRAS measurements of other soluble surfactants such as sodium dodecyl sulfate, where similar intensity decreases have been noted in the spectra of the C–H tails.[168] An important question remains as to whether vibrational excitons are unique to soluble surfactants, or if this phenomenon is generalizable to insoluble monolayers. This is addressed below.

The impressive agreement of the *ai*VEM with the PFOA experiments suggests that it is a useful tool with predictive capacity, but the C–F bonds in PFOA are rather exotic, making them poor surrogates for general trends in self-aggregating lipids at interfaces. As a model of the latter, we applied the *ai*VEM to a 2D sheet of 24 uniformly spaced octanoic acid ($C_8H_{16}O_2$) molecules, in an effort to hypothesize about the role of vibrational coupling in the 1D spectroscopy of C–H modes in an ordered monolayer at the air/water interface. The results (not shown) feature a lowering in the local intensity of the C–H vibrational modes upon compression from a diffuse monolayer to one corresponding to 5 Å mean molecular area. The prediction that vibrational coupling can induce distance-dependent signal reduction for an *insoluble* monolayer is next examined experimentally.

4.3.4 Arachidic Acid Monolayer Measurements

To determine if vibrational excitons can be observed in 1D vibrational spectroscopy of surfactants more generally, an insoluble arachidic acid (AA, $C_{20}H_{40}O_2$) monolayer was probed with IRRAS and surface tensiometry. AA forms a stable monolayer at the air/water interface (Fig. 4.9), even when over 95% of the carboxylic acid headgroups are deprotonated at pH $\sim$ 12,[305] making it an excellent insoluble surfactant to contrast with PFOA. IRRAS spectra of an AA monolayer on water and on 0.47 M NaCl at pH 12.5 were collected at constant mean molecular area, and a plot of the C–H vibrational modes is shown in Fig. 4.7a. To prevent trace metal binding to the AA monolayer, 4 μM ethylenediaminetetraacetic acid (EDTA) was added to both subphase solutions.[306]

Mean molecular area (MMA) values were chosen based on the surface pressure-area isotherms in Fig. 4.7b. At 55.5 Å^2/molecule, the AA monolayer is in a liquid expanded (LE) phase in which the surfactants are fluid and not yet aggregated. Monolayer compression yields a plateau region (37 Å^2/molecule) corresponding to a

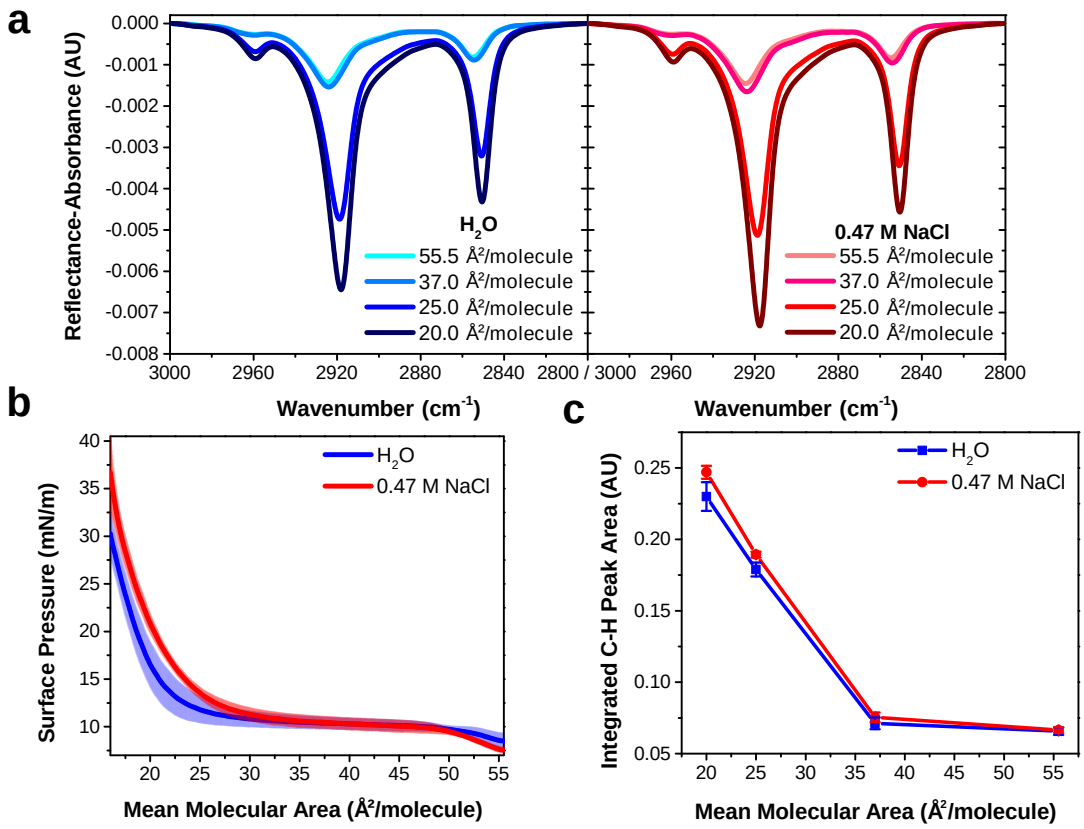

Figure 4.7: Deprotonated arachidic acid (AA) monolayers on water and 0.47 M NaCl at pH 12.5. Both aqueous subphase solutions contain 4 μM ethylenediaminetetraacetic acid. (**a**) Infrared reflection-absorption spectroscopy (IRRAS) of the AA monolayer C–H stretching region as a function of mean molecular area, expressed in units of Å^2/molecule. (**b**) Surface pressure-area isotherms of AA monolayers. Shading represents one standard deviation from the mean. (**c**) Integrated peak area corresponding to C–H vibrational modes as a function of AA monolayer mean molecular area. Lines connecting the data points are drawn to guide the eye, and error bars represent one standard deviation from the mean.

first-order phase transition between the LE and tilted condensed (TC) phases, known as the LE-TC coexistence region.[306,307] AA surfactants aggregate into 2D domains at the air/water interface and increase in size with compression.[308] (Brewster angle microscopy images of the AA domain morphologies are shown in Fig. 4.8.) The monolayer begins to transition to the TC phase starting at 25 Å^2/molecule and the transition is complete by 20 Å^2/molecule, characterized by a condensed sheet of surfactant. The AA monolayer has a higher surface pressure at mean molecular areas $\lesssim$ 35 Å^2/molecule on the NaCl solution subphase, indicating that NaCl expands the

monolayer. The chloride counterion is likely to blame for this monolayer expansion, as it has a greater propensity to partition to the air/water interface than sodium, whereupon it intercalates between the carboxylic acid head groups of AA, amplifying electrostatic repulsion.[65,309]

To affirm the AA monolayer two-dimensional phase assignments and stability at low MMA, Brewster angle microscope (BAM) images of the monolayer were collected throughout the surface pressure-area isotherms. Representative images of the AA monolayer at the MMA values probed spectroscopically are shown in Fig. 4.8 with the H_2O subphase on the top row and the 0.47 M NaCl subphase on the bottom row. Dark regions of the image correspond to the aqueous subphase, and bright regions correspond to domains, or two dimensional aggregates, of the AA surfactants. In the liquid expanded (LE) phase at 55.5 Å^2/molecule, the AA surfactants have not yet aggregated into domains; thus the images are dark on both subphase solutions. Surfactant domains form in the LE - tilted condensed (TC) coexistence region, and the domain shapes differ significantly between the aqueous subphases at 37.0 Å^2/molecule. AA on the H_2O subphase forms vine-like domains, whereas the NaCl solution induces small, asymmetrical AA domains. Further compression to 25.0 Å^2/molecule causes the domains to merge. AA on H_2O forms brighter merged domain structures and larger dark regions than AA on 0.47 M NaCl, suggesting that the surfactants aggregate more closely to one another on H_2O. The trend is still apparent in the TC phase at 20 Å^2/molecule, although the AA domains have largely merged into one sheet. The brighter domain structures and greater dark space within the BAM images of AA on H_2O suggest that AA surfactants aggregate more tightly together, meaning that vibrational excitons between the surfactants are more significant for AA on H_2O than for AA on the NaCl solution subphase.

The three peaks in the IRRAS spectra of AA (Fig. 4.7a) correspond to the υ_{AS}-CH_3 stretch at 2959 cm^{-1}, the υ_{AS}-CH_2 stretch at 2918 cm^{-1}, and the υ_{S}-CH_2 stretch

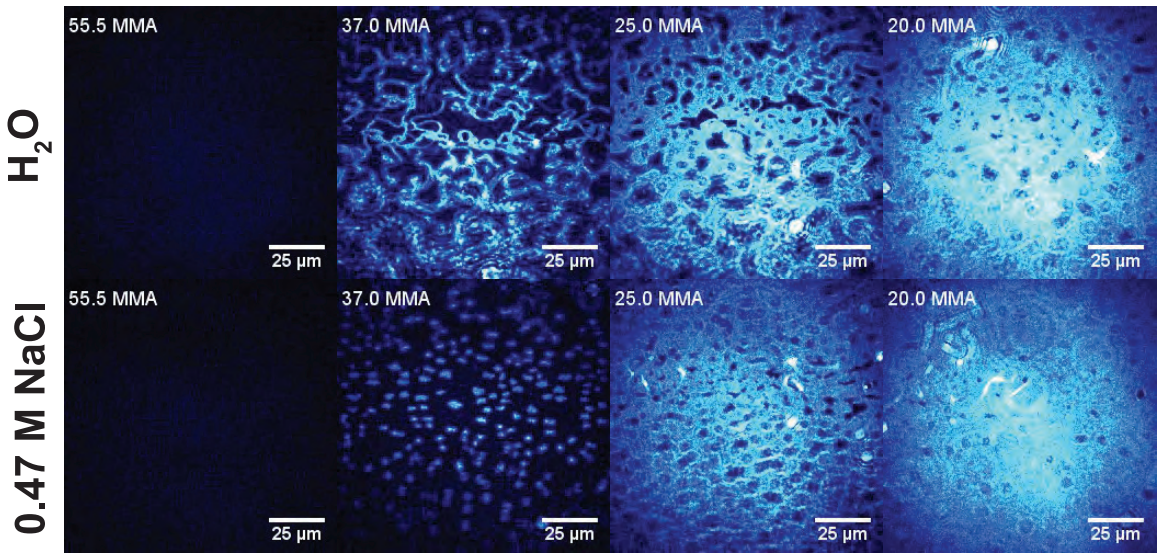

Figure 4.8: Brewster angle microscopy (BAM) images of arachidic acid (AA) monolayers on H_2O (top row) and on 0.47 M NaCl (bottom row). The aqueous subphase solutions were adjusted to pH 12.5, and 4 μM ethylenediaminetetraacetic acid (EDTA) was added to prevent trace metal binding to the AA carboxylate moieties.

at 2850.5 cm^{-1}.[66] A mutual feature of these spectra (regardless of subphase identity) is that the region between the two high-energy bands becomes more intense as a function of monolayer compression. This feature is indicative of delocalization of the vibrational wavefunction across a new region in the vibrational manifold, hinting at exciton splitting. At smaller mean molecular area (25.0 and 20.0 $Å^2$/molecule), the C–H peak intensity is greater on 0.47 M NaCl than on H_2O, as shown in the integrated C–H peak areas in Fig. 4.7d. As the AA monolayer is compressed to smaller mean molecular area, the C–H peak area of AA on the NaCl solution subphase becomes larger relative to the water subphase. AA surfactants are closer together on the water subphase and therefore subject to stronger vibrational couplings, which decay with distance as R^{-3}. As a result, excitonic behavior is observable in insoluble surfactant monolayers via IRRAS signal intensity depletion in the C–H stretching region.

To ensure that differences in AA C–H peak intensities are due to vibrational excitons and not desorption into the aqueous subphase, AA monolayer surface pressure was tracked throughout the IRRAS measurements. The AA surface pressure

relative to the initial surface pressure (SP/SP_0) is plotted as a function of time in Fig. 4.9, and one standard deviation from the mean is represented by shading. At 37.0 $Å^2$/molecule, the AA surface pressure changes minimally throughout an IRRAS measurement, and the magnitude of change is nearly identical between the water and 0.47 M NaCl aqueous subphase solutions. The decrease in surface pressure becomes slightly greater at 25.0 $Å^2$/molecule such that the relative surface pressure drops to 0.94 ± 0.02 and 0.92 ± 0.01 for the H_2O and NaCl subphase solutions, respectively. If the larger decrease in surface pressure on the 0.47 M NaCl subphase was indicative of AA desorption, then the C–H peak intensity would be smaller in magnitude on the NaCl solution subphase in comparison to the water subphase. However, the opposite is true in that the C–H peak intensity is greater for AA on the NaCl solution subphase, indicating that the peak intensity differences between the aqueous subphase solutions can be attributed to vibrational excitons and not AA desorption. The relative surface pressure measurements for AA at 20.0 $Å^2$/molecule also support this conclusion. While the surface pressure decrease is the largest in magnitude at this particular MMA, the differences in relative surface pressure are insignificant between the two aqueous subphase solutions (0.75 ± 0.06 on H_2O versus 0.76 ± 0.03 on 0.47 M NaCl).

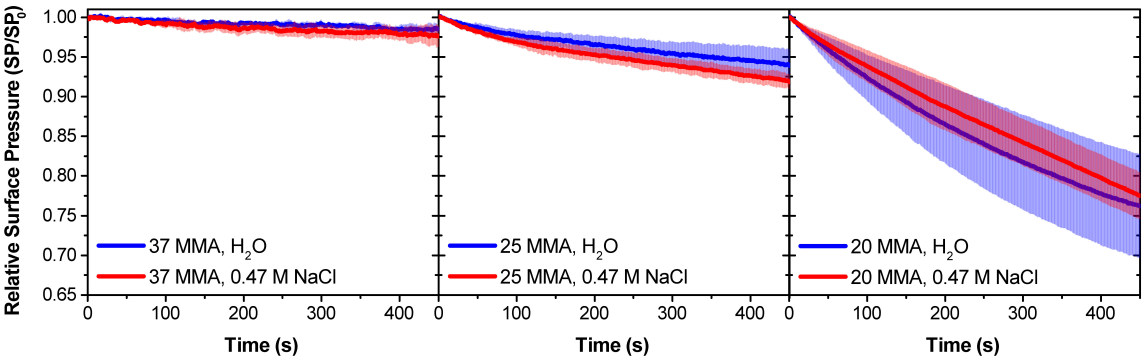

Figure 4.9: Surface pressure stability of arachidic acid (AA) monolayers on H_2O and 0.47 M NaCl aqueous subphase solutions throughout the time span of an infrared reflection-absorption spectroscopy (IRRAS) experiment. The subphase pH was adjusted to pH 12.5, and 4 μM ethylenediaminetetraacetic acid (EDTA) was added to prevent trace metal binding to the AA carboxylate moieties. Shading represents one standard deviation from the mean.

The observable impact of vibrational excitons on the IRRAS spectra of AA monolayers is smaller in magnitude than that of PFOA. Our calculations imply that, on average, transition dipole moments of C–F moieties are 3× larger than those of C–H moieties in fatty acids of commensurate chain length, contributing to the observed differences in vibrational coupling. Soluble surfactants are able to access an extra degree of freedom (in comparison to insoluble surfactants that are restricted to the interfacial plane), which could also influence the vibrational mode coupling by allowing for three-dimensional aggregation.

4.4 Conclusions

We observed the signature of vibrational excitons in surfactants at the air/water interface via alkyl and fluoroalkyl vibrational mode signal reduction in 1D surface-sensitive infrared reflection-absorption spectroscopy (IRRAS). Surface tensiometry, molecular dynamics simulations, and *ab initio* calculations confirm the existence of significant vibrational coupling in both soluble fluoroalkyl and insoluble alkyl surfactants. Intentionally excluding solvent effects from the theoretical model reveals that coupling with the solvent is unimportant in obtaining the most pertinent features of the IRRAS spectrum. Instead, model IRRAS spectra of perfluorooctanoic acid obtained from molecular dynamics simulations and vibrational exciton calculations agree nearly quantitatively with experiment, despite exclusion of solvent effects, indicating that surfactant intermolecular coupling dominates the observed spectral features. While solvent effects are minimal, the ionic composition of the aqueous phase plays a significant role in modulating vibrational coupling via the strong R^{-3} distance dependence of transition-dipole interactions. Salts modulate intermolecular distances (and therefore vibrational couplings) between surfactants, depleting infrared intensity of 1D surface-sensitive spectra. In light of this new interpretation, 1D vi-

brational spectroscopic studies of surfactants at surfaces of varying aqueous phase compositions should be carefully scrutinized.

The results described above present both challenges and opportunities for the surface science community. Quantitative analyses involving vibrational mode peak intensities must be approached with caution to avoid misinterpretation of vibrational spectra due to vibrational coupling. The molecular environment has a profound impact on the organization of self-aggregating molecules, making fluid interfaces particularly susceptible to the influence of vibrational excitons. The emergence of vibrational excitons in 1D spectra offers a new, highly-sensitive spectroscopic handle for probing molecular organization at interfaces. Further study of the spectral perturbations induced by vibrational excitons is needed for the development of improved 1D surface-sensitive vibrational spectroscopic analyses. More broadly, the influence of vibrational excitons should be investigated in systems beyond the air/water interface, particularly in confined environments like aerosols.

Chapter 5

Calcium Bridging Drives Polysaccharide Co-Adsorption to a Proxy Sea Surface Microlayer

5.1 Introduction

Saccharides constitute one of the most abundant classes of organic carbon in sea spray aerosol (SSA);[79,80,227] but the mechanisms through which these compounds are selectively transferred from bulk seawater to the ocean surface, known as the sea surface microlayer (SSML), and finally to SSA, are not fully understood.[83] Compared with seawater concentrations, saccharides are enriched 1.2 – 12.1-fold in the SSML,[78,310,311] 38 – 3700-fold in super-micron SSA,[312] and 100 – 930,000-fold in sub-micron SSA.[32,312] It is thought that soluble saccharides co-adsorb to insoluble organic films at the SSML and transfer into SSA via bubble bursting at the ocean surface.[38,39,313–315] Chemical composition is a significant driver of SSA particle radiative properties, so climate models require predictive representations of marine aerosol composition to accurately model climate processes in the marine boundary layer.[5,30,37,38,47] SSA containing polysaccharides, especially polysaccharides within marine microgels, comprise a significant fraction of cloud condensation nuclei (CCN)[10,316–318] and ice nucleating

particles (INPs),[17,204,319–324] thereby affecting cloud formation and albedo. Thus, characterization of polysaccharide enrichment mechanisms in SSA is imperative for improving aerosol representation in global climate models.

Recent work by Hasenecz *et al.* has shown that the polysaccharide alginate is enriched in laboratory-generated marine aerosol, and alginate enrichment can be enhanced upon adding protein and additional $CaCl_2$ salt to the model seawater solution.[325] Alginate is a type of exopolymeric substance derived from marine brown algae and bacteria;[326,327] it is composed of (1→4)-linked α-L-guluronic (G) and β-D-mannuronic (M) monomers that form a block copolymer with random sequences of M-, G-, and MG-blocks.[328–333] Alginate polymers undergo ionic cross-linking to form hydrophilic gels via metal ion coordination primarily to the G residue carboxylic acid moieties.[330,333,334] The rigidity and stability of the hydrogels are largely driven by the M/G residue ratio and the molecular weight of the polymers,[333,335,336] but the ionic cross-linker identities and concentrations also play a crucial role.[337–342] Multivalent cations readily induce gelation, and the cation solvation free energies dictate the local interaction configurations with G residues.[342] Of the abundant seawater cations, Ca^{2+} is the most efficient gelling agent.[337,338,342] Mg^{2+} only induces gelation at high alginate concentrations ($>$ 3 wt% alginate and $[Mg^{2+}] > 50$ mM) because of its high affinity for water such that the G residue carboxylate moieties cannot readily dehydrate Mg^{2+} for coordination.[339–342] Extensive experimental and computational studies[70,72,73,75,343,344] have investigated polysaccharide aggregation into surface-active marine gels via ionic coordination, but less is known about polysaccharide complexation to other surface-active organic molecules derived from marine biota. Enhanced saccharide enrichment in laboratory-generated SSA in the presence of divalent cations and other surface-active organic material strongly suggests a co-adsorption mechanism mediated by divalent cationic bridging.[39,325]

A divalent cation mediated co-adsorption mechanism was also postulated by Schill

et al. to explain enrichment of the monosaccharide glucuronic acid in laboratory-generated SSA.[39] Glucuronic acid likely co-adsorbs to an insoluble palmitic acid (hexadecanoic acid, $CH_3(CH_2)_{14}COOH$) monolayer via seawater divalent cation bridging interactions. Palmitic acid is one of the most abundant lipids in the SSML[52,53] and in nascent SSA,[49,50,53] making it a good model for insoluble organic matter in an SSML proxy film.[27,67,68,252] Cooperative adsorption (co-adsorption) to insoluble lipid monolayers has been indirectly observed for other saccharides and polysaccharides as well.[38,313,314,345] Electrostatic interactions between charged saccharides and either charged or zwitterionic lipid headgroups have been the predominant mode of co-adsorption proposed. For example, the cationic polysaccharide chitosan primarily interacts with negatively charged and zwitterionic phospholipids through electrostatic interactions between the chitosan ammonium and phospholipid phosphate moieties.[346–351] Chitosan co-adsorption expands the monolayer,[352] and chitosan likely intercalates into the monolayer at low monolayer mean molecular area through dispersion interactions.[350,351] Divalent cationic bridging between the anionic polysaccharide dextran sulfate and the zwitterionic phospholipids 1,2-dipalmitoyl-phosphatidylethanolamine (DPPE) and 1,2-dimyristoyl-*sn*-glycero-3-phosphocholine (DMPC) has also been observed.[353–355] Ca^{2+} bridges the sulfate and phosphate moieties, whereas Na^+ does not.[354] Strength of dextran sulfate co-adsorption increases with the number of calcium bridges formed, and unlike chitosan, dextran sulfate does not intercalate into the monolayer; instead, the authors argued that strong bridging interactions tether the polysaccharide to the underside of the phosphate headgroups.[355] Thus, divalent cationic bridging interactions could promote saccharide co-adsorption to the SSML and enrichment in SSA.

In this study, we examine the cationic bridging mechanism responsible for alginate co-adsorption to a deprotonated palmitic acid monolayer using surface-sensitive infrared reflection-absorption spectroscopy (IRRAS), surface tensiometry, and har-

monic vibrational frequency calculations. To the best of our knowledge, we present the first observations of polyelectrolyte adsorption to an insoluble monolayer of the same charge state bridged by an ion of opposite charge. Ca^{2+} induces the greatest degree of alginate co-adsorption to the monolayer, but the divalent cationic bridges break apart upon monolayer protonation. Mg^{2+} also promotes co-adsorption to the deprotonated monolayer, but the interaction is much weaker due to the strong hydration of Mg^{2+}. Na^{+} alone does not facilitate alginate co-adsorption. Our detailed analysis of the alginate co-adsorption mechanism to an SSML proxy film suggest that the Ca^{2+} bridge to surface-active marine organic matter is an important driver of polysaccharide enrichment in the SSML, and thus, in SSA.

5.2 Materials & Methods

5.2.1 Materials

Calcium chloride dihydrate (Certified ACS, Fisher Chemical), magnesium chloride hexahydrate (Crystalline/Certified ACS, Fisher Chemical), d_{31}-palmitic acid (98%, Cambridge Isotope Laboratories, Inc.), and d_{33}-cetyl alcohol (d_{33}-hexadecanol, 98%, Cambridge Isotope Laboratories, Inc.) were used as received. Sodium chloride (99.5%, for biochemistry, ACROS Organics™) was baked for at least 10 hours in a furnace at 650° C to remove residual organic impurities.[251,284] Alginic acid (sodium salt, ACROS Organics™, Lot: A0406891) was also used as received from the same batch to maximize homogeneity in molecular weight and composition. All aqueous solutions were prepared with ultrapure water (18.2 MΩ·cm, Milli-Q Advantage A10, EMD Millipore) in glassware cleaned in a piranha acid bath. Acidification by atmospheric CO_2 causes the ultrapure water pH to be 5.8 ± 0.1; hence, the pH 5.8 aqueous solutions were not pH adjusted. Atmospheric CO_2 acidifies the solutions at seawater pH too, so the solutions were initially pH adjusted with sodium hydroxide

pellets (98%, extra pure, ACROS Organics™) to 8.6 ± 0.1 to ensure that the pH would be 8.2 ± 0.1 throughout spectral acquisition. Lipids were dissolved in chloroform (Reagent ACS, 99.8+%, ACROS Organics™) to prepare ∼1.25 mM solutions for spreading onto the aqueous surface.

5.2.2 Surface Tensiometry

Surface pressure – area isotherms were performed using the Wilhelmy plate method in a Teflon Langmuir trough with Delrin barriers (Biolin Scientific). The platinum Wilhelmy plate, trough, and barriers were cleaned thoroughly with ultrapure water and ethanol, and the Wilhelmy plate was fired with a Bunsen burner until red hot. Surface cleanliness of the aqueous subphase was assessed by sweeping the barriers at maximum compression speed (270 mm/min/barrier) to ensure that the surface pressure did not rise above 0.20 mN/m. d_{31}-Palmitic acid dissolved in chloroform was spread dropwise onto the aqueous surface using a glass syringe (Hamilton), and the chloroform solvent was allowed to evaporate over 10 minutes. The barriers were symmetrically compressed at a rate of 5 mm/min/barrier, and constant surface pressure was maintained during spectroscopic measurements via slow barrier position fluctuations (1 mm/min/barrier).

5.2.3 Infrared Reflection-Absorption Spectroscopy

Infrared-reflection absorption spectroscopy was conducted using a custom-built optical setup. Two planar gold mirrors positioned at 48° relative to surface normal were placed inside a Fourier transform infrared spectrometer (Spectrum 100, PerkinElmer) to direct the incident beam towards the aqueous surface and to direct the reflected light towards the liquid nitrogen-cooled HgCdTe (MCT) detector. Spectra were collected with unpolarized light as an average of 400 scans in the single-beam mode, and the spectral resolution was set to 4 cm^{-1}. Energy values were recorded be-

tween 450 and 4000 cm^{-1} in 0.5 cm^{-1} increments. Experiments were repeated in at least triplicate, and each spectrum was reported as the average of all trials. Spectral background subtraction and peak integration were performed using OriginPro 9.0. The O-H stretching region was analyzed by fitting a line between endpoints 2985 and 3000 cm^{-1} for baseline subtraction, and the area under the curve was integrated between these endpoints. The IRRAS spectra and integrated peak areas were numerically corrected to account for differences in monolayer mean molecular area (MMA) between experiments. The average MMA value of the subphase containing alginate was divided by the corresponding average MMA value of the salt water subphase. This ratio was then multiplied into the reflectance-absorbance values of the spectra containing alginate. Similar spectral analyses were performed in the COOH stretching (1150-1850 cm^{-1}) and CD_2 scissoring mode (1070-1110 cm^{-1}) regions, and descriptions of the peak fitting procedures can be found in Appendix B. All spectra and data points represent averages of at least three measurements, and error bars represent one standard deviation from the mean.

5.3 Results & Discussion

The mechanism of alginate co-adsorption to a d_{31}-palmitic acid ($CD_3(CD_2)_{14}COOH$) monolayer was investigated as a function of solution ionic composition, d_{31}-palmitic acid protonation state, and surface pressure. We will use the terms "monolayer" to refer to the monomolecular layer of d_{31}-palmitic acid alone and "film" to describe alginate complexed to the d_{31}-palmitic acid monolayer. Deuterated palmitic acid was used to spectrally isolate the CD_2 scissoring mode from the carboxylate stretching region. The ionic composition was selected to model concentrations of the most abundant cations in seawater: 0.47 M NaCl, 10 mM $CaCl_2$, and 53 mM $MgCl_2$.[1,254] As a direct comparison to the 10 mM $CaCl_2$ solution, alginate co-adsorption in 10 mM

$MgCl_2$ aqueous solution was also measured. All aqueous solutions have a background of 0.47 M NaCl to maintain high ionic strength as in seawater.

The carboxylic acid protonation state was varied through the solution pH values of 8.2 and 5.8. Palmitic acid has a reported surface pKa between 8.34 and 8.7,[67,241,356,357] and the pKa values of alginate G and M residues are 3.7 and 3.4, respectively.[358] Thus at pH 8.2, the pH of seawater,[359] palmitic acid is partially deprotonated and alginate is fully deprotonated. At pH 5.8, palmitic acid is mostly protonated, and alginate carboxylate groups remain deprotonated. Salts can deprotonate carboxylic acids at pH values significantly below the pKa,[68,179,360] however, so a d_{33}-cetyl alcohol (d_{33}-hexadecanol, $(CH_3(CH_2)_{15}OH)$ monolayer was used as a control to study alginate co-adsorption to a fully protonated monolayer. Alginic acid is insoluble in water, so a lower pH value was not tested instead to avoid significant changes in solubility. Alginate hydrolysis kinetics are also enhanced in acidic solution, thereby changing the alginate molecular weight distribution in solution over time.[361,362] Deprotonated palmitate molecules are slightly more soluble in water,[68,242] so IRRAS spectra were maintained and collected at constant surface pressure to minimize any interpretation impacts from dissolution. The surface pressure values of 5 mN/m and 25 mN/m were chosen to represent the tilted condensed (TC) and untilted condensed (UC) two-dimensional monolayer phases, respectively.[97] Both phases exhibit long-range lateral order in the alkyl tails, but the d_{31}-palmitic acid molecules in the UC phase are closer together on average (more tightly packed) and less tilted relative to surface normal.[87]

To measure co-adsorption of alginate to the d_{31}-palmitic acid monolayer, IRRAS spectra were analyzed in the OH-stretching region (2985-3800 cm^{-1}), the COOH stretching region (1150-1850 cm^{-1}), and the CD_2 scissoring mode region (1070-1110 cm^{-1}). IRRAS spectra are plotted as reflectance-absorbance (RA),

$$\mathrm{RA} = -\log\left(\frac{R_\mathrm{f}}{R_0}\right) \quad , \tag{5.1}$$

where R_f corresponds to the film reflectance and R_0 corresponds to the reflectance of the bare aqueous solution. Hence, the signal from the interfacial film is captured, whereas the signal from the bulk aqueous phase is subtracted. When the film reflectance is greater than the solution reflectance ($R_f/R_0 > 1$), the reflectance-absorbance values are negative. Conversely, if the reflected signal from the solution is greater than that of the film ($R_f/R_0 < 1$), then the reflectance-absorbance values are positive. To isolate the signal from alginate co-adsorption due to the presence of the d_{31}-palmitic acid monolayer, alginate was also included in the aqueous solution spectrum (R_0). Yet, the contribution of alginate adsorbed to the air-water interface due to surface activity alone is small and below our spectroscopic limit of detection.

The OH stretching region provides sensitive detection of the aqueous solution reflectance, making the spectra useful for quantifying changes in interfacial coverage as a function of alginate co-adsorption. As shown in Figs. 5.1a and 5.1c, the IRRAS OH-stretching modes are positive in sign, indicating that the OH region reflectance decreases upon spreading d_{31}-palmitic acid onto the aqueous solution. The magnitude of the reflectance-absorbance signal intensity also increases with compression of the monolayer to higher surface pressure. Thus, increasing organic surface coverage decreases reflectance from the underlying aqueous solution. Consequently, alginate co-adsorption to d_{31}-palmitic acid molecules increases surface coverage, and the OH stretching region reflectance-absorbance values increase with alginate co-adsorption to the film. If there is no alginate co-adsorption, then the film spectrum with alginate in the solution directly overlaps the monolayer spectrum without alginate.

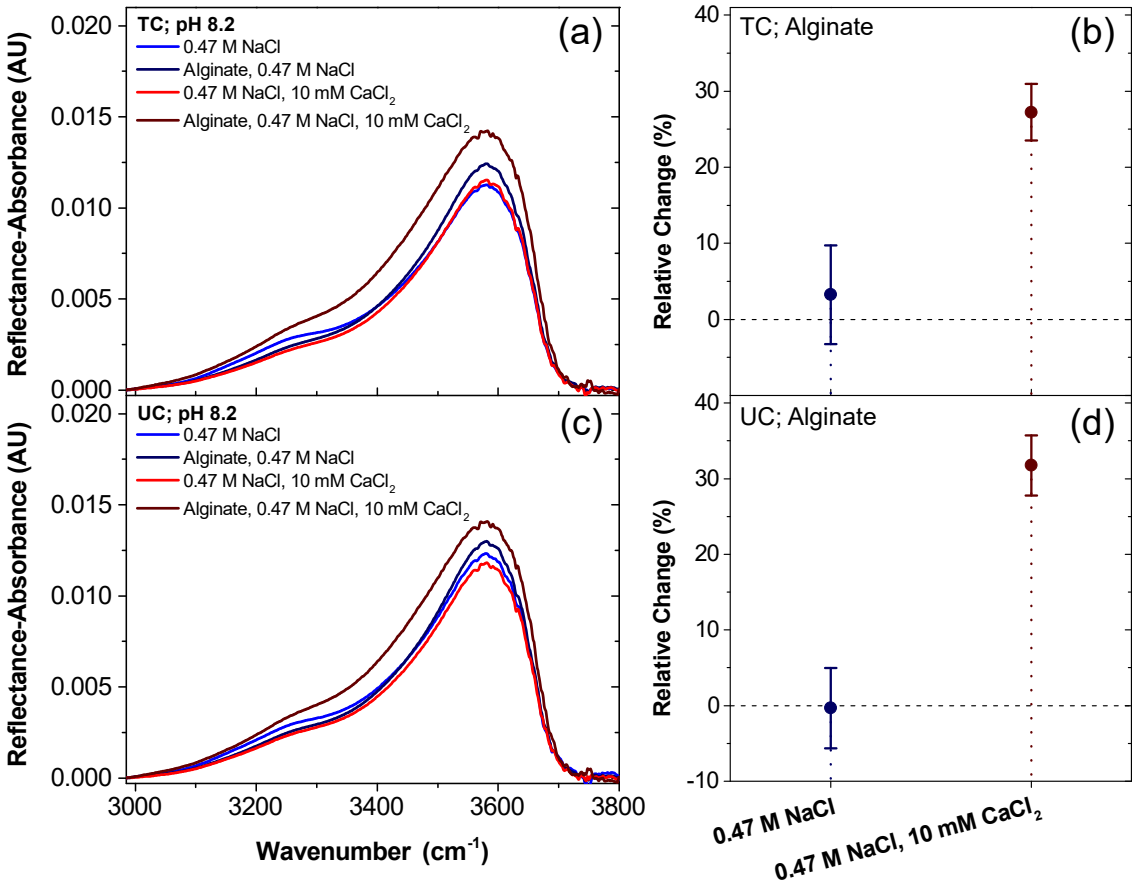

Figure 5.1: IRRAS spectra of the OH stretching region and the corresponding relative changes in integrated peak area of the film indicate that $CaCl_2$ induces significant alginate co-adsorption to the d_{31}-palmitic acid monolayer. Data points and error bars are color-coded to indicate differences in solution composition. Surface pressure was held constant in the **(a)** tilted condensed (5 mN/m) and **(c)** untilted condensed (25 mN/m) phases throughout spectral acquisition. The relative changes in integrated peak area between the solutions with and without alginate are quantified in the **(b)** tilted condensed and **(d)** untilted condensed phases. Positive relative change indicates alginate co-adsorption to the monolayer, and 0% relative change indicates no co-adsorption.

Figs. 5.1a and 5.1c illustrate changes in the OH stretching region spectra caused by increasing organic surface coverage due to alginate co-adsorption. The spectrum of d_{31}-palmitic acid spread onto an aqueous solution containing 50 ppm alginate, 0.47 M NaCl, and 10 mM $CaCl_2$ is significantly enhanced relative to d_{31}-palmitic acid spread onto the salt water solution. IRRAS signal corresponding to the NaCl and alginate solution is slightly greater relative to the NaCl solution alone, but the differences are much smaller in the absence of $CaCl_2$. The IRRAS film spectrum corresponding to

alginate co-adsorption closely follows the shape of the monolayer spectrum on salt water solution, and the greatest OH stretching region signal enhancement occurs around ~3580 cm^{-1} which has been assigned to surface water molecules hydrogen bonded to a carboxylic acid group.[356,363,364] Therefore, alginate co-adsorption enhances the signal around 3580 cm^{-1} due to the alginate carboxylate hydration.

To better quantify organic surface coverage as a function of alginate co-adsorption, the MMA-corrected OH region was integrated between 2985 and 3800 cm^{-1}. The relative change in the integrated peak areas between the spectra with and without alginate was calculated using the following formula:

$$\text{Relative Change} = \frac{A_{\text{Alginate}} - A_{\text{SW}}}{A_{\text{SW}}} \times 100\% \ . \tag{5.2}$$

In this equation, A_{Alginate} represents the integrated peak area of the spectrum with alginate in the solution, and A_{SW} represents the integrated peak area of the spectrum containing only salt water (no alginate) in the solution. Alginate co-adsorption corresponds to a positive relative change in surface coverage, and no adsorption results in a 0% relative change. While the 0.47 M NaCl solution might induce some alginate co-adsorption to the TC monolayer, as shown by the small but positive relative change value in Fig. 5.1b, the value is not statistically significant given that the error (represented as one standard deviation from the mean) is larger than the average relative change value. Addition of 10 mM $CaCl_2$ to the solution containing alginate induces a significant increase in the integrated peak area and consequently a 27% relative change in surface coverage. This increase suggests an alginate co-adsorption mechanism of divalent cationic bridging between alginate and d_{31}-palmitic acid carboxylate moieties.

The differences between the TC and UC spectra and associated relative changes in surface coverage provide insights into the co-adsorption mechanism. The UC film

spectrum corresponding to the 50 ppm alginate and 0.47 M NaCl solution nearly overlaps with the UC monolayer spectrum corresponding to the 0.47 M NaCl solution (Fig. 5.1c), suggesting little to no alginate co-adsorption. The average relative difference in integrated peak area of the UC monolayer and film spectra is approximately 0% (Fig. 5.1d), indicating a lack of alginate co-adsorption. Additionally, the smaller relative change in surface coverage in comparison to the TC spectrum suggests that alginate is being "squeezed out" of the compressed film. This hypothesis is further supported by greater MMA expansion with alginate in the solution for the TC film relative to the UC film (see Table B.1). It is possible that alginate intercalates into the TC film via weaker electrostatic interactions induced by Na^+ cations and via hydrogen bonding interactions between palmitic acid headgroups and alginate hydroxyl moieties. However, in the UC phase, alginate is pushed out of the interface due to exchange repulsion. Higher surface pressure increases alginate co-adsorption for the solution containing 10 mM $CaCl_2$ to a 32% relative change in surface coverage, and film expansion in the presence of alginate is not significantly different between the TC and UC phases. Thus, alginate likely does not intercalate between the d_{31}-palmitic acid molecules with $CaCl_2$ in the solution, and the UC film possibly provides more ideally spaced sites for the Ca^{2+} bridges.

Palmitic acid protonation state significantly impacts the extent of alginate co-adsorption. For the d_{31}-palmitic acid monolayer at pH 5.8, there is a reduced degree of alginate co-adsorption to the film in comparison to the chemical system at pH 8.2. The d_{31}-palmitic acid TC and UC spectra corresponding to the solution containing alginate have higher reflectance-absorbance values across the entire OH stretching region (Figs. 5.2a and 5.2c), indicative of alginate co-adsorption. The relative changes in surface coverage presented in Figs. 5.2b and 5.2d quantify this observation, in which alginate co-adsorption at pH 5.8 results in a 14% and 9% increase in the integrated peak area for the TC and UC phase spectra, respectively. At pH 8.2, alginate co-

adsorption results in a 27% and 32% integrated peak area increase for the TC and UC phase spectra, respectively. Therefore, increased d_{31}-palmitic acid protonation decreases the extent of alginate co-adsorption. Unlike the interfacial film at pH 8.2, monolayer compression decreases the magnitude of alginate co-adsorption for the solution at pH 5.8. Alginate might be intercalating into the TC film similarly to the mechanism proposed for the solution containing only 0.47 M NaCl.

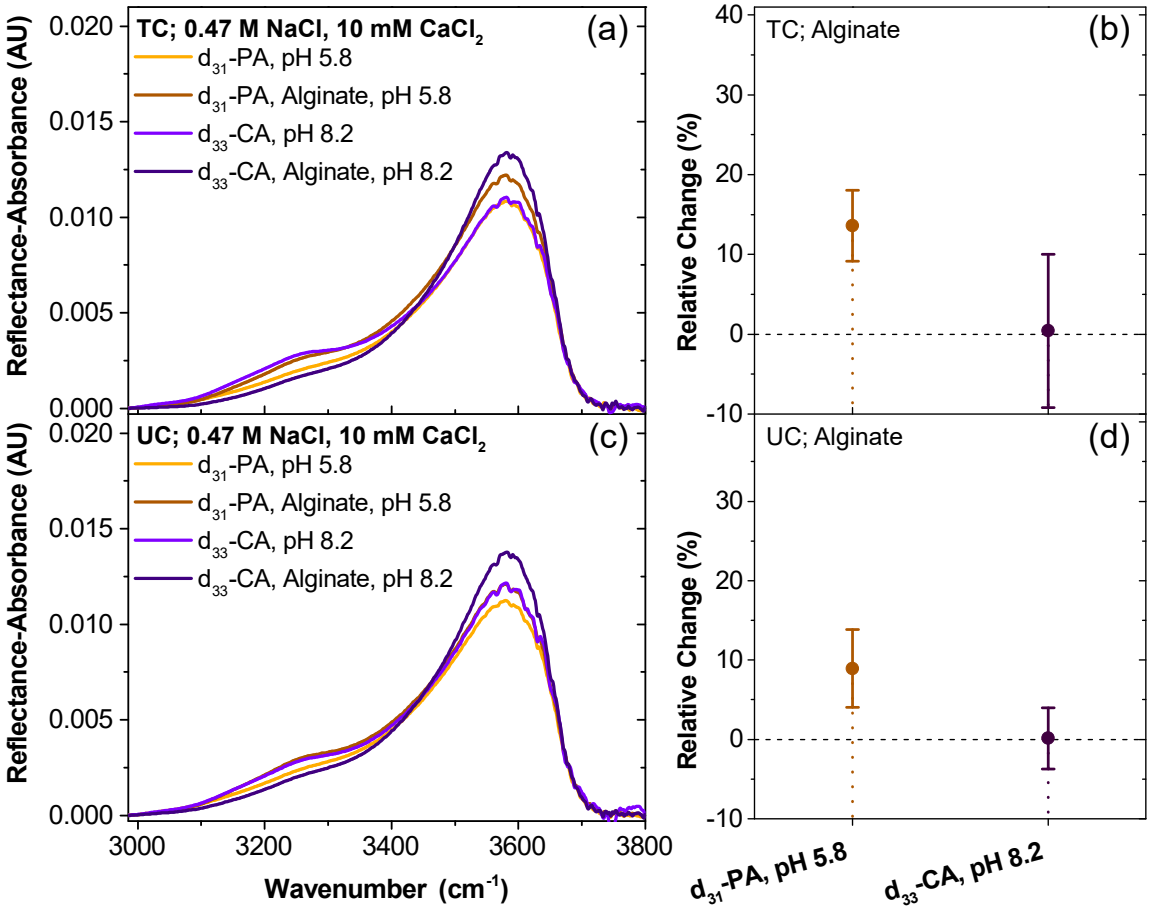

Figure 5.2: IRRAS spectra of the OH stretching region and the corresponding relative changes in integrated peak area of d_{31}-palmitic acid (d_{31}-PA) and d_{33}-cetyl alcohol (d_{33}-CA) monolayers show that headgroup protonation prevents alginate co-adsorption. Data points and error bars are color-coded to indicate differences in monolayer and solution composition. Surface pressure was held constant in the **(a)** tilted condensed (5 mN/m) and **(c)** untilted condensed (25 mN/m) phases throughout spectral acquisition. (Note that the light purple and dark brown data curves overlap in **(c)**.) The relative changes in integrated peak area between the solutions with and without alginate are quantified in the **(b)** tilted condensed and **(d)** untilted condensed phases. Positive relative change indicates alginate co-adsorption to the monolayer, and 0% relative change indicates no co-adsorption.

A fully protonated d_{33}-cetyl alcohol monolayer was examined as a control because it does not become partially deprotonated in the presence of salts at any of the pH values tested. Trends in the IRRAS spectra of d_{33}-cetyl alcohol alone are less clear (Figs. 5.2a and 5.2c). In both monolayer phases, the alginate solution enhances IRRAS signal at ~3580 cm^{-1} and decreases the signal between ~3050 and 3440 cm^{-1} relative to the salt water solution. The region around 3050 cm^{-1} has been attributed to cyclic carboxylic acid dimers observed in polyacrylic acid solutions,[364,365] and the region from ~3200 cm^{-1} to ~3400 cm^{-1} corresponds to a more ordered hydrogen bonding structure to a less-ordered water structure.[363,366,367] Further analysis reveals no significant differences between the OH region integrated peak areas for the solutions with and without alginate in both the TC and UC phases, resulting in a 0% relative change in surface coverage (Figs. 5.2b and 5.2d). It is likely that alginate perturbs the interfacial hydration structure but does not co-adsorb to the cetyl alcohol monolayer. Thus, a protonated monolayer blocks alginate co-adsorption, indicating the importance of electrostatic interactions in polysaccharide co-adsorption to an SSML proxy film.

The carboxylic acid spectral region (1150-1850 cm^{-1}) provides further insight into the d_{31}-palmitic acid protonation state and the extent of alginate co-adsorption. Harmonic vibrational frequency calculations were performed to predict the relative frequency shifts between the d_{31}-palmitic acid carboxylate and carboxylic acid modes and the alginate carboxylate modes (see Appendix Section B.2). Additionally, peaks were fitted to Gaussian functions to resolve the center wavelengths and full width at half maximum (FWHM) values; the fitting procedure and summary of the Gaussian fits for each spectrum are summarized in Appendix Section B.3. Spectra of a d_{31}-palmitic acid TC (Fig. 5.3a) and UC (Fig. 5.3c) monolayer exhibit four negative peaks corresponding to the lipid carboxylic acid moieties and one positive band at ~1660 cm^{-1} corresponding to the water bending mode (δ H-O-H). The proto-

nated carboxylic acid moiety is characterized by the C-OH stretching mode (ν C-OH, $\sim$1270 cm^{-1}) and the C=O stretching mode (ν C=O, $\sim$1720 cm^{-1}). Deprotonation of the carboxylic acid leads to the appearance of the COO^- symmetric (ν_S COO^-, $\sim$1410 cm^{-1}) and asymmetric (ν_{AS} COO^-, $\sim$1540 cm^{-1}) stretching modes (negative bands).

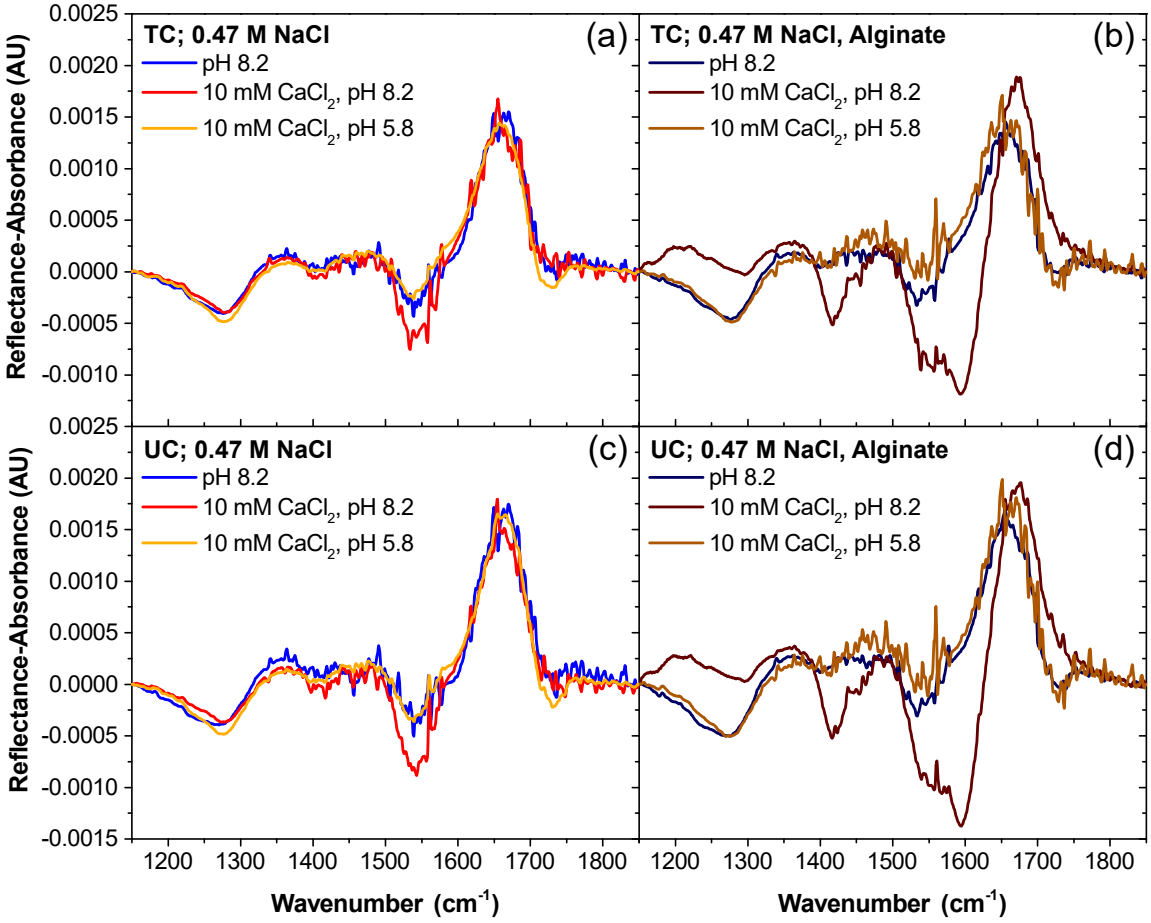

Figure 5.3: IRRAS spectra of the COOH stretching region provide direct evidence of alginate co-adsorption via Ca^{2+} bridging interactions to the d_{31}-palmitic acid monolayer at pH 8.2. Spectral lines are color-coded to indicate differences in solution composition. Surface pressure was held constant in the **(a)**, **(b)** tilted condensed (5 mN/m) and **(c)**, **(d)** untilted condensed (25 mN/m) phases throughout spectral acquisition. Spectra corresponding to the salt water solutions are shown in **(a)** and **(c)**, and spectra corresponding to the salt water solutions containing 50 ppm alginate are shown in **(b)** and **(d)**.

As anticipated, d_{31}-palmitic acid spread onto a 0.47 M NaCl solution at pH 8.2 is partially deprotonated, demonstrated by the presence of all four carboxylic acid

and carboxylate stretching modes (Figs. 5.3a and 5.3c). Addition of 10 mM CaCl2 further deprotonates the headgroups, as shown by the increase in COO^- stretching intensities and by the disappearance of the C=O stretching mode in both TC and UC phases (Tables B.6 and B.8). Decreasing the pH to 5.8 increases the extent of d_{31}-palmitic acid protonation; the C-OH and C=O stretching modes are most intense at this pH (Table B.10). However, the presence of the COO^- stretching modes in the TC and UC phase spectra indicates that Ca^{2+} induces some deprotonation which has been shown previously.[68,176,368,369]

Direct measurement of alginate co-adsorption to the d_{31}-palmitic acid monolayer is observed in Figs. 5.3b and 5.3d. There is a large increase in the negative COO^- stretching peak intensities and breadth for d_{31}-palmitic acid spread onto the 0.47 M NaCl, 10 mM $CaCl_2$, and 50 ppm alginate solution at pH 8.2. The asymmetric and symmetric stretches appear to split into higher and lower frequency bands, so an additional Gaussian function was used to fit both peaks (Fig. B.5). Vibrational frequency calculations predict a 47 cm^{-1} blue shift and a 20 cm^{-1} blue shift for the alginate asymmetric and symmetric COO^- stretching modes, respectively, relative to the corresponding d_{31}-palmitic acid modes (Tables B.3 and B.5). The theoretical predictions quite closely match the experimental ~55 cm^{-1} blue shift for the second ν_{AS} COO^- peak and the ~37 cm^{-1} blue shift for the second ν_S COO^- peak (Table B.9). Hence, the higher frequency COO^- stretching bands indicate alginate co-adsorption to the largely deprotonated monolayer in the presence of $CaCl_2$.

The carboxylate region also provides evidence for Ca^{2+} ionic bridges driving alginate co-adsorption to the d_{31}-palmitic acid monolayer. Alginate co-adsorption induces d_{31}-palmitic acid deprotonation, as shown by increased COO^- stretching intensities and decreased C-OH stretching intensity for the pH 8.2 solution containing 10 mM CaCl2 (Fig. 5.3). Similar peak broadening and intensity enhancement was observed for the phosphate headgroup vibrational modes of 1,2-dipalmitoyl-*sn*-glycero-

3-phosphatidic acid (DPPA) upon arginine and guanidinium binding.[192] Palmitic acid deprotonation likely facilitates the formation of energetically favorable ionic complexes between alginate, Ca^{2+}, and palmitate. Furthermore, the ν_{AS} COO^-, ν_S COO^-, and ν C-OH modes blue shift upon addition of alginate to the solution (Table B.9). The ν_{AS} COO^- mode blue shifts ~2.5 cm^{-1} in the TC phase but does not shift in the UC phase, the ν_S COO^- mode blue shifts 7 cm^{-1} in the TC phase and ~6 cm^{-1} in the UC phase, and the ν C-OH mode blue shifts ~13 cm^{-1} in the TC phase and ~15 cm^{-1} in the UC phase. It is possible that the alginate carboxylate interacting with the Ca^{2+} ion complexed to the d_{31}-palmitate headgroup weakens ionic interactions between the monolayer carboxylate and the Ca^{2+} ion alone, thereby leading to an increased palmitic acid COO^- force constant and blue shifts in the palmitate carboxylate vibrational modes.

Spectra of d_{31}-palmitic acid spread onto the 0.47 M NaCl solution at pH 8.2 and the 0.47 M NaCl and 10 mM $CaCl_2$ solution at pH 5.8 do not exhibit any higher frequency COO^- stretching peaks upon alginate addition to the solution, suggesting minimal to no alginate co-adsorption (Fig. 5.3). Secondly, the ν_{AS} COO^-, ν_S COO-, and ν C-OH mode peak areas are insignificantly different between the solutions with and without alginate, meaning that alginate co-adsorption to the monolayer is unlikely (Tables B.6 and B.7; Tables B.10 and B.11). Smaller blue shifts in the ν_{AS} COO^-, ν_S COO-, and ν C-OH modes are observed for the solutions containing 10 mM $CaCl_2$ and alginate at pH 5.8 as compared to the identical solution at pH 8.2 (Table B.11). While these spectral shifts are not direct evidence of alginate co-adsorption to the monolayer, it is likely that alginate perturbs the d_{31}-palmitic acid headgroup hydration structure via electrostatic interactions with the headgroups. The less numerous d_{31}-palmitate headgroups may facilitate Ca^{2+} bridging interactions with alginate carboxylate moieties at various points across the monolayer, as also indicated by the small relative change in surface coverage (Figs. 5.2b and 5.2d). However, having

fewer Ca^{2+} bridging sites hinders concerted alginate co-adsorption. For the d_{33}-cetyl alcohol monolayer (Fig. B.12), there are no detectable peaks corresponding to alginate carboxylate modes, further supporting the lack of alginate co-adsorption to the fully protonated monolayer.

To determine if alginate co-adsorption perturbs d_{31}-palmitic acid interfacial organization, the CD_2 scissoring mode was analyzed as a function of solution composition, pH, and surface pressure (Fig. 5.4). All conditions yield a CD_2 scissoring mode center wavelength of 1089 cm^{-1} (see Table B.16), indicative of hexagonal lattice packing structure.[154] CD_2 scissoring mode spectra corresponding to the salt water and alginate solutions directly overlap for the 0.47 M NaCl solution at pH 8.2 (Figs. 5.4a and 5.4d) and for the 0.47 M NaCl and 10 mM $CaCl_2$ solution at pH 5.8 (Figs. 5.4c and 5.4f), further indicating no alginate co-adsorption. However, the CD_2 scissoring mode reflectance-absorbance signal magnitude in the TC and UC phase is significantly enhanced for d_{31}-palmitic acid spread onto the 0.47 M NaCl, 10 mM $CaCl_2$, and 50 ppm alginate solutions at pH 8.2 (Figs. 5.4b and 5.4e). Signal enhancement is most apparent in the high frequency regime, and a smaller extent of signal enhancement occurs in the lower frequency region of the spectra. From the harmonic frequency analysis results (Tables B.3-B.5), the signal enhancement can be attributed to alginate C-OH stretching and bending and CH stretching. The CD_2 shoulder features overlap in frequency with the CD_2 scissoring modes, and particularly intense alginate vibrational transitions occur $\sim$10 cm^{-1} lower than and $\sim$20 cm^{-1} higher than the center frequency of the d_{31}-palmitate CD_2 scissoring mode. As a result, the signal enhancement surrounding the CD_2 scissoring peak can be confidently attributed to alginate co-adsorption to the monolayer via Ca^{2+} bridging interactions.

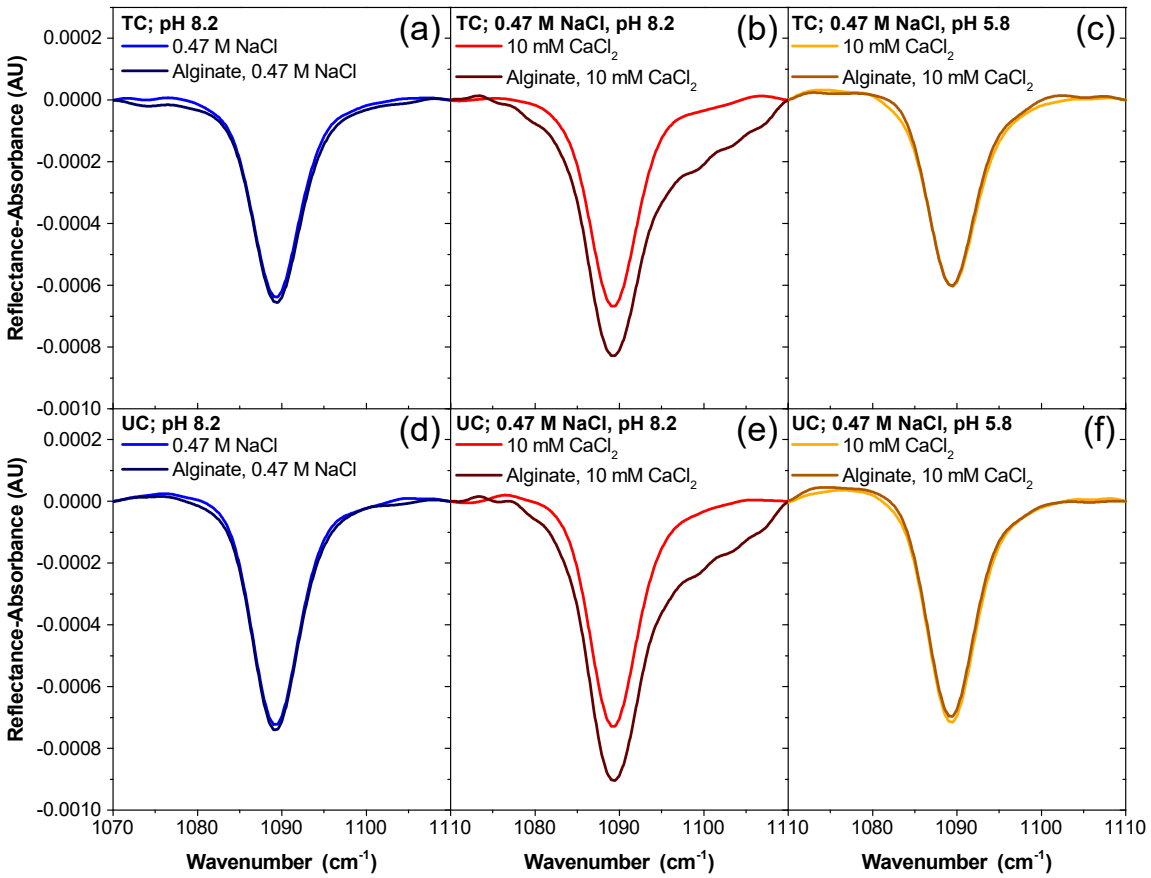

Figure 5.4: IRRAS spectra of the CD_2 scissoring mode region demonstrate alginate co-adsorption to the d_{31}-palmitic acid monolayer in the presence of 10 mM $CaCl_2$ at pH 8.2, and the spectra indicate no changes in d_{31}-palmitic acid lattice packing upon adsorption. Spectral lines are color-coded to indicate differences in solution composition. Surface pressure was held constant in the **(a)**, **(b)**, **(c)** tilted condensed (5 mN/m) and **(d)**, **(e)**, **(f)** untilted condensed (25 mN/m) phases throughout spectral acquisition.

With insights gained into the divalent cationic bridging mechanism, the same alginate co-adsorption experiments were performed with $MgCl_2$, the most abundant divalent cation in seawater (∼53 mM).[1,254] Mg^{2+} has such a strong hydration shell that the fully hydrated Mg^{2+} only weakly interacts with the alginate and palmitic acid carboxylate moieties.[339–342,363,369] Both 10 mM and 53 mM $MgCl_2$ solutions increase IRRAS reflectance-absorbance for the alginate-containing spectra at ∼3580 cm^{-1}, and the magnitude of the signal increase is similar (Figs. 5.5a and 5.5c). Calculation of the relative change reveals that the higher $MgCl_2$ concentration causes a marginal increase in alginate co-adsorbed to the d_{31}-palmitic acid monolayer (Figs. 5.5b and 5.5d). With

increasing $MgCl_2$ concentration, the relative change in integrated peak area increases from 8% to 10% and from 3% to 9% in the TC and UC phases, respectively. The reduction in OH region relative change with film compression (TC to UC phase) further suggests weak binding. The Mg^{2+} bridges are likely weaker than the sum of the other electrostatic, hydrogen bonding, and dispersion interactions between the alginate and d_{31}-palmitic acid molecules, facilitating alginate intercalation into the TC film. Compression of the film then pushes alginate out of the interface, reducing the extent of intermolecular interactions between alginate and d_{31}-palmitic acid in the UC phase. Despite Mg^{2+} being ∼5 times more abundant than Ca^{2+} in seawater, alginate co-adsorption mediated by Mg^{2+} is ∼3 times weaker in comparison to Ca^{2+} when comparing seawater relative concentrations of 10 mM Ca^{2+} and 53 mM Mg^{2+}. At 10 mM concentrations for both cations, calcium outperforms magnesium by a factor of ∼3 in the TC phase and by a factor of ∼10 in the UC phase (Figs. 5.1 and 5.5).

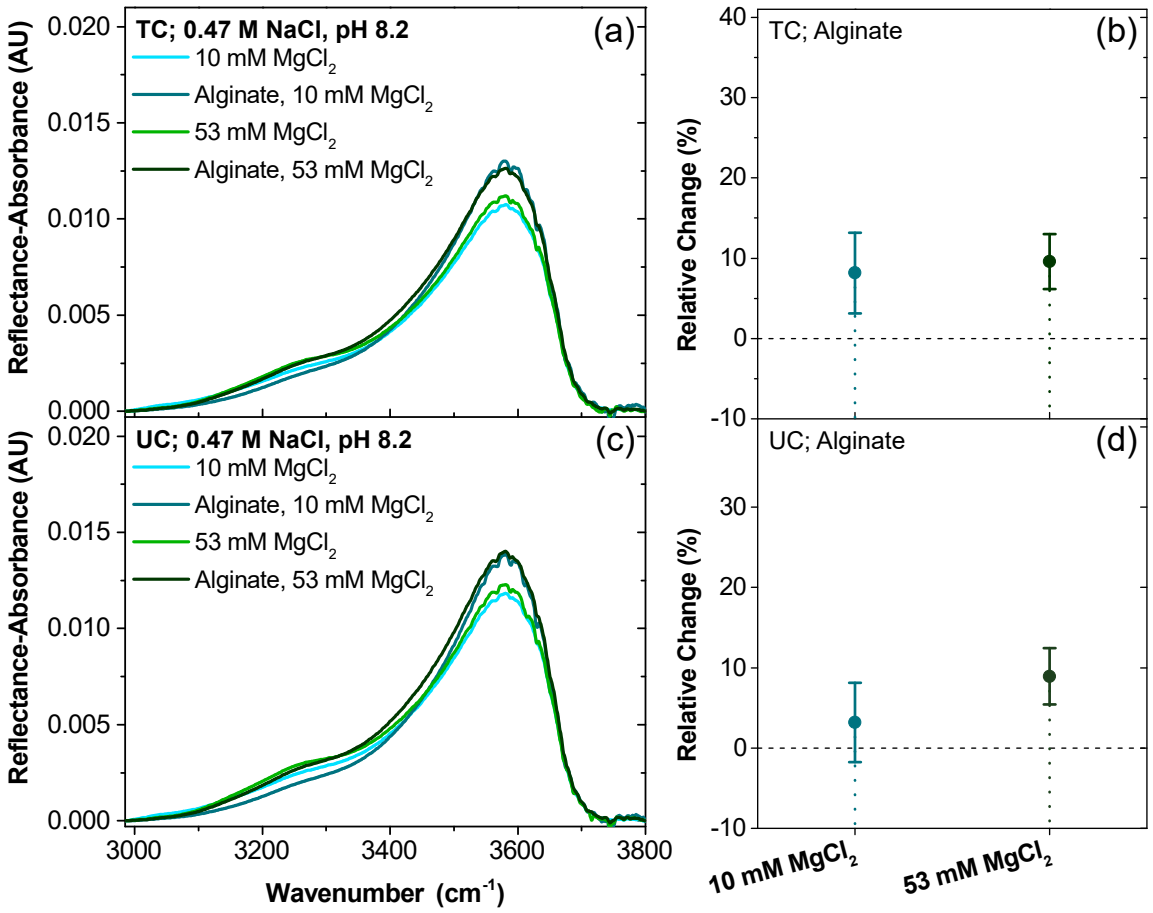

Figure 5.5: IRRAS spectra of the OH stretching region and the corresponding relative changes in integrated peak area indicate that Mg^{2+} induces weak alginate co-adsorption to the d_{31}-palmitic acid monolayer. Data points and error bars are color-coded to indicate differences in solution composition. Surface pressure was held constant in the **(a)** tilted condensed (5 mN/m) and **(c)** untilted condensed (25 mN/m) phases throughout spectral acquisition. The relative changes in integrated peak area between the solutions with and without alginate are quantified in the **(b)** tilted condensed and **(d)** untilted condensed phases. Positive relative change indicates alginate co-adsorption to the monolayer, and 0% relative change indicates no co-adsorption.

The carboxylate region provides additional support for this weak Mg^{2+} bridging co-adsorption mechanism (Fig. 5.6). For d_{31}-palmitic acid spread onto the solution containing 10 mM $MgCl_2$, the ν_S COO^- mode is blue-shifted by 1 cm^{-1} in the TC phase and ~2.5 cm^{-1} in the UC phase, and the ν_{AS} COO^- mode is red-shifted by 1 cm^{-1} in the TC phase and ~3 cm^{-1} in the UC phase (Tables B.8 and B.9). These small spectral shifts suggest that the d_{31}-palmitate carboxylate headgroup becomes

dehydrated with the addition of alginate to the solution,[360] perhaps via complexation of Mg^{2+} to the d_{31}-palmitate carboxylate moiety. The integrated carboxylate peak areas do not change significantly between the salt water solution and alginate solution (Tables B.12 and B.13), suggesting no alginate co-adsorption.

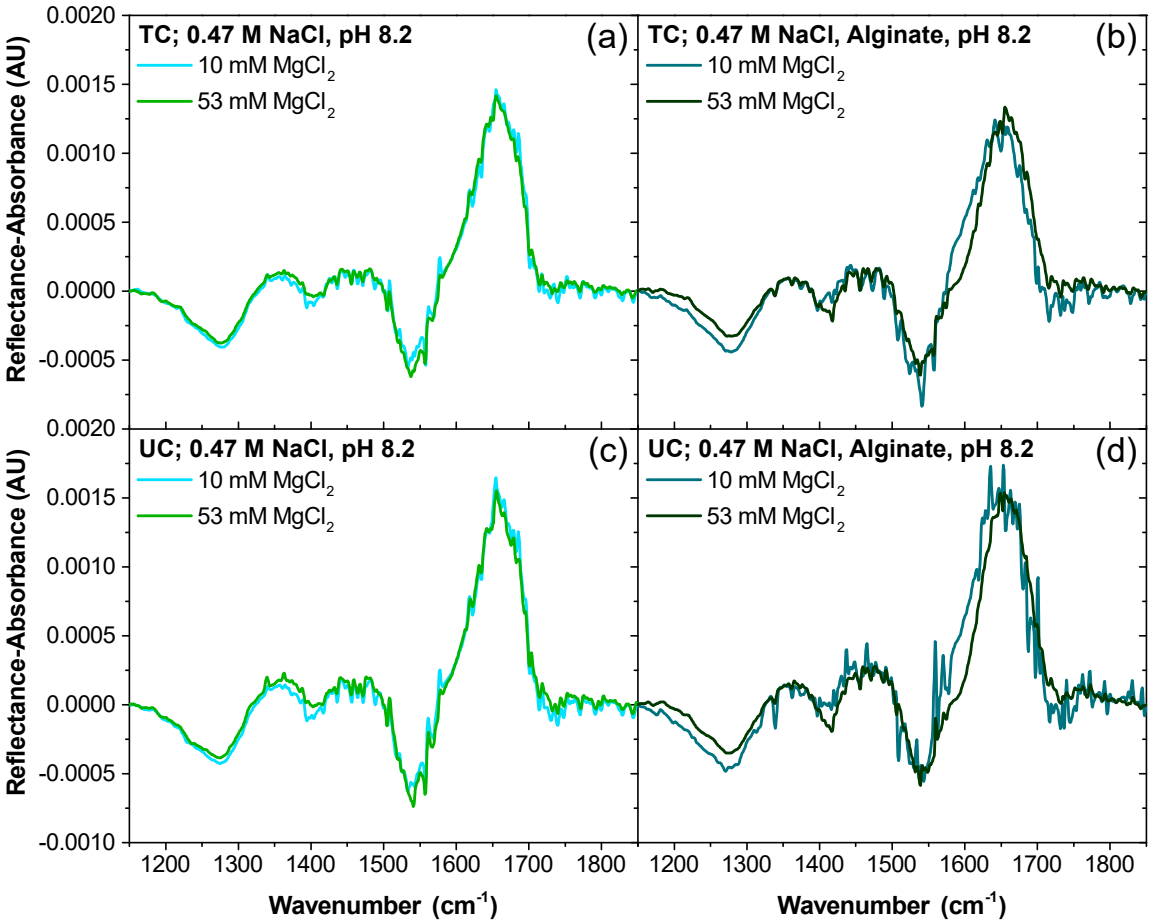

Figure 5.6: IRRAS spectra of the COOH stretching region indicate weak alginate co-adsorption to the d_{31}-palmitic acid monolayer via Mg^{2+} bridging interactions. Spectral lines are color-coded to indicate differences in solution composition. Surface pressure was held constant in the **(a)**, **(b)** tilted condensed (5 mN/m) and **(c)**, **(d)** untilted condensed (25 mN/m) phases throughout spectral acquisition. Spectra corresponding to the salt water solutions are shown in **(a)** and **(c)**, and spectra corresponding to the salt water solutions containing 50 ppm alginate are shown in **(b)** and **(d)**.

Increasing the solution $MgCl_2$ concentration to 53 mM leads to some features of alginate co-adsorption to the monolayer (Fig. 5.6). The d_{31}-palmitic acid ν_{AS} COO^-, ν_S COO^-, and ν C-OH modes blue shift upon alginate addition to the solution (Ta-

bles B.14 and B.15), similarly to the spectra corresponding to the solutions containing 10 mM $CaCl_2$. The ν_{AS} COO^- blue shifts ~0.5 cm^{-1} in the TC phase and ~3 cm^{-1} in the UC phase, the ν_S COO^- blue shifts ~4 cm^{-1} in the TC phase and ~5 cm^{-1} in the UC phase, and the ν C-OH blue shifts ~9 cm^{-1} in the TC phase and ~12 cm^{-1} in the UC phase. The blue shifts are smaller than those observed with the 10 mM $CaCl_2$ solution at pH 8.2, either an indication of fewer Mg^{2+} bridging interactions or weaker bridging interactions. Secondly, the ν C-OH peak area decreases while the ν_{AS} COO^- and ν_S COO^- peak areas increase with alginate present in the solution, further supporting the hypothesis of alginate co-adsorption.

The CD_2 scissoring modes of d_{31}-palmitic acid spread onto the $MgCl_2$ solutions corroborate the findings from the OH stretching and COOH stretching regions. At 10 mM $MgCl_2$, the salt water and alginate spectra nearly overlap (Figs. 5.7a and 5.7c). There is a small increase in peak intensity of the TC spectrum corresponding to the alginate solution which could be attributed to alginate weakly co-adsorbed to the TC monolayer. Then the alginate is squeezed out upon film compression, causing the peak intensity difference to disappear in the UC phase. The solution containing 53 mM $MgCl_2$ and alginate induces increased peak intensities in the d_{31}-palmitic acid CD_2 scissoring mode and the higher frequency regime relative to the spectra corresponding to the salt water solution (Figs. 5.7b and 5.7d). The signal enhancement is smaller in comparison to the system containing 10 mM $CaCl_2$ and alginate at pH 8.2, but the spectral trends match. Hence, the higher concentration of $MgCl_2$ facilitates some alginate co-adsorption to the monolayer through Mg^{2+} bridging interactions.

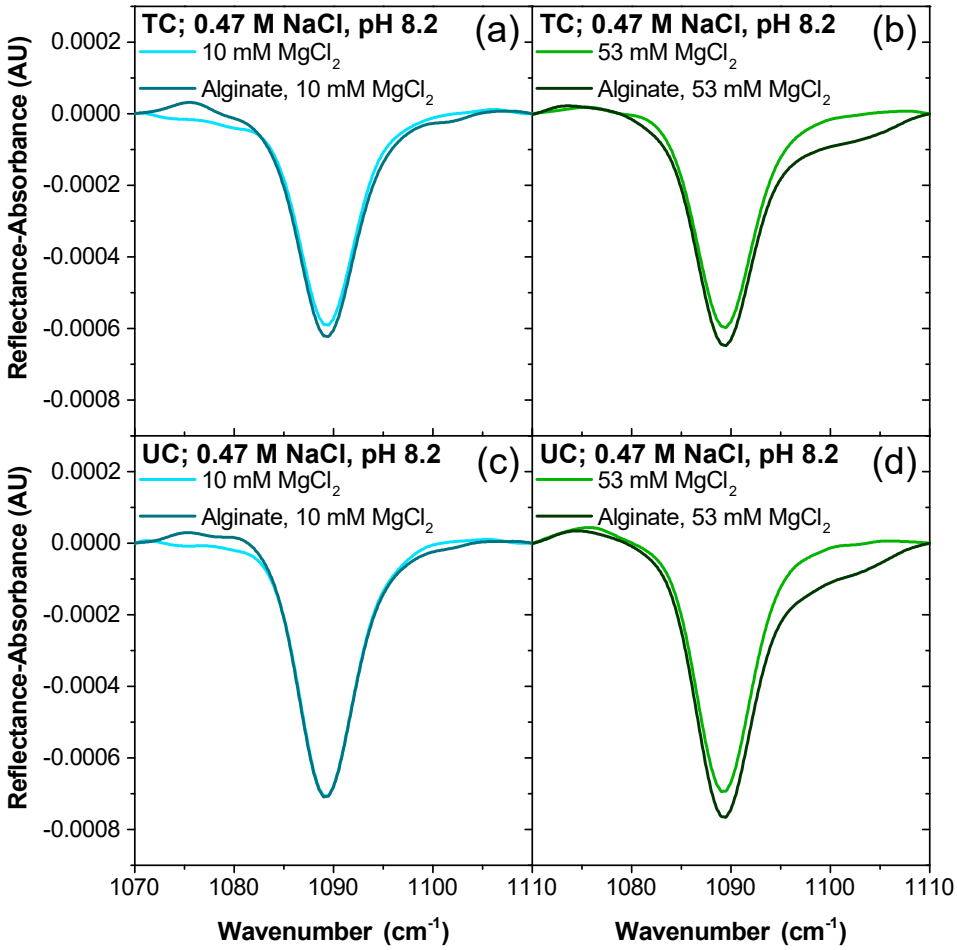

Figure 5.7: IRRAS spectra of the CD_2 scissoring mode region demonstrate weak alginate co-adsorption to the d_{31}-palmitic acid monolayer in the presence of 53 mM $MgCl_2$ at pH 8.2, and the spectra indicate no changes in the d_{31}-palmitic acid lattice packing upon adsorption. Spectral lines are color-coded to indicate differences in solution composition. Surface pressure was held constant in the **(a)**, **(b)** tilted condensed (5 mN/m) and **(c)**, **(d)** untilted condensed (25 mN/m) phases throughout spectral acquisition.

5.4 Conclusions

We directly observe alginate co-adsorption to an insoluble d_{31}-palmitic acid monolayer via divalent cationic bridging interactions using surface-sensitive infrared reflection-absorption spectroscopy (IRRAS), and the co-adsorption mechanism is summarized in Fig. 5.8. Ca^{2+} facilitates the greatest extent of alginate co-adsorption, as shown by the appearance of alginate vibrational modes in the IRRAS spectra and by the ∼27%

and ∼32% increase in surface coverage in the TC and UC phases, respectively. Alginate co-adsorption is dependent upon d_{31}-palmitic acid protonation state, however; d_{31}-palmitate promotes alginate co-adsorption in the presence of divalent cations, whereas protonation inhibits co-adsorption. Na^+ cations alone are insufficient in facilitating co-adsorption. Mg^{2+} induces ∼3 times weaker alginate co-adsorption at a seawater concentration of 53 mM in comparison to 10 mM Ca^{2+}, and Mg^{2+} induces minimal co-adsorption when matching the Ca^{2+} seawater concentration (10 mM). The hydration free energy of Mg^{2+} is much higher than that of Ca^{2+}, meaning that Mg^{2+} cannot shed its hydration shell as readily to facilitate bridging interactions between the d_{31}-palmitate and alginate carboxylate moieties. The presence of alginate perturbs the hydration structure and dehydrates the d_{31}-palmitic acid carboxylic acid headgroups, but alginate co-adsorption does not change the d_{31}-palmitic acid lattice packing structure. Alginate co-adsorption is largely confined to the subsurface region of the film. Consequently, surface pressure plays a minimal role in the extent of alginate co-adsorption.

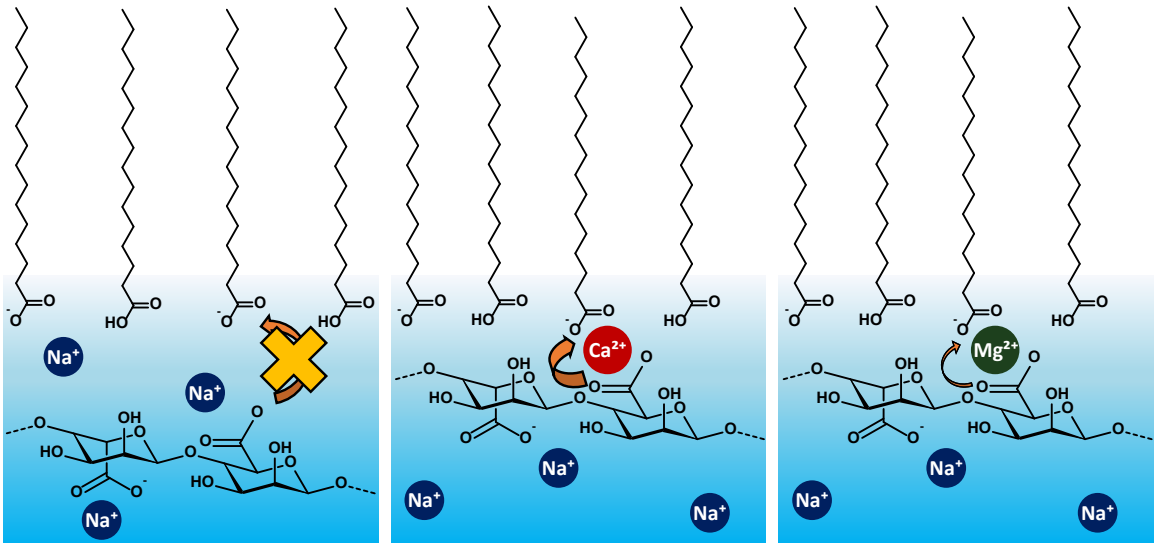

Figure 5.8: Schematic summarizing the alginate co-adsorption mechanism to a partially deprotonated d_{31}-palmitic acid monolayer via divalent cationic bridging.

Our detailed experimental and computational characterization of the divalent

cationic bridging interactions driving alginate co-adsorption to a sea surface microlayer (SSML) proxy film provides important physical and chemical insights into the potential mechanisms responsible for polysaccharide enrichment in sea spray aerosol (SSA). Ca^{2+} drives this bridging motif between the alginate and palmitic acid carboxylate moieties and outcompetes Mg^{2+} despite higher Mg^{2+} concentrations in seawater. Quantification of organic surface coverage via the OH stretching region integrated peak areas also provides a potentially useful parameter for aerosol representation in climate models. We demonstrate that soluble polysaccharides can interact electrostatically with other surface-active organic matter through seawater ionic bridging interactions, leading to polysaccharide surface enrichment in the SSML, and therefore, in SSA.

Chapter 6

Conclusions

The work described herein primarily concerns the physicochemical properties of surfactant films coating the aqueous surfaces of the sea surface microlayer (SSML) and of sea spray aerosol (SSA). The ocean covers the majority of Earth's surface, and SSA constitutes one of the most abundant sources of natural aerosol on the planet. Consequently, these marine interfaces play a significant role in global climate and require further characterization for improved Earth system model parameterization. The structure and organization of proxy marine surfactant films are studied through a combination of surface tensiometry, surface-sensitive spectroscopy, and computational chemistry. Additionally, the spectroscopic tools themselves are analyzed for their reliability in quantitative interpretation. Lastly, the cooperative adsorption of polysaccharides to a surfactant monolayer is studied to better understand the mechanisms driving saccharide enrichment in SSA.

It is known that fatty acids and other organic compounds form a film on SSA surfaces, and SSA particle surface-area-to-volume ratios are altered during aging in the marine boundary layer (MBL). To understand SSA surface organization and its role during dynamic atmospheric conditions, an SSA proxy fatty acid film and its individual components stearic acid (SA), palmitic acid (PA), and myristic acid (MA) were studied separately using surface pressure – area ($\Pi - A$) isotherms and Brewster

angle microscopy (BAM). The films were spread on an aqueous NaCl subphase at pH 8.2, 5.6, and 2.0 to mimic nascent to aged SSA aqueous core composition in the MBL, respectively. The individual fatty acid behavior differs from that of the SSA proxy film, and at nascent SSA pH the mixture yields a monolayer with intermediate rigidity that folds upon film compression to the collapse state. Acidification causes the SSA proxy film to become more rigid and form 3D nuclei. The results reveal film morphology alterations, which are related to SSA reflectivity, throughout various stages of SSA aging and provide a better understanding of SSA impacts on climate.

Surface-sensitive vibrational spectroscopy is a common tool for measuring molecular organization and intermolecular interactions at interfaces, such as proxy marine aqueous interfaces. Peak intensity ratios are typically used to extract molecular information from one-dimensional spectra, but vibrational coupling between surfactant molecules can manifest as signal depletion in one-dimensional spectra. Through a combination of experiment and theory, the emergence of vibrational exciton delocalization in infrared reflection-absorption spectra of soluble and insoluble surfactants at the air/water interface is observed. Vibrational coupling causes a significant decrease in peak intensities corresponding to C–F vibrational modes of perfluorooctanoic acid molecules. Vibrational excitons also form between arachidic acid surfactants within a compressed monolayer, manifesting as signal reduction of C–H stretching modes. Ionic composition of the aqueous phase impacts surfactant intermolecular distance, thereby modulating vibrational coupling strength between surfactants. The results serve as a cautionary tale against employing alkyl and fluoroalkyl vibrational peak intensities as proxies for concentration, although such analysis is ubiquitous in interface science.

In addition to surfactants, saccharides comprise a significant mass fraction of organic carbon in sea spray aerosol (SSA), but the mechanisms through which soluble saccharides are transferred from seawater to the ocean surface and eventu-

ally into SSA are not fully understood. Using a combination of surface-sensitive infrared reflection-absorption spectroscopy and surface tensiometry, it was demonstrated that the marine-relevant, anionic polysaccharide alginate co-adsorbs to an insoluble palmitic acid monolayer via divalent cationic bridging interactions. Ca^{2+} induces the greatest extent of alginate co-adsorption to the monolayer, evidenced by the 30% increase in surface coverage, whereas Mg^{2+} only facilitates one-third the extent of co-adsorption at seawater-relevant cation concentrations due to its strong hydration propensity. Na^{+} cations alone do not facilitate alginate co-adsorption, and palmitic acid protonation hinders the formation of divalent cationic bridges between the palmitate and alginate carboxylate moieties. Alginate co-adsorption is largely confined to the interfacial region beneath the monolayer headgroups, so surface pressure, and thus monolayer surface coverage, only changes the amount of alginate co-adsorption by less than 5%. These results provide physical and molecular insights into a potentially significant polysaccharide enrichment mechanism within the SSML.

Bibliography

[1] Millero, F. J. *Chemical Oceanography*, 4th ed.; Taylor & Francis: Boca Raton, 2013.

[2] de Leeuw, G.; Andreas, E. L.; Anguelova, M. D.; Fairall, C. W.; Lewis, E. R.; O'Dowd, C.; Schulz, M.; Schwartz, S. E. Production Flux of Sea Spray Aerosol. *Rev. Geophys.* **2011**, *49*, RG2001.

[3] Donaldson, D. J.; George, C. Sea-Surface Chemistry and Its Impact on the Marine Boundary Layer. *Environ. Sci. Technol.* **2012**, *46*, 10385–10389.

[4] Rossignol, S.; Tinel, L.; Bianco, A.; Passananti, M.; Brigante, M.; Donaldson, D. J.; George, C. Atmospheric Photochemistry at a Fatty Acid–Coated Air-Water Interface. *Science* **2016**, *353*, 699–702.

[5] Bertram, T. H.; Cochran, R. E.; Grassian, V. H.; Stone, E. A. Sea Spray Aerosol Chemical Composition: Elemental and Molecular Mimics for Laboratory Studies of Heterogeneous and Multiphase Reactions. *Chem. Soc. Rev.* **2018**, *47*, 2374–2400.

[6] Twomey, S. Pollution and the Planetary Albedo. *Atmos. Environ.* **1974**, *8*, 1251–1256.

[7] Gantt, B.; Xu, J.; Meskhidze, N.; Zhang, Y.; Nenes, A.; Ghan, S. J.; Liu, X.; Easter, R.; Zaveri, R. Global Distribution and Climate Forcing of Marine Organic Aerosol – Part 2: Effects on Cloud Properties and Radiative Forcing. *Atmos. Chem. Phys.* **2012**, *12*, 6555–6563.

[8] IPCC, 2014, In *Climate Change 2013: The Physical Science Basis: Working Group I Contribution to the Fifth Assessment Report of the Intergovernmental Panel on Climate Change*; Stocker, T. F., Qin, D., Plattner, G.-K., Tignor, M. M. B., Allen, S. K., Boschung, J., Nauels, A., Xia, Y., Bex, V., Midgley, P. M., Eds.; Cambridge University Press: New York, 2014.

[9] Moore, M. J.; Furutani, H.; Roberts, G. C.; Moffet, R. C.; Gilles, M. K.; Palenik, B.; Prather, K. A. Effect of Organic Compounds on Cloud Condensation Nuclei (CCN) Activity of Sea Spray Aerosol Produced by Bubble Bursting. *Atmos. Environ.* **2011**, *45*, 7462–7469.

[10] Orellana, M. V.; Matrai, P. A.; Leck, C.; Rauschenberg, C. D.; Lee, A. M.; Coz, E. Marine Microgels as a Source of Cloud Condensation Nuclei in the High Arctic. *Proc. Natl. Acad. Sci. U.S.A.* **2011**, *108*, 13612–13617.

[11] Modini, R. L. et al. Primary Marine Aerosol-Cloud Interactions off the Coast of California. *J. Geophys. Res. Atmos.* **2015**, *120*, 4282–4303.

[12] Sanchez, K. J. et al. Meteorological and Aerosol Effects on Marine Cloud Microphysical Properties. *J. Geophys. Res. Atmos.* **2016**, *121*, 4142–4161.

[13] Quinn, P. K.; Coffman, D. J.; Johnson, J. E.; Upchurch, L. M.; Bates, T. S. Small Fraction of Marine Cloud Condensation Nuclei Made up of Sea Spray Aerosol. *Nat. Geosci.* **2017**, *10*, 674–679.

[14] Brooks, S. D.; Thornton, D. C. Marine Aerosols and Clouds. *Annu. Rev. Mar. Sci.* **2018**, *10*, 289–313.

[15] Gaston, C.; Cahill, J.; Collins, D.; Suski, K.; Ge, J.; Barkley, A.; Prather, K.; Gaston, C. J.; Cahill, J. F.; Collins, D. B.; Suski, K. J.; Ge, J. Y.; Barkley, A. E.; Prather, K. A. The Cloud Nucleating Properties and Mixing State of Marine Aerosols Sampled along the Southern California Coast. *Atmosphere* **2018**, *9*, 52.

[16] Burrows, S. M.; Hoose, C.; Pöschl, U.; Lawrence, M. G. Ice Nuclei in Marine Air: Biogenic Particles or Dust? *Atmos. Chem. Phys.* **2013**, *13*, 245–267.

[17] Wilson, T. W. et al. A Marine Biogenic Source of Atmospheric Ice-Nucleating Particles. *Nature* **2015**, *525*, 234–238.

[18] DeMott, P. J. et al. Sea Spray Aerosol as a Unique Source of Ice Nucleating Particles. *Proc. Natl. Acad. Sci. U.S.A.* **2016**, *113*, 5797–5803.

[19] Ladino, L. A.; Yakobi-Hancock, J. D.; Kilthau, W. P.; Mason, R. H.; Si, M.; Li, J.; Miller, L. A.; Schiller, C. L.; Huffman, J. A.; Aller, J. Y.; Knopf, D. A.; Bertram, A. K.; Abbatt, J. P. D. Addressing the Ice Nucleating Abilities of Marine Aerosol: A Combination of Deposition Mode Laboratory and Field Measurements. *Atmos. Environ.* **2016**, *132*, 1–10.

[20] McCluskey, C. S. et al. A Dynamic Link between Ice Nucleating Particles Released in Nascent Sea Spray Aerosol and Oceanic Biological Activity during Two Mesocosm Experiments. *J. Atmos. Sci.* **2016**, *74*, 151–166.

[21] Chance, R. J.; Hamilton, J. F.; Carpenter, L. J.; Hackenberg, S. C.; Andrews, S. J.; Wilson, T. W. Water-Soluble Organic Composition of the Arctic Sea Surface Microlayer and Association with Ice Nucleation Ability. *Environ. Sci. Technol.* **2018**,

[22] McCluskey, C. S.; Hill, T. C. J.; Sultana, C. M.; Laskina, O.; Trueblood, J.; Santander, M. V.; Beall, C. M.; Michaud, J. M.; Kreidenweis, S. M.; Prather, K. A.; Grassian, V.; DeMott, P. J. A Mesocosm Double Feature: Insights into the Chemical Makeup of Marine Ice Nucleating Particles. *J. Atmos. Sci.* **2018**, *75*, 2405–2423.

[23] Mitts, B. A.; Wang, X.; Lucero, D. D.; Beall, C. M.; Deane, G. B.; DeMott, P. J.; Prather, K. A. Importance of Supermicron Ice Nucleating Particles in Nascent Sea Spray. *Geophys. Res. Lett.* **2021**, *48*, e2020GL089633.

[24] Ault, A. P.; Guasco, T. L.; Baltrusaitis, J.; Ryder, O. S.; Trueblood, J. V.; Collins, D. B.; Ruppel, M. J.; Cuadra-Rodriguez, L. A.; Prather, K. A.; Grassian, V. H. Heterogeneous Reactivity of Nitric Acid with Nascent Sea Spray Aerosol: Large Differences Observed between and within Individual Particles. *J. Phys. Chem. Lett.* **2014**, *5*, 2493–2500.

[25] Estillore, A. D.; Trueblood, J. V.; Grassian, V. H. Atmospheric Chemistry of Bioaerosols: Heterogeneous and Multiphase Reactions with Atmospheric Oxidants and Other Trace Gases. *Chem. Sci.* **2016**, *7*, 6604–6616.

[26] Trueblood, J. V.; Estillore, A. D.; Lee, C.; Dowling, J. A.; Prather, K. A.; Grassian, V. H. Heterogeneous Chemistry of Lipopolysaccharides with Gas-Phase Nitric Acid: Reactive Sites and Reaction Pathways. *J. Phys. Chem. A* **2016**, *120*, 6444–6450.

[27] Shrestha, M.; Luo, M.; Li, Y.; Xiang, B.; Xiong, W.; H. Grassian, V. Let There Be Light: Stability of Palmitic Acid Monolayers at the Air/Salt Water Interface in the Presence and Absence of Simulated Solar Light and a Photosensitizer. *Chem. Sci.* **2018**, *9*, 5716–5723.

[28] Mayer, K. J.; Wang, X.; Santander, M. V.; Mitts, B. A.; Sauer, J. S.; Sultana, C. M.; Cappa, C. D.; Prather, K. A. Secondary Marine Aerosol Plays a Dominant Role over Primary Sea Spray Aerosol in Cloud Formation. *ACS Cent. Sci.* **2020**, *6*, 2259–2266.

[29] Wang, X. et al. Microbial Control of Sea Spray Aerosol Composition: A Tale of Two Blooms. *ACS Cent. Sci.* **2015**, *1*, 124–131.

[30] Cochran, R. E. et al. Molecular Diversity of Sea Spray Aerosol Particles: Impact of Ocean Biology on Particle Composition and Hygroscopicity. *Chem* **2017**, *2*, 655–667.

[31] Cochran, R. E.; Ryder, O. S.; Grassian, V. H.; Prather, K. A. Sea Spray Aerosol: The Chemical Link between the Oceans, Atmosphere, and Climate. *Acc. Chem. Res.* **2017**, *50*, 599–604.

[32] Rastelli, E.; Corinaldesi, C.; Dell'Anno, A.; Lo Martire, M.; Greco, S.; Cristina Facchini, M.; Rinaldi, M.; O'Dowd, C.; Ceburnis, D.; Danovaro, R.

Transfer of Labile Organic Matter and Microbes from the Ocean Surface to the Marine Aerosol: An Experimental Approach. *Sci. Rep.* **2017**, *7*, 11475.

[33] Kirpes, R. M.; Bonanno, D.; May, N. W.; Fraund, M.; Barget, A. J.; Moffet, R. C.; Ault, A. P.; Pratt, K. A. Wintertime Arctic Sea Spray Aerosol Composition Controlled by Sea Ice Lead Microbiology. *ACS Cent. Sci.* **2019**, *5*, 1760–1767.

[34] Wurl, O.; Holmes, M. The Gelatinous Nature of the Sea-Surface Microlayer. *Mar. Chem.* **2008**, *110*, 89–97.

[35] Cunliffe, M.; Engel, A.; Frka, S.; Gašparović, B.; Guitart, C.; Murrell, J. C.; Salter, M.; Stolle, C.; Upstill-Goddard, R.; Wurl, O. Sea Surface Microlayers: A Unified Physicochemical and Biological Perspective of the Air–Ocean Interface. *Prog. Oceanogr.* **2013**, *109*, 104–116.

[36] Engel, A. et al. The Ocean's Vital Skin: Toward an Integrated Understanding of the Sea Surface Microlayer. *Front. Mar. Sci.* **2017**, *4*.

[37] Burrows, S. M.; Ogunro, O.; Frossard, A. A.; Russell, L. M.; Rasch, P. J.; Elliott, S. M. A Physically Based Framework for Modeling the Organic Fractionation of Sea Spray Aerosol from Bubble Film Langmuir Equilibria. *Atmos. Chem. Phys.* **2014**, *14*, 13601–13629.

[38] Burrows, S. M.; Gobrogge, E.; Fu, L.; Link, K.; Elliott, S. M.; Wang, H.; Walker, R. OCEANFILMS-2: Representing Coadsorption of Saccharides in Marine Films and Potential Impacts on Modeled Marine Aerosol Chemistry. *Geophys. Res. Lett.* **2016**, *43*, 8306–8313.

[39] Schill, S. R.; Burrows, S. M.; Hasenecz, E. S.; Stone, E. A.; Bertram, T. H. The Impact of Divalent Cations on the Enrichment of Soluble Saccharides in Primary Sea Spray Aerosol. *Atmosphere* **2018**, *9*, 476.

[40] Zhang, T.; Fiamingo, M.; Allen, H. C. Trace Metal Enrichment Driven by Phosphate Functional Group Binding Selectivity. *J. Geophys. Res. Oceans* **2018**, *123*, 5286–5297.

[41] Hoffman, E. J.; Duce, R. A. Factors Influencing the Organic Carbon Content of Marine Aerosols: A Laboratory Study. *J. Geophys. Res.* **1976**, *81*, 3667–3670.

[42] Thorpe, S. A. Bubble Clouds and the Dynamics of the Upper Ocean. *Q. J. R. Meteorol. Soc.* **1992**, *118*, 1–22.

[43] Bird, J. C.; de Ruiter, R.; Courbin, L.; Stone, H. A. Daughter Bubble Cascades Produced by Folding of Ruptured Thin Films. *Nature* **2010**, *465*, 759–762.

[44] O'Dowd, C. D.; Facchini, M. C.; Cavalli, F.; Ceburnis, D.; Mircea, M.; Decesari, S.; Fuzzi, S.; Yoon, Y. J.; Putaud, J.-P. Biogenically Driven Organic Contribution to Marine Aerosol. *Nature* **2004**, *431*, 676–680.

[45] O'Dowd, C. D.; de Leeuw, G. Marine Aerosol Production: A Review of the Current Knowledge. *Philos. Trans. R. Soc. Lond. Math. Phys. Eng. Sci.* **2007**, *365*, 1753–1774.

[46] Prather, K. A. et al. Bringing the Ocean into the Laboratory to Probe the Chemical Complexity of Sea Spray Aerosol. *Proc. Natl. Acad. Sci. U.S.A.* **2013**, *110*, 7550–7555.

[47] Quinn, P. K.; Collins, D. B.; Grassian, V. H.; Prather, K. A.; Bates, T. S. Chemistry and Related Properties of Freshly Emitted Sea Spray Aerosol. *Chem. Rev.* **2015**, *115*, 4383–4399.

[48] Tervahattu, H.; Hartonen, K.; Kerminen, V.-M.; Kupiainen, K.; Aarnio, P.; Koskentalo, T.; Tuck, A. F.; Vaida, V. New Evidence of an Organic Layer on Marine Aerosols. *J. Geophys. Res.* **2002**, *107*, AAC 1–1.

[49] Tervahattu, H.; Juhanoja, J.; Kupiainen, K. Identification of an Organic Coating on Marine Aerosol Particles by TOF-SIMS. *J. Geophys. Res.* **2002**, *107*, ACH 18–1.

[50] Mochida, M.; Kitamori, Y.; Kawamura, K.; Nojiri, Y.; Suzuki, K. Fatty Acids in the Marine Atmosphere: Factors Governing Their Concentrations and Evaluation of Organic Films on Sea-Salt Particles. *J. Geophys. Res.* **2002**, *107*, 4325.

[51] Marty, J. C.; Saliot, A.; Buat-Ménard, P.; Chesselet, R.; Hunter, K. A. Relationship between the Lipid Compositions of Marine Aerosols, the Sea Surface Microlayer, and Subsurface Water. *J. Geophys. Res. Oceans* **1979**, *84*, 5707–5716.

[52] Rad, F. M.; Leck, C.; Ilag, L. L.; Nilsson, U. Investigation of Ultrahigh-Performance Liquid Chromatography/Travelling-Wave Ion Mobility/Time-of-Flight Mass Spectrometry for Fast Profiling of Fatty Acids in the High Arctic Sea Surface Microlayer. *Rapid Commun. Mass Sp.* **2018**, *32*, 942–950.

[53] Cochran, R. E.; Laskina, O.; Jayarathne, T.; Laskin, A.; Laskin, J.; Lin, P.; Sultana, C.; Lee, C.; Moore, K. A.; Cappa, C. D.; Bertram, T. H.; Prather, K. A.; Grassian, V. H.; Stone, E. A. Analysis of Organic Anionic Surfactants in Fine and Coarse Fractions of Freshly Emitted Sea Spray Aerosol. *Environ. Sci. Technol.* **2016**, *50*, 2477–2486.

[54] Cincinelli, A.; Stortini, A. M.; Perugini, M.; Checchini, L.; Lepri, L. Organic Pollutants in Sea-Surface Microlayer and Aerosol in the Coastal Environment of Leghorn—(Tyrrhenian Sea). *Mar. Chem.* **2001**, *76*, 77–98.

[55] Wurl, O.; Obbard, J. P. A Review of Pollutants in the Sea-Surface Microlayer (SML): A Unique Habitat for Marine Organisms. *Mar. Pollut. Bull.* **2004**, *48*, 1016–1030.

[56] Ju, X.; Jin, Y.; Sasaki, K.; Saito, N. Perfluorinated Surfactants in Surface, Subsurface Water and Microlayer from Dalian Coastal Waters in China. *Environ. Sci. Technol.* **2008**, *42*, 3538–3542.

[57] Casas, G.; Martínez-Varela, A.; Roscales, J. L.; Vila-Costa, M.; Dachs, J.; Jiménez, B. Enrichment of Perfluoroalkyl Substances in the Sea-Surface Microlayer and Sea-Spray Aerosols in the Southern Ocean. *Environ. Pollut.* **2020**, *267*, 115512.

[58] Moody, C. A.; Field, J. A. Perfluorinated Surfactants and the Environmental Implications of Their Use in Fire-Fighting Foams. *Environ. Sci. Technol.* **2000**, *34*, 3864–3870.

[59] Sunderland, E. M.; Hu, X. C.; Dassuncao, C.; Tokranov, A. K.; Wagner, C. C.; Allen, J. G. A Review of the Pathways of Human Exposure to Poly- and Perfluoroalkyl Substances (PFASs) and Present Understanding of Health Effects. *J. Expo. Sci. Env. Epid.* **2019**, *29*, 131–147.

[60] Johansson, J. H.; Salter, M. E.; Navarro, J. C. A.; Leck, C.; Nilsson, E. D.; Cousins, I. T. Global Transport of Perfluoroalkyl Acids via Sea Spray Aerosol. *Environ. Sci.: Processes Impacts* **2019**, *21*, 635–649.

[61] Sha, B.; Johansson, J. H.; Benskin, J. P.; Cousins, I. T.; Salter, M. E. Influence of Water Concentrations of Perfluoroalkyl Acids (PFAAs) on Their Size-Resolved Enrichment in Nascent Sea Spray Aerosols. *Environ. Sci. Technol.* **2020**,

[62] Cochran, R. E.; Jayarathne, T.; Stone, E. A.; Grassian, V. H. Selectivity Across the Interface: A Test of Surface Activity in the Composition of Organic-Enriched Aerosols from Bubble Bursting. *J. Phys. Chem. Lett.* **2016**, *7*, 1692–1696.

[63] Cheng, S.; Du, L.; George, C. Understanding the Interfacial Behavior of Typical Perfluorocarboxylic Acids at Surfactant-Coated Aqueous Interfaces. *J. Geophys. Res. Atmos.* **2020**, *125*, e2019JD032182.

[64] Ghosh, N.; Roy, S.; Mondal, J. A. On the Behavior of Perfluorinated Persistent Organic Pollutants (POPs) at Environmentally Relevant Aqueous Interfaces: An Interplay of Hydrophobicity and Hydrogen Bonding. *Langmuir* **2020**, *36*, 3720–3729.

[65] Adams, E. M.; Casper, C. B.; Allen, H. C. Effect of Cation Enrichment on Dipalmitoylphosphatidylcholine (DPPC) Monolayers at the Air-Water Interface. *J. Colloid Interf. Sci.* **2016**, *478*, 353–364.

[66] Adams, E. M.; Verreault, D.; Jayarathne, T.; Cochran, R. E.; Stone, E. A.; Allen, H. C. Surface Organization of a DPPC Monolayer on Concentrated $SrCl_2$ and $ZnCl_2$ Solutions. *Phys. Chem. Chem. Phys.* **2016**, *18*, 32345–32357.

[67] Adams, E. M.; Wellen, B. A.; Thiraux, R.; Reddy, S. K.; Vidalis, A. S.; Paesani, F.; Allen, H. C. Sodium–Carboxylate Contact Ion Pair Formation Induces Stabilization of Palmitic Acid Monolayers at High pH. *Phys. Chem. Chem. Phys.* **2017**, *19*, 10481–10490.

[68] Rudd, B. A. W.; Vidalis, A. S.; Allen, H. C. Thermodynamic versus Non-Equilibrium Stability of Palmitic Acid Monolayers in Calcium-Enriched Sea Spray Aerosol Proxy Systems. *Phys. Chem. Chem. Phys.* **2018**, *20*, 16320–16332.

[69] Zhang, T.; Brantley, S. L.; Verreault, D.; Dhankani, R.; Corcelli, S. A.; Allen, H. C. Effect of pH and Salt on Surface PK_{a} of Phosphatidic Acid Monolayers. *Langmuir* **2018**, *34*, 530–539.

[70] Verdugo, P.; Alldredge, A. L.; Azam, F.; Kirchman, D. L.; Passow, U.; Santschi, P. H. The Oceanic Gel Phase: A Bridge in the DOM–POM Continuum. *Mar. Chem.* **2004**, *92*, 67–85.

[71] Azam, F.; Malfatti, F. Microbial Structuring of Marine Ecosystems. *Nat. Rev. Microbiol.* **2007**, *5*, 782–791.

[72] Verdugo, P.; V. Orellana, M.; Chin, W.-C.; W. Petersen, T.; van den Eng, G.; Benner, R.; I. Hedges, J. Marine Biopolymer Self-Assembly : Implications for Carbon Cycling in the Ocean. *Faraday Discuss.* **2008**, *139*, 393–398.

[73] Verdugo, P. Marine Microgels. *Annu. Rev. Mar. Sci.* **2012**, *4*, 375–400.

[74] Galgani, L.; Piontek, J.; Engel, A. Biopolymers Form a Gelatinous Microlayer at the Air-Sea Interface When Arctic Sea Ice Melts. *Sci. Rep.* **2016**, *6*, 29465.

[75] Chin, W.-C.; Orellana, M. V.; Verdugo, P. Spontaneous Assembly of Marine Dissolved Organic Matter into Polymer Gels. *Nature* **1998**, *391*, 568–572.

[76] Tanaka, T.; Fillmore, D.; Sun, S.-T.; Nishio, I.; Swislow, G.; Shah, A. Phase Transitions in Ionic Gels. *Phys. Rev. Lett.* **1980**, *45*, 1636–1639.

[77] Verdugo, P. Dynamics of Marine Biopolymer Networks. *Polym. Bull.* **2007**, *58*, 139–143.

[78] Jayarathne, T.; Sultana, C. M.; Lee, C.; Malfatti, F.; Cox, J. L.; Pendergraft, M. A.; Moore, K. A.; Azam, F.; Tivanski, A. V.; Cappa, C. D.; Bertram, T. H.; Grassian, V. H.; Prather, K. A.; Stone, E. A. Enrichment of Saccharides and Divalent Cations in Sea Spray Aerosol During Two Phytoplankton Blooms. *Environ. Sci. Technol.* **2016**, *50*, 11511–11520.

[79] Russell, L. M.; Hawkins, L. N.; Frossard, A. A.; Quinn, P. K.; Bates, T. S. Carbohydrate-like Composition of Submicron Atmospheric Particles and Their Production from Ocean Bubble Bursting. *Proc. Natl. Acad. Sci. U.S.A.* **2010**, *107*, 6652–6657.

[80] Hawkins, L. N.; Russell, L. M. Polysaccharides, Proteins, and Phytoplankton Fragments: Four Chemically Distinct Types of Marine Primary Organic Aerosol Classified by Single Particle Spectromicroscopy. *Adv. Meteorol.* **2010**, *2010*, 1–14.

[81] IPCC, 2013, In *Climate Change 2014: Synthesis Report*; Core Writing Team„ Pachauri, R. K., Meyer, L., Eds.; Intergovernmental Panel on Climate Change: Geneva, Switzerland, 2015; Includes bibliographical references and index.

[82] Carslaw, K. S.; Lee, L. A.; Reddington, C. L.; Pringle, K. J.; Rap, A.; Forster, P. M.; Mann, G. W.; Spracklen, D. V.; Woodhouse, M. T.; Regayre, L. A.; Pierce, J. R. Large Contribution of Natural Aerosols to Uncertainty in Indirect Forcing. *Nature* **2013**, *503*, 67–71.

[83] Elliott, S.; Burrows, S. M.; Deal, C.; Liu, X.; Long, M.; Ogunro, O.; Russell, L. M.; Wingenter, O. Prospects for Simulating Macromolecular Surfactant Chemistry at the Ocean–Atmosphere Boundary. *Environ. Res. Lett.* **2014**, *9*, 064012.

[84] Ogunro, O. O.; Burrows, S. M.; Elliott, S.; Frossard, A. A.; Hoffman, F.; Letscher, R. T.; Moore, J. K.; Russell, L. M.; Wang, S.; Wingenter, O. W. Global Distribution and Surface Activity of Macromolecules in Offline Simulations of Marine Organic Chemistry. *Biogeochemistry* **2015**, *126*, 25–56.

[85] Elliott, S. et al. Does Marine Surface Tension Have Global Biogeography? Addition for the OCEANFILMS Package. *Atmosphere* **2018**, *9*, 216.

[86] Chattoraj, D. K.; Birdi, K. S. *Adsorption and the Gibbs Surface Excess*; Plenum Press: New York, 1984; Includes indexes.

[87] Butt, H.-J.; Graf, K.; Kappl, M. *Physics and Chemistry of Interfaces*, third, revised and enlarged edition ed.; Wiley-VCH Verlag GmbH & Co. KGaA: Weinheim, Germany, 2013; Previous ed.: 2006.

[88] Israelachvili, J. N. *Intermolecular and Surface Forces*, 3rd ed.; Academic Press: Burlington, MA, 2011.

[89] Hantal, G.; Sega, M.; Horvai, G.; Jedlovszky, P. Contribution of Different Molecules and Moieties to the Surface Tension in Aqueous Surfactant Solutions. *J. Phys. Chem. C* **2019**, *123*, 16660–16670.

[90] Zhao, X.; Nathanson, G. M.; Andersson, G. G. Competing Segregation of Br– and Cl– to a Surface Coated with a Cationic Surfactant: Direct Measurements of Ion and Solvent Depth Profiles. *J. Phys. Chem. A* **2020**,

[91] Zhao, X.; Nathanson, G. M.; Andersson, G. G. Experimental Depth Profiles of Surfactants, Ions, and Solvent at the Angstrom Scale: Studies of Cationic and Anionic Surfactants and Their Salting Out. *J. Phys. Chem. B* **2020**, *124*, 2218–2229.

[92] Asadzadeh Shahir, A.; Arabadzhieva, D.; Petkova, H.; Karakashev, S. I.; Nguyen, A. V.; Mileva, E. Effect of Under-Monolayer Adsorption on Foamability, Rheological Characteristics, and Dynamic Behavior of Fluid Interfaces: Experimental Evidence for the Guggenheim Extended Interface Model. *J. Phys. Chem. C* **2017**, *121*, 11472–11487.

[93] Qazi, M. J.; Schlegel, S. J.; Backus, E. H.; Bonn, M.; Bonn, D.; Shahidzadeh, N. Dynamic Surface Tension of Surfactants in the Presence of High Salt Concentrations. *Langmuir* **2020**,

[94] Nakahara, H.; Shibata, O.; Moroi, Y. Examination of Surface Adsorption of Cetyltrimethylammonium Bromide and Sodium Dodecyl Sulfate. *J. Phys. Chem. B* **2011**, *115*, 9077–9086.

[95] Casper, C. B.; Verreault, D.; Adams, E. M.; Hua, W.; Allen, H. C. Surface Potential of DPPC Monolayers on Concentrated Aqueous Salt Solutions. *J. Phys. Chem. B* **2016**, *120*, 2043–2052.

[96] Teer, E.; Knobler, C. M.; Lautz, C.; Wurlitzer, S.; Kildae, J.; Fischer, T. M. Optical Measurements of the Phase Diagrams of Langmuir Monolayers of Fatty Acid, Ester, and Alcohol Mixtures by Brewster-Angle Microscopy. *J. Chem. Phys.* **1997**, *106*, 1913–1920.

[97] Carter-Fenk, K. A.; Allen, H. C. Collapse Mechanisms of Nascent and Aged Sea Spray Aerosol Proxy Films. *Atmosphere* **2018**, *9*, 503.

[98] Baumler, S. M.; Allen, H. C. In *Physical Chemistry of Gas-Liquid Interfaces*; Faust, J. A., House, J. E., Eds.; Developments in Physical & Theoretical Chemistry; Elsevier, 2018; pp 105–133.

[99] Lu, J. R.; Thomas, R. K.; Penfold, J. Surfactant Layers at the Air/Water Interface: Structure and Composition. *Adv. Colloid Interfac.* **2000**, *84*, 143–304.

[100] Penfold, J.; Thomas, R. K.; Staples, E.; Tucker, I. *Mesoscale Phenomena in Fluid Systems*; ACS Symposium Series; American Chemical Society, 2003; Vol. 861; pp 96–115.

[101] Carter, K. A. Impacts of Salt and pH on the Phase Behavior of Sea Spray Aerosol Proxy Films. Ph.D. thesis, The Ohio State University, 2018.

[102] Martínez-Balbuena, L.; Arteaga-Jiménez, A.; Hernández-Zapata, E.; Márquez-Beltrán, C. Applicability of the Gibbs Adsorption Isotherm to the Analysis of Experimental Surface-Tension Data for Ionic and Nonionic Surfactants. *Adv. Colloid Interfac.* **2017**, *247*, 178–184.

[103] Costanza, J.; Arshadi, M.; Abriola, L. M.; Pennell, K. D. Accumulation of PFOA and PFOS at the Air–Water Interface. *Environ. Sci. Technol. Lett.* **2019**, *6*, 487–491.

[104] von Szyszkowski, B. Experimentelle Studien Über Kapillare Eigenschaften Der Wässerigen Lösungen von Fettsäuren. *Z. Für Phys. Chem.* **1908**, *64U*, 385–414.

[105] Vecitis, C. D.; Park, H.; Cheng, J.; Mader, B. T.; Hoffmann, M. R. Enhancement of Perfluorooctanoate and Perfluorooctanesulfonate Activity at Acoustic Cavitation Bubble Interfaces. *J. Phys. Chem. C* **2008**, *112*, 16850–16857.

[106] Lunkenheimer, K.; Geggel, K.; Prescher, D. Role of Counterion in the Adsorption Behavior of 1:1 Ionic Surfactants at Fluid Interfaces—Adsorption Properties of Alkali Perfluoro-n-Octanoates at the Air/Water Interface. *Langmuir* **2017**, *33*, 10216–10224.

[107] Langmuir, I. The Constitution and Fundamental Properties of Solids and Liquids. II. Liquids. *J. Am. Chem. Soc.* **1917**, *39*, 1848–1906.

[108] Lunkenheimer, K.; Prescher, D.; Hirte, R.; Geggel, K. Adsorption Properties of Surface Chemically Pure Sodium Perfluoro-n-Alkanoates at the Air/Water Interface: Counterion Effects within Homologous Series of 1:1 Ionic Surfactants. *Langmuir* **2015**, *31*, 970–981.

[109] Asadzadeh Shahir, A.; Nguyen, K. T.; Nguyen, A. V. A Sum-Frequency Generation Spectroscopic Study of the Gibbs Analysis Paradox: Monolayer or Sub-Monolayer Adsorption? *Phys. Chem. Chem. Phys.* **2016**, *18*, 8794–8805.

[110] Peng, M.; Duignan, T. T.; Zhao, X. S.; Nguyen, A. V. Surface Potential Explained: A Surfactant Adsorption Model Incorporating Realistic Layer Thickness. *J. Phys. Chem. B* **2020**, *124*, 3195–3205.

[111] Peng, M.; Nguyen, A. V.; Wang, J.; Miller, R. A Critical Review of the Model Fitting Quality and Parameter Stability of Equilibrium Adsorption Models. *Adv. Colloid Interfac.* **2018**, *262*, 50–68.

[112] Peng, M.; Nguyen, A. V. Adsorption of Ionic Surfactants at the Air-Water Interface: The Gap between Theory and Experiment. *Adv. Colloid Interfac.* **2020**, *275*, 102052.

[113] Gaines, G. L. *Insoluble Monolayers at Liquid-Gas Interfaces*; Interscience Publishers: New York, 1966.

[114] Mohwald, H. Phospholipid and Phospholipid-Protein Monolayers at the Air/Water Interface. *Annu. Rev. Phys. Chem.* **1990**, *41*, 441–476.

[115] Ma, G.; Allen, H. C. Condensing Effect of Palmitic Acid on DPPC in Mixed Langmuir Monolayers. *Langmuir* **2007**, *23*, 589–597.

[116] Smith, R. D.; Berg, J. C. The Collapse of Surfactant Monolayers at the Air—Water Interface. *J. Colloid Interf. Sci.* **1980**, *74*, 273–286.

[117] Ybert, C.; Lu, W.; Möller, G.; Knobler, C. M. Collapse of a Monolayer by Three Mechanisms. *J. Phys. Chem. B* **2002**, *106*, 2004–2008.

[118] Lee, K. Y. C. Collapse Mechanisms of Langmuir Monolayers. *Annu. Rev. Phys. Chem.* **2008**, *59*, 771–791.

[119] Hecht, E. *Optics*, 5th ed.; Pearson Education, Inc: Boston, 2017.

[120] Tompkins, H. G.; McGahan, W. A. *Spectroscopic Ellipsometry and Reflectometry: A User's Guide*; Wiley: New York, 1999.

[121] Born, M.; Wolf, E. *Principles of Optics: Electromagnetic Theory of Propagation, Interference, and Diffraction of Light*, 5th ed.; Pergamon Press: Oxford, New York, 1975.

[122] Bernath, P. F. *Spectra of Atoms and Molecules*, third ed. ed.; Oxford University Press: Oxford ; New York, 2016.

[123] Willock, D. J. *Molecular Symmetry*; John Wiley & Sons, Ltd, 2009; pp 325–338.

[124] Frenkel, J. On the Transformation of Light into Heat in Solids. I. *Phys. Rev.* **1931**, *37*, 17–44.

[125] Hexter, R. M. Intermolecular Coupling of Vibrations in Molecular Crystals: A Vibrational Exciton Approach. *J. Chem. Phys.* **1960**, *33*, 1833–1841.

[126] Davydov, A. S. The Theory of Molecular Excitons. *Sov. Phys. Usp.* **1964**, *7*, 145.

[127] Signorell, R. Verification of the Vibrational Exciton Approach for CO2 and N2O Nanoparticles. *J. Chem. Phys.* **2003**, *118*, 2707–2715.

[128] Firanescu, G.; Hermsdorf, D.; Ueberschaer, R.; Signorell, R. Large Molecular Aggregates: From Atmospheric Aerosols to Drug Nanoparticles. *Phys. Chem. Chem. Phys.* **2006**, *8*, 4149–4165.

[129] Firanescu, G.; Luckhaus, D.; Signorell, R. Size Effects in the Infrared Spectra of NH3 Ice Nanoparticles Studied by a Combined Molecular Dynamics and Vibrational Exciton Approach. *J. Chem. Phys.* **2006**, *125*, 144501.

[130] Hénon, S.; Meunier, J. Microscope at the Brewster Angle: Direct Observation of First-order Phase Transitions in Monolayers. *Rev. Sci. Instrum.* **1991**, *62*, 936–939.

[131] Hoenig, D.; Moebius, D. Direct Visualization of Monolayers at the Air-Water Interface by Brewster Angle Microscopy. *J. Phys. Chem.* **1991**, *95*, 4590–4592.

[132] Hosoi, K.; Ishikawa, T.; Tomioka, A.; Miyano, K. Quantitative Image Analysis in Brewster Angle Microscopy: Molecular Tilt of a Stearic Acid Monolayer on Water. *Jpn. J. Appl. Phys.* **1993**, *32*, L135–L137.

[133] Overbeck, G. A.; Hoenig, D.; Moebius, D. Visualization of First- and Second-Order Phase Transitions in Eicosanol Monolayers Using Brewster Angle Microscopy. *Langmuir* **1993**, *9*, 555–560.

[134] Fischer, T. M.; Bruinsma, R. F.; Knobler, C. M. Textures of Surfactant Monolayers. *Phys. Rev. E* **1994**, *50*, 413–428.

[135] Overbeck, G. A.; Hönig, D.; Möbius, D. Stars, Stripes and Shells in Monolayers: Simulation of the Molecular Arrangement in Schlieren Structures. *Thin Solid Films* **1994**, *242*, 213–219.

[136] Overbeck, G. A.; Hönig, D.; Wolthaus, L.; Gnade, M.; Möbius, D. Observation of Bond Orientational Order in Floating and Transferred Monolayers with Brewster Angle Microscopy. *Thin Solid Films* **1994**, *242*, 26–32.

[137] Tsao, M.-W.; Fischer, T. M.; Knobler, C. M. Quantitative Analysis of Brewster-Angle Microscope Images of Tilt Order in Langmuir Monolayer Domains. *Langmuir* **1995**, *11*, 3184–3188.

[138] Weidemann, G.; Vollhardt, D. Long Range Tilt Orientational Order in Fatty Acid Ethyl Ester Monolayers. *Langmuir* **1996**, *12*, 5114–5119.

[139] Lautz, C.; Fischer, T. M. Discontinuities in the Tilt Angle of Octadecanol Langmuir Monolayers As Observed with Brewster Angle Autocorrelation Spectroscopy. *J. Phys. Chem. B* **1997**, *101*, 8790–8793.

[140] Lautz, C.; Fischer, T. M.; Kildea, J. Hysteresis Effects at the Tilted to Non-tilted Transition in Octadecanol Monolayers as Observed with Brewster Angle Autocorrelation Spectroscopy. *J. Chem. Phys.* **1997**, *106*, 7448–7453.

[141] Lautz, C.; Fischer, T. M. Determination of the Tilt Angle of Langmuir Monolayers with Brewster Angle Autocorrelation Spectroscopy and Quantitative Image Analysis in Brewster Angle Microscopy: A Comparison between Two Different Methods. *Jpn. J. Appl. Phys.* **1997**, *36*, 5703–5706.

[142] de Mul, M. N. G.; Mann, J. A. Determination of the Thickness and Optical Properties of a Langmuir Film from the Domain Morphology by Brewster Angle Microscopy. *Langmuir* **1998**, *14*, 2455–2466.

[143] Rodríguez Patino, J. M.; Sánchez, C. C.; Rodríguez Niño, M. R. Morphological and Structural Characteristics of Monoglyceride Monolayers at the Air-Water Interface Observed by Brewster Angle Microscopy. *Langmuir* **1999**, *15*, 2484–2492.

[144] Fernsler, J. G.; Zasadzinski, J. A. Competitive Adsorption: A Physical Model for Lung Surfactant Inactivation. *Langmuir* **2009**, *25*, 8131–8143.

[145] Miñones, J.; Pais, S.; Miñones, J.; Conde, O.; Dynarowicz-Łątka, P. Interactions between Membrane Sterols and Phospholipids in Model Mammalian and Fungi Cellular Membranes — A Langmuir Monolayer Study. *Biophys. Chem.* **2009**, *140*, 69–77.

[146] Roldán-Carmona, C.; Giner-Casares, J. J.; Pérez-Morales, M.; Martín-Romero, M. T.; Camacho, L. Revisiting the Brewster Angle Microscopy: The Relevance of the Polar Headgroup. *Adv. Colloid Interfac.* **2012**, *173*, 12–22.

[147] Vollhardt, D. Brewster Angle Microscopy: A Preferential Method for Mesoscopic Characterization of Monolayers at the Air/Water Interface. *Curr. Opin. Colloid In.* **2014**, *19*, 183–197.

[148] Daear, W.; Mahadeo, M.; Prenner, E. J. Applications of Brewster Angle Microscopy from Biological Materials to Biological Systems. *Biochim. Biophys. Acta BBA - Biomembr.* **2017**, *1859*, 1749–1766.

[149] Fernsler, J.; Nguyen, V.; Wallum, A.; Benz, N.; Hamlin, M.; Pilgram, J.; Vanderpoel, H.; Lau, R. A LEGO Mindstorms Brewster Angle Microscope. *Am. J. Phys.* **2017**, *85*, 655–662.

[150] Sun, Z.; Zheng, D.; Baldelli, S. Distortion Correction for a Brewster Angle Microscope Using an Optical Grating. *Anal. Chem.* **2017**, *89*, 2186–2190.

[151] Baszkin, A., Norde, W., Eds. *Physical Chemistry of Biological Interfaces*; M. Dekker: New York, 2000.

[152] Hale, G. M.; Querry, M. R. Optical Constants of Water in the 200-Nm to 200-Mm Wavelength Region. *Appl. Opt., AO* **1973**, *12*, 555–563.

[153] Nagata, Y.; Hasegawa, T.; Backus, E. H. G.; Usui, K.; Yoshimune, S.; Ohto, T.; Bonn, M. The Surface Roughness, but Not the Water Molecular Orientation Varies with Temperature at the Water–Air Interface. *Phys. Chem. Chem. Phys.* **2015**, *17*, 23559–23564.

[154] Mendelsohn, R.; Brauner, J. W.; Gericke, A. External Infrared Reflection Absorption Spectrometry of Monolayer Films at the Air-Water Interface. *Annu. Rev. Phys. Chem.* **1995**, *46*, 305–334.

[155] Mendelsohn, R.; Flach, C. R. *Handbook of Vibrational Spectroscopy*; John Wiley & Sons, Ltd, 2006.

[156] Zheng, J.; Leblanc, R. M. *Interface Science and Technology*; Elsevier, 2007; Vol. 14; pp 247–276.

[157] Gericke, A.; Hühnerfuss, H. In Situ Investigation of Saturated Long-Chain Fatty Acids at the Air/Water Interface by External Infrared Reflection-Absorption Spectrometry. *J. Phys. Chem.* **1993**, *97*, 12899–12908.

[158] Gericke, A.; Hühnerfuss, H. The Effect of Cations on the Order of Saturated Fatty Acid Monolayers at the Air-Water Interface as Determined by Infrared Reflection-Absorption Spectrometry. *Thin Solid Films* **1994**, *245*, 74–82.

[159] Gericke, A.; Hühnerfuss, H. Investigation of Z- and E-Unsaturated Fatty Acids, Fatty Acid Esters, and Fatty Alcohols at the Air/Water Interface by Infrared Spectroscopy. *Langmuir* **1995**, *11*, 225–230.

[160] Gericke, A.; Hühnerfuss, H. The Conformational Order and Headgroup Structure of Long-Chain Alkanoic Acid Ester Monolayers at the Air/Water Interface. *Berichte Bunsenges. Für Phys. Chem.* **1995**, *99*, 641–650.

[161] Neumann, V.; Gericke, A.; Hühnerfuss, H. Comparison of Enantiomeric and Racemic Monolayers of 2-Hydroxyhexadecanoic Acid by External Infrared Reflection-Absorption Spectroscopy. *Langmuir* **1995**, *11*, 2206–2212.

[162] Gericke, A.; Brauner, J. W.; Erukulla, R. K.; Bittman, R.; Mendelsohn, R. In-Situ Investigation of Partially Deuterated Fatty Acid and Phospholipid Monolayers at the Air-Water Interface by IR Reflection-Absorption Spectroscopy. *Thin Solid Films* **1996**, *284*, 428–431.

[163] Gericke, A.; Mendelsohn, R. Partial Chain Deuteration as an IRRAS Probe of Conformational Order of Different Regions in Hexadecanoic Acid Monolayers at the Air/Water Interface. *Langmuir* **1996**, *12*, 758–762.

[164] Mao, L.; Ritcey, A. M.; Desbat, B. Evaluation of Molecular Orientation in a Polymeric Monolayer at the Air-Water Interface by Polarization-Modulated Infrared Spectroscopy. *Langmuir* **1996**, *12*, 4754–4759.

[165] Flach, C. R.; Gericke, A.; Mendelsohn, R. Quantitative Determination of Molecular Chain Tilt Angles in Monolayer Films at the Air/Water Interface: Infrared Reflection/Absorption Spectroscopy of Behenic Acid Methyl Ester. *J. Phys. Chem. B* **1997**, *101*, 58–65.

[166] Sakai, H.; Umemura, J. Molecular Orientation in Langmuir Films of 12-Hydroxystearic Acid Studied by Infrared External-Reflection Spectroscopy. *Langmuir* **1998**, *14*, 6249–6255.

[167] Flach, C. R.; Xu, Z.; Bi, X.; Brauner, J. W.; Mendelsohn, R. Improved IRRAS Apparatus for Studies of Aqueous Monolayer Films: Determination of the Orientation of Each Chain in a Fatty-Acid Homogeneous Ceramide 2. *Appl. Spectrosc.* **2001**, *55*, 1060–1066.

[168] Prosser, A. J.; Franses, E. I. Infrared Reflection Absorption Spectroscopy (IRRAS) of Aqueous Nonsurfactant Salts, Ionic Surfactants, and Mixed Ionic Surfactants. *Langmuir* **2002**, *18*, 9234–9242.

[169] Brauner, J. W.; Flach, C. R.; Xu, Z.; Bi, X.; Lewis, R. N. A. H.; McElhaney, R. N.; Gericke, A.; Mendelsohn, R. Quantitative Functional Group Orientation in Langmuir Films by Infrared Reflection-Absorption Spectroscopy: CO Groups in Behenic Acid Methyl Ester and Sn2-13C-DSPC. *J. Phys. Chem. B* **2003**, *107*, 7202–7211.

[170] Wang, Y.; Du, X.; Guo, L.; Liu, H. Chain Orientation and Headgroup Structure in Langmuir Monolayers of Stearic Acid and Metal Stearate (Ag, Co, Zn, and Pb) Studied by Infrared Reflection-Absorption Spectroscopy. *J. Chem. Phys.* **2006**, *124*, 134706.

[171] Muro, M.; Itoh, Y.; Hasegawa, T. A Conformation and Orientation Model of the Carboxylic Group of Fatty Acids Dependent on Chain Length in a Langmuir Monolayer Film Studied by Polarization-Modulation Infrared Reflection Absorption Spectroscopy. *J. Phys. Chem. B* **2010**, *114*, 11496–11501.

[172] Wang, H.; Coss, C. S.; Mudalige, A.; Polt, R. L.; Pemberton, J. E. A PM-IRRAS Investigation of Monorhamnolipid Orientation at the Air–Water Interface. *Langmuir* **2013**, *29*, 4441–4450.

[173] Goto, T. E.; Caseli, L. Understanding the Collapse Mechanism in Langmuir Monolayers through Polarization Modulation-Infrared Reflection Absorption Spectroscopy. *Langmuir* **2013**, *29*, 9063–9071.

[174] Simon-Kutscher, J.; Gericke, A.; Hühnerfuss, H. Effect of Bivalent Ba, Cu, Ni, and Zn Cations on the Structure of Octadecanoic Acid Monolayers at the Air-Water Interface As Determined by External Infrared Reflection-Absorption Spectroscopy. *Langmuir* **1996**, *12*, 1027–1034.

[175] Johann, R.; Vollhardt, D.; Möhwald, H. Study of the pH Dependence of Head Group Bonding in Arachidic Acid Monolayers by Polarization Modulation Infrared Reflection Absorption Spectroscopy. *Colloid Surface A.* **2001**, *182*, 311–320.

[176] Le Calvez, E.; Blaudez, D.; Buffeteau, T.; Desbat, B. Effect of Cations on the Dissociation of Arachidic Acid Monolayers on Water Studied by Polarization-Modulated Infrared Reflection-Absorption Spectroscopy. *Langmuir* **2001**, *17*, 670–674.

[177] Muro, M.; Harada, M.; Okada, T.; Hasegawa, T. Molecular Rearrangement in a Zinc Stearate Langmuir Film Dependent on a Film Preparation Method Studied Using Polarization-Modulation Infrared Reflection Absorption Spectroscopy and X-Ray Absorption Fine Structure. *J. Phys. Chem. B* **2012**, *116*, 3148–3154.

[178] Griffith, E. C.; Vaida, V. Ionization State of L-Phenylalanine at the Air–Water Interface. *J. Am. Chem. Soc.* **2013**, *135*, 710–716.

[179] Luo, M.; Wauer, N. A.; Angle, K. J.; Dommer, A. C.; Song, M.; Nowak, C. M.; Amaro, R. E.; Grassian, V. H. Insights into the Behavior of Nonanoic Acid and Its Conjugate Base at the Air/Water Interface through a Combined Experimental and Theoretical Approach. *Chem. Sci.* **2020**, *11*, 10647–10656.

[180] Neal, J. F.; Rogers, M. M.; Smeltzer, M. A.; Carter-Fenk, K. A.; Grooms, A. J.; Zerkle, M. M.; Allen, H. C. Sodium Drives Interfacial Equilibria for Semi-Soluble Phosphoric and Phosphonic Acids of Model Sea Spray Aerosol Surfaces. *ACS Earth Space Chem.* **2020**, *4*, 1549–1557.

[181] Dahmen-Levison, U.; Brezesinski, G. Methyl-Branched Glycerophosphocholines: Monolayer Disorder and Its Effect on the Rate of Phospholipase A2 Catalyzed Hydrolysis. *Phys. Chem. Chem. Phys.* **2000**, *2*, 4605–4608.

[182] Meinders, M. B.; van den Bosch, G. G.; de Jongh, H. H. Adsorption Properties of Proteins at and near the Air/Water Interface from IRRAS Spectra of Protein Solutions. *Eur Biophys J* **2001**, *30*, 256–267.

[183] Lavoie, H.; Desbat, B.; Vaknin, D.; Salesse, C. Structure of Rhodopsin in Monolayers at the Air-Water Interface: A PM-IRRAS and X-Ray Reflectivity Study. *Biochemistry* **2002**, *41*, 13424–13434.

[184] Brezesinski, G.; Möhwald, H. Langmuir Monolayers to Study Interactions at Model Membrane Surfaces. *Adv. Colloid Interfac.* **2003**, *100-102*, 563–584.

[185] Desmeules, P.; Penney, S.-É.; Desbat, B.; Salesse, C. Determination of the Contribution of the Myristoyl Group and Hydrophobic Amino Acids of Recoverin on Its Dynamics of Binding to Lipid Monolayers. *Biophys. J.* **2007**, *93*, 2069–2082.

[186] Amado, E.; Kerth, A.; Blume, A.; Kressler, J. Infrared Reflection Absorption Spectroscopy Coupled with Brewster Angle Microscopy for Studying Interactions of Amphiphilic Triblock Copolymers with Phospholipid Monolayers. *Langmuir* **2008**, *24*, 10041–10053.

[187] Wang, L.; Brauner, J. W.; Mao, G.; Crouch, E.; Seaton, B.; Head, J.; Smith, K.; Flach, C. R.; Mendelsohn, R. Interaction of Recombinant Surfactant Protein D with Lipopolysaccharide: Conformation and Orientation of Bound Protein by IRRAS and Simulations. *Biochemistry* **2008**, *47*, 8103–8113.

[188] Mendelsohn, R.; Mao, G.; Flach, C. R. Infrared Reflection–Absorption Spectroscopy: Principles and Applications to Lipid–Protein Interaction in Langmuir Films. *B.B.A.-Biomembranes* **2010**, *1798*, 788–800.

[189] Nasir, M. N.; Besson, F. Conformational Analyses of Bacillomycin D, a Natural Antimicrobial Lipopeptide, Alone or in Interaction with Lipid Monolayers at the Air–Water Interface. *J. Colloid Interf. Sci.* **2012**, *387*, 187–193.

[190] Hama, T.; Kouchi, A.; Watanabe, N.; Enami, S.; Shimoaka, T.; Hasegawa, T. In Situ Nondestructive Analysis of Kalanchoe Pinnata Leaf Surface Structure by Polarization-Modulation Infrared Reflection–Absorption Spectroscopy. *J. Phys. Chem. B* **2017**, *121*, 11124–11131.

[191] Liu, W.; Li, S.; Wang, Z.; Yan, E. C. Y.; Leblanc, R. M. Characterization of Surface-Active Biofilm Protein BslA in Self-Assembling Langmuir Monolayer at the Air–Water Interface. *Langmuir* **2017**, *33*, 7548–7555.

[192] Neal, J. F.; Zhao, W.; Grooms, A. J.; Flood, A. H.; Allen, H. C. Arginine–Phosphate Recognition Enhanced in Phospholipid Monolayers at Aqueous Interfaces. *J. Phys. Chem. C* **2018**, *122*, 26362–26371.

[193] Luo, M.; Dommer, A. C.; Schiffer, J. M.; Rez, D. J.; Mitchell, A. R.; Amaro, R. E.; Grassian, V. H. Surfactant Charge Modulates Structure and Stability of Lipase-Embedded Monolayers at Marine-Relevant Aerosol Surfaces. *Langmuir* **2019**, *35*, 9050–9060.

[194] Neal, J. F.; Zhao, W.; Grooms, A. J.; Smeltzer, M. A.; Shook, B. M.; Flood, A. H.; Allen, H. C. Interfacial Supramolecular Structures of Amphiphilic Receptors Drive Aqueous Phosphate Recognition. *J. Am. Chem. Soc.* **2019**, *141*, 7876–7886.

[195] Grooms, A. J.; Neal, J. F.; Ng, K. C.; Zhao, W.; Flood, A. H.; Allen, H. C. Thermodynamic Signatures of the Origin of Anti-Hofmeister Selectivity for Phosphate at Aqueous Interfaces. *J. Phys. Chem. A* **2020**, *124*, 5621–5630.

[196] Neal, J. F.; Saha, A.; Zerkle, M. M.; Zhao, W.; Rogers, M. M.; Flood, A. H.; Allen, H. C. Molecular Recognition and Hydration Energy Mismatch Combine To Inform Ion Binding Selectivity at Aqueous Interfaces. *J. Phys. Chem. A* **2020**, *124*, 10171–10180.

[197] Gericke, A.; Michailov, A. V.; Hühnerfuss, H. Polarized External Infrared Reflection-Absorption Spectrometry at the Air/Water Interface: Comparison of Experimental and Theoretical Results for Different Angles of Incidence. *Vib. Spectrosc.* **1993**, *4*, 335–348.

[198] Ropers, M.-H.; Meister, A.; Blume, A.; Ralet, M.-C. Pectin-Lipid Assembly at the Air–Water Interface: Effect of the Pectin Charge Distribution. *Biomacromolecules* **2008**, *9*, 1306–1312.

[199] Shen, Y. R. Optical Second Harmonic Generation at Interfaces. *Annu. Rev. Phys. Chem.* **1989**, *40*, 327–350.

[200] Eisenthal, K. B. Liquid Interfaces Probed by Second-Harmonic and Sum-Frequency Spectroscopy. *Chem. Rev.* **1996**, *96*, 1343–1360.

[201] Haywood, J.; Boucher, O. Estimates of the Direct and Indirect Radiative Forcing Due to Tropospheric Aerosols: A Review. *Rev. Geophys.* **2000**, *38*, 513–543.

[202] Alpert, P. A.; Aller, J. Y.; Knopf, D. A. Ice Nucleation from Aqueous NaCl Droplets with and without Marine Diatoms. *Atmos. Chem. Phys.* **2011**, *11*, 5539–5555.

[203] Knopf, D. A.; Alpert, P. A.; Wang, B.; Aller, J. Y. Stimulation of Ice Nucleation by Marine Diatoms. *Nat. Geosci.* **2011**, *4*, 88–90.

[204] Pummer, B. G. et al. Ice Nucleation by Water-Soluble Macromolecules. *Atmos. Chem. Phys.* **2015**, *15*, 4077–4091.

[205] Collins, D. B.; Bertram, T. H.; Sultana, C. M.; Lee, C.; Axson, J. L.; Prather, K. A. Phytoplankton Blooms Weakly Influence the Cloud Forming Ability of Sea Spray Aerosol. *Geophys. Res. Lett.* **2016**, *43*, 2016GL069922.

[206] Forestieri, S. D.; Staudt, S. M.; Kuborn, T. M.; Faber, K.; Ruehl, C. R.; Bertram, T. H.; Cappa, C. D. Establishing the Impact of Model Surfactants on Cloud Condensation Nuclei Activity of Sea Spray Aerosol Mimics. *Atmos. Chem. Phys.* **2018**, *18*, 10985–11005.

[207] Veghte, D. P.; Altaf, M. B.; Freedman, M. A. Size Dependence of the Structure of Organic Aerosol. *J. Am. Chem. Soc.* **2013**, *135*, 16046–16049.

[208] Altaf, M. B.; Zuend, A.; Freedman, M. A. Role of Nucleation Mechanism on the Size Dependent Morphology of Organic Aerosol. *Chem. Commun.* **2016**, *52*, 9220–9223.

[209] Losey, D. J.; Parker, R. G.; Freedman, M. A. pH Dependence of Liquid–Liquid Phase Separation in Organic Aerosol. *J. Phys. Chem. Lett.* **2016**, *7*, 3861–3865.

[210] Freedman, M. A. Phase Separation in Organic Aerosol. *Chem. Soc. Rev.* **2017**, *46*, 7694–7705.

[211] Altaf, M. B.; Dutcher, D. D.; Raymond, T. M.; Freedman, M. A. Effect of Particle Morphology on Cloud Condensation Nuclei Activity. *ACS Earth Space Chem.* **2018**, *2*, 634–639.

[212] Gavish, M.; Popovitz-Biro, R.; Lahav, M.; Leiserowitz, L. Ice Nucleation by Alcohols Arranged in Monolayers at the Surface of Water Drops. *Science* **1990**, *250*, 973–975.

[213] Ochshorn, E.; Cantrell, W. Towards Understanding Ice Nucleation by Long Chain Alcohols. *J. Chem. Phys.* **2006**, *124*, 054714.

[214] Knopf, D. A.; Forrester, S. M. Freezing of Water and Aqueous NaCl Droplets Coated by Organic Monolayers as a Function of Surfactant Properties and Water Activity. *J. Phys. Chem. A* **2011**, *115*, 5579–5591.

[215] Lupi, L.; Peters, B.; Molinero, V. Pre-Ordering of Interfacial Water in the Pathway of Heterogeneous Ice Nucleation Does Not Lead to a Two-Step Crystallization Mechanism. *J. Chem. Phys.* **2016**, *145*, 211910.

[216] Qiu, Y.; Odendahl, N.; Hudait, A.; Mason, R.; Bertram, A. K.; Paesani, F.; DeMott, P. J.; Molinero, V. Ice Nucleation Efficiency of Hydroxylated Organic Surfaces Is Controlled by Their Structural Fluctuations and Mismatch to Ice. *J. Am. Chem. Soc.* **2017**, *139*, 3052–3064.

[217] Takahama, S.; Liu, S.; Russell, L. M. Coatings and Clusters of Carboxylic Acids in Carbon-Containing Atmospheric Particles from Spectromicroscopy and Their Implications for Cloud-Nucleating and Optical Properties. *J. Geophys. Res.* **2010**, *115*.

[218] Estillore, A. D.; Morris, H. S.; Or, V. W.; Lee, H. D.; Alves, M. R.; Marciano, M. A.; Laskina, O.; Qin, Z.; Tivanski, A. V.; Grassian, V. H. Linking Hygroscopicity and the Surface Microstructure of Model Inorganic Salts, Simple and Complex Carbohydrates, and Authentic Sea Spray Aerosol Particles. *Phys. Chem. Chem. Phys.* **2017**, *19*, 21101–21111.

[219] Yoon, Y. J.; Ceburnis, D.; Cavalli, F.; Jourdan, O.; Putaud, J. P.; Facchini, M. C.; Decesari, S.; Fuzzi, S.; Sellegri, K.; Jennings, S. G.; O'Dowd, C. D. Seasonal Characteristics of the Physicochemical Properties of North Atlantic Marine Atmospheric Aerosols. *J. Geophys. Res.* **2007**, *112*, D04206.

[220] Gantt, B.; Meskhidze, N.; Facchini, M. C.; Rinaldi, M.; Ceburnis, D.; O'Dowd, C. D. Wind Speed Dependent Size-Resolved Parameterization for the Organic Mass Fraction of Sea Spray Aerosol. *Atmos. Chem. Phys.* **2011**, *11*, 8777–8790.

[221] Facchini, M. C.; Rinaldi, M.; Decesari, S.; Carbone, C.; Finessi, E.; Mircea, M.; Fuzzi, S.; Ceburnis, D.; Flanagan, R.; Nilsson, E. D.; de Leeuw, G.; Martino, M.; Woeltjen, J.; O'Dowd, C. D. Primary Submicron Marine Aerosol Dominated by Insoluble Organic Colloids and Aggregates. *Geophys. Res. Lett.* **2008**, *35*, L17814.

[222] Sciare, J.; Favez, O.; Sarda-Estève, R.; Oikonomou, K.; Cachier, H.; Kazan, V. Long-Term Observations of Carbonaceous Aerosols in the Austral Ocean Atmosphere: Evidence of a Biogenic Marine Organic Source. *J. Geophys. Res.* **2009**, *114*.

[223] Gantt, B.; Meskhidze, N. The Physical and Chemical Characteristics of Marine Primary Organic Aerosol: A Review. *Atmos. Chem. Phys.* **2013**, *13*, 3979–3996.

[224] Lee, C.; Sultana, C. M.; Collins, D. B.; Santander, M. V.; Axson, J. L.; Malfatti, F.; Cornwell, G. C.; Grandquist, J. R.; Deane, G. B.; Stokes, M. D.; Azam, F.; Grassian, V. H.; Prather, K. A. Advancing Model Systems for Fundamental Laboratory Studies of Sea Spray Aerosol Using the Microbial Loop. *J. Phys. Chem. A* **2015**, *119*, 8860–8870.

[225] Pham, D. Q.; O'Brien, R.; Fraund, M.; Bonanno, D.; Laskina, O.; Beall, C.; Moore, K. A.; Forestieri, S.; Wang, X.; Lee, C.; Sultana, C.; Grassian, V.;

Cappa, C. D.; Prather, K. A.; Moffet, R. C. Biological Impacts on Carbon Speciation and Morphology of Sea Spray Aerosol. *ACS Earth Space Chem.* **2017**, *1*, 551–561.

[226] Patterson, J. P.; Collins, D. B.; Michaud, J. M.; Axson, J. L.; Sultana, C. M.; Moser, T.; Dommer, A. C.; Conner, J.; Grassian, V. H.; Stokes, M. D.; Deane, G. B.; Evans, J. E.; Burkart, M. D.; Prather, K. A.; Gianneschi, N. C. Sea Spray Aerosol Structure and Composition Using Cryogenic Transmission Electron Microscopy. *ACS Cent. Sci.* **2016**, *2*, 40–47.

[227] Aller, J. Y.; Radway, J. C.; Kilthau, W. P.; Bothe, D. W.; Wilson, T. W.; Vaillancourt, R. D.; Quinn, P. K.; Coffman, D. J.; Murray, B. J.; Knopf, D. A. Size-Resolved Characterization of the Polysaccharidic and Proteinaceous Components of Sea Spray Aerosol. *Atmos. Environ.* **2017**, *154*, 331–347.

[228] Collins, D. B.; Zhao, D. F.; Ruppel, M. J.; Laskina, O.; Grandquist, J. R.; Modini, R. L.; Stokes, M. D.; Russell, L. M.; Bertram, T. H.; Grassian, V. H.; Deane, G. B.; Prather, K. A. Direct Aerosol Chemical Composition Measurements to Evaluate the Physicochemical Differences between Controlled Sea Spray Aerosol Generation Schemes. *Atmos. Meas. Tech.* **2014**, *7*, 3667–3683.

[229] Frossard, A. A.; Russell, L. M.; Burrows, S. M.; Elliott, S. M.; Bates, T. S.; Quinn, P. K. Sources and Composition of Submicron Organic Mass in Marine Aerosol Particles. *J. Geophys. Res. Atmos.* **2014**, *119*, 12,977–13,003.

[230] Wang, X.; Deane, G. B.; Moore, K. A.; Ryder, O. S.; Stokes, M. D.; Beall, C. M.; Collins, D. B.; Santander, M. V.; Burrows, S. M.; Sultana, C. M.; Prather, K. A. The Role of Jet and Film Drops in Controlling the Mixing State of Submicron Sea Spray Aerosol Particles. *Proc. Natl. Acad. Sci. U.S.A.* **2017**, *114*, 6978–6983.

[231] Donaldson, D. J.; Vaida, V. The Influence of Organic Films at the Air-Aqueous Boundary on Atmospheric Processes. *Chem. Rev.* **2006**, *106*, 1445–1461.

[232] Griffith, E. C.; Adams, E. M.; Allen, H. C.; Vaida, V. Hydrophobic Collapse of a Stearic Acid Film by Adsorbed L -Phenylalanine at the Air–Water Interface. *J. Phys. Chem. B* **2012**, *116*, 7849–7857.

[233] Joos, P. Effect of the pH on the Collapse Pressure of Fatty Acid Monolayers Evaluation of the Surface Dissociation Constant. *Bull. Sociétés Chim. Belg.* **1971**, *80*, 277–281.

[234] Pezron, E.; Claesson, P. M.; Berg, J. M.; Vollhardt, D. Stability of Arachidic Acid Monolayers on Aqueous Salt Solutions. *J. Colloid Interf. Sci.* **1990**, *138*, 245–254.

[235] Angelova, A.; Reiche, J.; Ionov, R.; Janietz, D.; Brehmer, L. Control of the Structure of Langmuir-Blodgett Films of a Discotic Liquid Crystalline Compound via the Subphase Composition and the Adjacent Molecular Environment. *Thin Solid Films* **1994**, *242*, 289–294.

[236] Angelova, A.; Vollhardt, D.; Ionov, R. 2D-3D Transformations of Amphiphilic Monolayers Influenced by Intermolecular Interactions: A Brewster Angle Microscopy Study. *J. Phys. Chem.* **1996**, *100*, 10710–10720.

[237] Minassian-Saraga, L. T. Recent Work on Spread Monolayers, Adsorption and Desorption. *J. Colloid Sci.* **1956**, *11*, 398–418.

[238] Patil, G. S.; Matthews, R. H.; Cornwell, D. G. Kinetics of the Processes of Desorption from Fatty Acid Monolayers. *J. Lipid Res.* **1973**, *14*, 26–31.

[239] Gershfeld, N. L. Physical Chemistry of Lipid Films at Fluid Interfaces. *Annu. Rev. Phys. Chem.* **1976**, *27*, 349–368.

[240] Gilman, J.; Eliason, T.; Fast, A.; Vaida, V. Selectivity and Stability of Organic Films at the Air–Aqueous Interface. *J. Colloid Interface Sci.* **2004**, *280*, 234–243.

[241] McLean, D. S.; Vercoe, D.; Stack, K. R.; Richardson, D. The Colloidal pKa of Lipophilic Extractives Commonly Found in Pinus Radiata. *Appita J.* **2005**, *58*, 362.

[242] Wellen, B. A.; Lach, E. A.; Allen, H. C. Surface pKa of Octanoic, Nonanoic, and Decanoic Fatty Acids at the Air–Water Interface: Applications to Atmospheric Aerosol Chemistry. *Phys. Chem. Chem. Phys.* **2017**,

[243] Dynarowicz-Łątka, P.; Kita, K. Molecular Interaction in Mixed Monolayers at the Air/Water Interface. *Adv. Colloid Interfac.* **1999**, *79*, 1–17.

[244] Rodríguez Patino, J. M.; Rodríguez Niño, M. Interfacial Characteristics of Food Emulsifiers (Proteins and Lipids) at the Air-Water Interface. *Colloids Surf. B Biointerfaces* **1999**, *15*, 235–252.

[245] Brzozowska, A. M.; Mugele, F.; Duits, M. H. G. Stability and Interactions in Mixed Monolayers of Fatty Acid Derivatives on Artificial Sea Water. *Colloid Surface A* **2013**, *433*, 200–211.

[246] Khattari, Z.; Sayyed, M. I.; Qashou, S. I.; Fasfous, I.; Al-Abdullah, T.; Maghrabi, M. Interfacial Behavior of Myristic Acid in Mixtures with DMPC and Cholesterol. *Chem. Phys.* **2017**, *490*, 106–114.

[247] McFate, C.; Ward, D.; Olmsted, J. Organized Collapse of Fatty Acid Monolayers. *Langmuir* **1993**, *9*, 1036–1039.

[248] Kundu, S.; Datta, A.; Hazra, S. Effect of Metal Ions on Monolayer Collapses. *Langmuir* **2005**, *21*, 5894–5900.

[249] Baoukina, S.; Monticelli, L.; Risselada, H. J.; Marrink, S. J.; Tieleman, D. P. The Molecular Mechanism of Lipid Monolayer Collapse. *Proc. Natl. Acad. Sci. U.S.A.* **2008**, *105*, 10803–10808.

[250] Fridlind, A. M.; Jacobson, M. Z. A Study of Gas-Aerosol Equilibrium and Aerosol pH in the Remote Marine Boundary Layer during the First Aerosol Characterization Experiment (ACE 1). *J. Geophys. Res. Atmos.* **2000**, *105*, 17325–17340.

[251] Huang, Z.; Hua, W.; Verreault, D.; Allen, H. C. Influence of Salt Purity on Na^+ and Palmitic Acid Interactions. *J. Phys. Chem. A* **2013**, *117*, 13412–13418.

[252] Adams, E. M.; Allen, H. C. Palmitic Acid on Salt Subphases and in Mixed Monolayers of Cerebrosides: Application to Atmospheric Aerosol Chemistry. *Atmosphere* **2013**, *4*, 315–336.

[253] Schneider, C. A.; Rasband, W. S.; Eliceiri, K. W. NIH Image to ImageJ: 25 Years of Image Analysis. *Nat. Methods* **2012**, *9*, 671–675.

[254] Millero, F. J.; Feistel, R.; Wright, D. G.; McDougall, T. J. The Composition of Standard Seawater and the Definition of the Reference-Composition Salinity Scale. *Deep-Sea Res. Pt. I* **2008**, *55*, 50–72.

[255] Durbin, M. K.; Shih, M. C.; Malik, A.; Zschack, P.; Dutta, P. Isotherm and X-Ray Diffraction Studies of Mixed Monolayers. *Colloid Surface A* **1995**, *102*, 173–179.

[256] Nutting, G. C.; Harkins, W. D. Pressure–Area Relations of Fatty Acid and Alcohol Monolayers. *J. Am. Chem. Soc.* **1939**, *61*, 1180–1187.

[257] Fischer, A.; Sackmann, E. Electron Microscopy and Electron Diffraction Study of Coexisting Phases of Pure and Mixed Monolayers Transferred onto Solid Substrates. *J. Colloid Interf. Sci.* **1986**, *112*, 1–14.

[258] Guyot-Sionnest, P.; Hunt, J. H.; Shen, Y. R. Sum-Frequency Vibrational Spectroscopy of a Langmuir Film: Study of Molecular Orientation of a Two-Dimensional System. *Phys. Rev. Lett.* **1987**, *59*, 1597–1600.

[259] Baoukina, S.; Rozmanov, D.; Mendez-Villuendas, E.; Tieleman, D. P. The Mechanism of Collapse of Heterogeneous Lipid Monolayers. *Biophys. Chem.* **2014**, *107*, 1136–1145.

[260] Gopal, A.; Lee, K. Y. C. Morphology and Collapse Transitions in Binary Phospholipid Monolayers. *J. Phys. Chem. B* **2001**, *105*, 10348–10354.

[261] Ding, J.; Takamoto, D. Y.; von Nahmen, A.; Lipp, M. M.; Lee, K. Y. C.; Waring, A. J.; Zasadzinski, J. A. Effects of Lung Surfactant Proteins, SP-B and SP-C, and Palmitic Acid on Monolayer Stability. *Biophys. J.* **2001**, *80*, 2262–2272.

[262] Takamoto, D. Y.; Lipp, M. M.; von Nahmen, A.; Lee, K. Y. C.; Waring, A. J.; Zasadzinski, J. A. Interaction of Lung Surfactant Proteins with Anionic Phospholipids. *Biophys. J.* **2001**, *81*, 153–169.

[263] Ridsdale, R.; Palaniyar, N.; Possmayer, F.; Harauz, G. Formation of Folds and Vesicles by Dipalmitoylphosphatidylcholine Monolayers Spread in Excess. *J. Membrane Biol.* **2001**, *180*, 21–32.

[264] Pallas, N. R.; Pethica, B. A. Liquid-Expanded to Liquid-Condensed Transition in Lipid Monolayers at the Air/Water Interface. *Langmuir* **1985**, *1*, 509–513.

[265] Ruckenstein, E. On the Nature of The Liquid Expanded/Liquid Condensed Phase Transition in Monolayers of Polar Molecules. *J. Colloid Interf. Sci.* **1997**, *196*, 313–315.

[266] Tang, C. Y.; Allen, H. C. Ionic Binding of Na^+ versus K^+ to the Carboxylic Acid Headgroup of Palmitic Acid Monolayers Studied by Vibrational Sum Frequency Generation Spectroscopy. *J. Phys. Chem. A* **2009**, *113*, 7383–7393.

[267] Muller, E. A.; Gray, T. P.; Zhou, Z.; Cheng, X.; Khatib, O.; Bechtel, H. A.; Raschke, M. B. Vibrational Exciton Nanoimaging of Phases and Domains in Porphyrin Nanocrystals. *Proc. Natl. Acad. Sci. U.S.A.* **2020**, *117*, 7030–7037.

[268] Signorell, R. Verification of the Vibrational Exciton Approach for CO2 and N2O Nanoparticles. *J. Chem. Phys.* **2003**, *118*, 2707–2715.

[269] Torii, H. Extent of Delocalization of Vibrational Modes in Liquids as a Result of Competition between Diagonal Disorder and Off-Diagonal Coupling. *J. Phys. Chem. A* **2004**, *108*, 2103–2107.

[270] Krummel, A. T.; Zanni, M. T. DNA Vibrational Coupling Revealed with Two-Dimensional Infrared Spectroscopy: Insight into Why Vibrational Spectroscopy Is Sensitive to DNA Structure. *J. Phys. Chem. B* **2006**, *110*, 13991–14000.

[271] Auer, B. M.; Skinner, J. L. Dynamical Effects in Line Shapes for Coupled Chromophores: Time-Averaging Approximation. *J. Chem. Phys.* **2007**, *127*, 104105.

[272] Auer, B. M.; Skinner, J. L. IR and Raman Spectra of Liquid Water: Theory and Interpretation. *J. Chem. Phys.* **2008**, *128*, 224511.

[273] Krummel, A. T.; Zanni, M. T. Evidence for Coupling between Nitrile Groups Using DNA Templates: A Promising New Method for Monitoring Structures with Infrared Spectroscopy. *J. Phys. Chem. B* **2008**, *112*, 1336–1338.

[274] Torii, H. Intra- and Intermolecular Charge Fluxes Induced by the OH Stretching Mode of Water and Their Effects on the Infrared Intensities and Intermolecular Vibrational Coupling. *J. Phys. Chem. B* **2010**, *114*, 13403–13409.

[275] Yang, M.; Skinner, J. L. Signatures of Coherent Vibrational Energy Transfer in IR and Raman Line Shapes for Liquid Water. *Phys. Chem. Chem. Phys.* **2010**, *12*, 982–991.

[276] Bredenbeck, J.; Ghosh, A.; Smits, M.; Bonn, M. Ultrafast Two Dimensional-Infrared Spectroscopy of a Molecular Monolayer. *J. Am. Chem. Soc.* **2008**, *130*, 2152–2153.

[277] Bredenbeck, J.; Ghosh, A.; Nienhuys, H.-K.; Bonn, M. Interface-Specific Ultrafast Two-Dimensional Vibrational Spectroscopy. *Acc. Chem. Res.* **2009**, *42*, 1332–1342.

[278] Lackner, M.; Hille, M.; Hasselbrink, E. Vibrational Energy Redistribution between CH Stretching Modes in Alkyl Chain Monolayers Revealed by Time-Resolved Two-Color Pump–Probe Sum Frequency Spectroscopy. *J. Phys. Chem. Lett.* **2020**, *11*, 108–112.

[279] Kawai, T.; Kamio, H.; Kondo, T.; Kon-No, K. Effects of Concentration and Temperature on SDS Monolayers at the Air-Solution Interface Studied by Infrared External Reflection Spectroscopy. *J. Phys. Chem. B* **2005**, *109*, 4497–4500.

[280] Rao, Y.; Li, X.; Lei, X.; Jockusch, S.; George, M. W.; Turro, N. J.; Eisenthal, K. B. Observations of Interfacial Population and Organization of Surfactants with Sum Frequency Generation and Surface Tension. *J. Phys. Chem. C* **2011**, *115*, 12064–12067.

[281] Wang, H.-F.; Gan, W.; Lu, R.; Rao, Y.; Wu, B.-H. Quantitative Spectral and Orientational Analysis in Surface Sum Frequency Generation Vibrational Spectroscopy (SFG-VS). *Int. Rev. Phys. Chem.* **2005**, *24*, 191–256.

[282] Buontempo, J. T.; Rice, S. A. Infrared External Reflection Spectroscopic Studies of Phase Transitions in Langmuir Monolayers of Heneicosanol. *J. Chem. Phys.* **1993**, *98*, 5835–5846.

[283] Tian, K.; Zhang, B.; Ye, S.; Luo, Y. Intermolecular Interactions at the Interface Quantified by Surface-Sensitive Second-Order Fermi Resonant Signals. *J. Phys. Chem. C* **2015**, *119*, 16587–16595.

[284] Hua, W.; Verreault, D.; Adams, E. M.; Huang, Z.; Allen, H. C. Impact of Salt Purity on Interfacial Water Organization Revealed by Conventional and Heterodyne-Detected Vibrational Sum Frequency Generation Spectroscopy. *J. Phys. Chem. C* **2013**, *117*, 19577–19585.

[285] Carter-Fenk, K. A.; Carter-Fenk, K.; Fiamingo, M. E.; Allen, H.; Herbert, J. M. Infrared Hide-and-Seek: Vibrational Excitons Conceal Surfactants at the Air/Water Interface. **2020**,

[286] Bussi, G.; Donadio, D.; Parrinello, M. Canonical Sampling through Velocity Rescaling. *J. Chem. Phys.* **2007**, *126*, 014101.

[287] Tuckerman, M.; Berne, B. J.; Martyna, G. J. Reversible Multiple Time Scale Molecular Dynamics. *J. Chem. Phys.* **1992**, *97*, 1990–2001.

[288] Lagardère, L.; Jolly, L.-H.; Lipparini, F.; Aviat, F.; Stamm, B.; Jing, Z. F.; Harger, M.; Torabifard, H.; Cisneros, G. A.; Schnieders, M. J.; Gresh, N.; Maday, Y.; Ren, P. Y.; Ponder, J. W.; Piquemal, J.-P. Tinker-HP: A Massively Parallel Molecular Dynamics Package for Multiscale Simulations of Large Complex Systems with Advanced Point Dipole Polarizable Force Fields. *Chem. Sci.* **2018**, *9*, 956–972.

[289] Lin, C. Y.; George, M. W.; Gill, P. M. W. EDF2: A Density Functional for Predicting Molecular Vibrational Frequencies. *Aust. J. Chem.* **2004**, *57*, 365.

[290] Shao, Y. et al. Advances in Molecular Quantum Chemistry Contained in the Q-Chem 4 Program Package. *Mol. Phys.* **2015**, *113*, 184–215.

[291] Merrick, J. P.; Moran, D.; Radom, L. An Evaluation of Harmonic Vibrational Frequency Scale Factors. *J. Phys. Chem. A* **2007**, *111*, 11683–11700.

[292] Vierke, L.; Berger, U.; Cousins, I. T. Estimation of the Acid Dissociation Constant of Perfluoroalkyl Carboxylic Acids through an Experimental Investigation of Their Water-to-Air Transport. *Environ. Sci. Technol.* **2013**, *47*, 11032–11039.

[293] Johansson, J. H.; Yan, H.; Berger, U.; Cousins, I. T. Water-to-Air Transfer of Branched and Linear PFOA: Influence of pH, Concentration and Water Type. *Emerging Contaminants* **2017**, *3*, 46–53.

[294] Kalra, A.; Tugcu, N.; Cramer, S. M.; Garde, S. Salting-In and Salting-Out of Hydrophobic Solutes in Aqueous Salt Solutions. *J. Phys. Chem. B* **2001**, *105*, 6380–6386.

[295] Vargaftik, N. B.; Volkov, B. N.; Voljak, L. D. International Tables of the Surface Tension of Water. *J. Phys. Chem. Ref. Data* **1983**, *12*, 817–820.

[296] Shinoda, K.; Nakayama, H. Separate Determinations of the Surface Excesses of Surface-Active Ions and of Gegenions at the Air-Solution Interface. *J. Coll. Sci.* **1963**, *18*, 705–712.

[297] Shinoda, K.; Hato, M.; Hayashi, T. Physicochemical Properties of Aqueous Solutions of Fluorinated Surfactants. *J. Phys. Chem.* **1972**, *76*, 909–914.

[298] Downes, N.; Ottewill, G.; Ottewill, R. An Investigation of the Behaviour of Ammonium Perfluoro-Octanoate at the Air/Water Interface in the Absence and Presence of Salts. *Colloid Surface A* **1995**, *102*, 203–211.

[299] Brusseau, M. L.; Van Glubt, S. The Influence of Surfactant and Solution Composition on PFAS Adsorption at Fluid-Fluid Interfaces. *Water Res.* **2019**, *161*, 17–26.

[300] Nakahara, H.; Nakamura, S.; Kawasaki, H.; Shibata, O. Properties of Two-Component Langmuir Monolayer of Single Chain Perfluorinated Carboxylic Acids with Dipalmitoylphosphatidylcholine (DPPC). *Colloid Surface B* **2005**, *41*, 285–298.

[301] Shimoaka, T.; Tanaka, Y.; Shioya, N.; Morita, K.; Sonoyama, M.; Amii, H.; Takagi, T.; Kanamori, T.; Hasegawa, T. Surface Properties of a Single Perfluoroalkyl Group on Water Surfaces Studied by Surface Potential Measurements. *J. Colloid Interf. Sci.* **2016**, *483*, 353–359.

[302] Downing, H. D.; Williams, D. Optical Constants of Water in the Infrared. *J. Geophys. Res.* **1975**, *80*, 1656–1661.

[303] Ponder, J. W.; Wu, C.; Ren, P.; Pande, V. S.; Chodera, J. D.; Schnieders, M. J.; Haque, I.; Mobley, D. L.; Lambrecht, D. S.; DiStasio, R. A.; Head-Gordon, M.; Clark, G. N. I.; Johnson, M. E.; Head-Gordon, T. Current Status of the AMOEBA Polarizable Force Field. *J. Phys. Chem. B* **2010**, *114*, 2549–2564.

[304] Persson, B. N. J.; Ryberg, R. Vibrational Interaction between Molecules Adsorbed on a Metal Surface: The Dipole-Dipole Interaction. *Phys. Rev. B* **1981**, *24*, 6954–6970.

[305] Tyrode, E.; Corkery, R. Charging of Carboxylic Acid Monolayers with Monovalent Ions at Low Ionic Strengths: Molecular Insight Revealed by Vibrational Sum Frequency Spectroscopy. *J. Phys. Chem. C* **2018**, *122*, 28775–28786.

[306] Sthoer, A.; Tyrode, E. Interactions of Na+ Cations with a Highly Charged Fatty Acid Langmuir Monolayer: Molecular Description of the Phase Transition. *J. Phys. Chem. C* **2019**, *123*, 23037–23048.

[307] Fainerman, V. B.; Vollhardt, D.; Johann, R. Arachidic Acid Monolayers at High pH of the Aqueous Subphase: Studies of Counterion Bonding. *Langmuir* **2000**, *16*, 7731–7736.

[308] Johann, R.; Vollhardt, D. Texture Features of Long-Chain Fatty Acid Monolayers at High pH of the Aqueous Subphase. *Mat. Sci. Eng. C* **1999**, *8-9*, 35–42.

[309] Javanainen, M.; Hua, W.; Tichacek, O.; Delcroix, P.; Cwiklik, L.; Allen, H. C. Structural Effects of Cation Binding to DPPC Monolayers. *Langmuir* **2020**, *36*, 15258–15269.

[310] Gao, Q.; Leck, C.; Rauschenberg, C.; Matrai, P. A. On the Chemical Dynamics of Extracellular Polysaccharides in the High Arctic Surface Microlayer. *Ocean Sci.* **2012**, *8*, 401–418.

[311] Thornton, D. C. O.; Brooks, S. D.; Chen, J. Protein and Carbohydrate Exopolymer Particles in the Sea Surface Microlayer (SML). *Front. Mar. Sci.* **2016**, *3*, 1–14.

[312] Hasenecz, E. S.; Jayarathne, T.; Pendergraft, M. A.; Santander, M. V.; Mayer, K. J.; Sauer, J.; Lee, C.; Gibson, W. S.; Kruse, S. M.; Malfatti, F.; Prather, K. A.; Stone, E. A. Marine Bacteria Affect Saccharide Enrichment in Sea Spray Aerosol during a Phytoplankton Bloom. *ACS Earth Space Chem.* **2020**, *4*, 1638–1649.

[313] Link, K. A.; Hsieh, C.-Y.; Tuladhar, A.; Chase, Z.; Wang, Z.; Wang, H.; Walker, R. A. Vibrational Studies of Saccharide-Induced Lipid Film Reorganization at Aqueous/Air Interfaces. *Chem. Phys.* **2018**, *512*, 104–110.

[314] Link, K. A.; Spurzem, G. N.; Tuladhar, A.; Chase, Z.; Wang, Z.; Wang, H.; Walker, R. A. Organic Enrichment at Aqueous Interfaces: Cooperative Adsorption of Glucuronic Acid to DPPC Monolayers Studied with Vibrational Sum Frequency Generation. *J. Phys. Chem. A* **2019**, *123*, 5621–5632.

[315] Link, K. A.; Spurzem, G. N.; Tuladhar, A.; Chase, Z.; Wang, Z.; Wang, H.; Walker, R. A. Cooperative Adsorption of Trehalose to DPPC Monolayers at the Water–Air Interface Studied with Vibrational Sum Frequency Generation. *J. Phys. Chem. B* **2019**, *123*, 8931–8938.

[316] Leck, C.; Bigg, E. K. Biogenic Particles in the Surface Microlayer and Overlaying Atmosphere in the Central Arctic Ocean during Summer. *Tellus B* **2005**, *57*, 305–316.

[317] Leck, C.; Gao, Q.; Mashayekhy Rad, F.; Nilsson, U. Size-Resolved Atmospheric Particulate Polysaccharides in the High Summer Arctic. *Atmos. Chem. Phys.* **2013**, *13*, 12573–12588.

[318] Leck, C.; Svensson, E. Importance of Aerosol Composition and Mixing State for Cloud Droplet Activation over the Arctic Pack Ice in Summer. *Atmos. Chem. Phys.* **2015**, *15*, 2545–2568.

[319] Pummer, B. G.; Bauer, H.; Bernardi, J.; Bleicher, S.; Grothe, H. Suspendable Macromolecules Are Responsible for Ice Nucleation Activity of Birch and Conifer Pollen. *Atmos. Chem. Phys.* **2012**, *12*, 2541–2550.

[320] Hiranuma, N.; Möhler, O.; Yamashita, K.; Tajiri, T.; Saito, A.; Kiselev, A.; Hoffmann, N.; Hoose, C.; Jantsch, E.; Koop, T.; Murakami, M. Ice Nucleation by Cellulose and Its Potential Contribution to Ice Formation in Clouds. *Nat. Geosci.* **2015**, *8*, 273–277.

[321] Dreischmeier, K.; Budke, C.; Wiehemeier, L.; Kottke, T.; Koop, T. Boreal Pollen Contain Ice-Nucleating as Well as Ice-Binding 'Antifreeze' Polysaccharides. *Sci. Rep.* **2017**, *7*, 41890.

[322] Hiranuma, N. et al. A Comprehensive Characterization of Ice Nucleation by Three Different Types of Cellulose Particles Immersed in Water. *Atmos. Chem. Phys.* **2019**, *19*, 4823–4849.

[323] Wolf, M. J.; Coe, A.; Dove, L. A.; Zawadowicz, M. A.; Dooley, K.; Biller, S. J.; Zhang, Y.; Chisholm, S. W.; Cziczo, D. J. Investigating the Heterogeneous Ice Nucleation of Sea Spray Aerosols Using Prochlorococcus as a Model Source of Marine Organic Matter. *Environ. Sci. Technol.* **2019**, *53*, 1139–1149.

[324] Zeppenfeld, S.; van Pinxteren, M.; Hartmann, M.; Bracher, A.; Stratmann, F.; Herrmann, H. Glucose as a Potential Chemical Marker for Ice Nucleating Activity in Arctic Seawater and Melt Pond Samples. *Environ. Sci. Technol.* **2019**, *53*, 8747–8756.

[325] Hasenecz, E. S.; Kaluarachchi, C. P.; Lee, H. D.; Tivanski, A. V.; Stone, E. A. Saccharide Transfer to Sea Spray Aerosol Enhanced by Surface Activity, Calcium, and Protein Interactions. *ACS Earth Space Chem.* **2019**, *3*, 2539–2548.

[326] Gorin, P. a. J.; Spencer, J. F. T. Exocellular Alginic Acid from Azotobacter Vinelandii. *Can. J. Chem.* **1966**, *44*, 993–998.

[327] Linker, A.; Jones, R. S. A New Polysaccharide Resembling Alginic Acid Isolated from Pseudomonads. *J. Biol. Chem.* **1966**, *241*, 3845–3851.

[328] Haug, A.; Larsen, B.; Fykse, O.; Block-Bolten, A.; Toguri, J. M.; Flood, H. Quantitative Determination of the Uronic Acid Composition of Alginates. *Acta Chem. Scand.* **1962**, *16*, 1908–1918.

[329] Haug, A.; Larsen, B.; Smidsrød, O.; Smidsrød, O.; Eriksson, G.; Blinc, R.; Paušak, S.; Ehrenberg, L.; Dumanović, J. Studies on the Sequence of Uronic Acid Residues in Alginic Acid. *Acta Chem. Scand.* **1967**, *21*, 691–704.

[330] Haug, A.; Myklestad, S.; Larsen, B.; Smidsrød, O.; Eriksson, G.; Blinc, R.; Paušak, S.; Ehrenberg, L.; Dumanović, J. Correlation between Chemical Structure and Physical Properties of Alginates. *Acta Chem. Scand.* **1967**, *21*, 768–778.

[331] Grasdalen, H.; Larsen, B.; Smidsrød, O. A p.m.r. Study of the Composition and Sequence of Uronate Residues in Alginates. *Carbohyd. Res.* **1979**, *68*, 23–31.

[332] Johnson, F. A.; Craig, D. Q. M.; Mercer, A. D. Characterization of the Block Structure and Molecular Weight of Sodium Alginates. *J. Pharm. Pharmacol.* **1997**, *49*, 639–643.

[333] Lee, K. Y.; Mooney, D. J. Alginate: Properties and Biomedical Applications. *Prog. Polym. Sci.* **2012**, *37*, 106–126.

[334] Morris, E. R.; Rees, D. A.; Thom, D.; Boyd, J. Chiroptical and Stoichiometric Evidence of a Specific, Primary Dimerisation Process in Alginate Gelation. *Carbohyd. Res.* **1978**, *66*, 145–154.

[335] Fang, Y.; Al-Assaf, S.; Phillips, G. O.; Nishinari, K.; Funami, T.; Williams, P. A.; Li, L. Multiple Steps and Critical Behaviors of the Binding of Calcium to Alginate. *J. Phys. Chem. B* **2007**, *111*, 2456–2462.

[336] Hecht, H.; Srebnik, S. Structural Characterization of Sodium Alginate and Calcium Alginate. *Biomacromolecules* **2016**, *17*, 2160–2167.

[337] Kohn, R. Ion Binding on Polyuronates - Alginate and Pectin. *Pure Appl. Chem.* **1975**, *42*, 371–397.

[338] Malovíková, A.; Rinaudo, M.; Milas, M. Comparative Interactions of Magnesium and Calcium Counterions with Polygalacturonic Acid. *Biopolymers* **1994**, *34*, 1059–1064.

[339] Donati, I.; Cesàro, A.; Paoletti, S. Specific Interactions versus Counterion Condensation. 1. Nongelling Ions/Polyuronate Systems. *Biomacromolecules* **2006**, *7*, 281–287.

[340] Donati, I.; Asaro, F.; Paoletti, S. Experimental Evidence of Counterion Affinity in Alginates: The Case of Nongelling Ion Mg^{2+}. *J. Phys. Chem. B* **2009**, *113*, 12877–12886.

[341] Topuz, F.; Henke, A.; Richtering, W.; Groll, J. Magnesium Ions and Alginate Do Form Hydrogels: A Rheological Study. *Soft Matter* **2012**, *8*, 4877.

[342] Huynh, U. T. D.; Lerbret, A.; Neiers, F.; Chambin, O.; Assifaoui, A. Binding of Divalent Cations to Polygalacturonate: A Mechanism Driven by the Hydration Water. *J. Phys. Chem. B* **2016**, *120*, 1021–1032.

[343] Li, X.; Leck, C.; Sun, L.; Hede, T.; Tu, Y.; Ågren, H. Cross-Linked Polysaccharide Assemblies in Marine Gels: An Atomistic Simulation. *J. Phys. Chem. Lett.* **2013**, *4*, 2637–2642.

[344] Sun, L.; Li, X.; Hede, T.; Tu, Y.; Leck, C.; Ågren, H. Molecular Dynamics Simulations Reveal the Assembly Mechanism of Polysaccharides in Marine Aerosols. *Phys. Chem. Chem. Phys.* **2014**, *16*, 25935–25941.

[345] Degen, P.; Paulus, M.; Zwar, E.; Jakobi, V.; Dogan, S.; Tolan, M.; Rehage, H. Surfactant-Mediated Formation of Alginate Layers at the Water-Air Interface. *Surf. Interface Anal.* **2019**, *51*, 1051–1058.

[346] Pavinatto, F. J.; Pavinatto, A.; Caseli, L.; dos Santos, D. S.; Nobre, T. M.; Zaniquelli, M. E. D.; Oliveira, O. N. Interaction of Chitosan with Cell Membrane Models at the Air-Water Interface. *Biomacromolecules* **2007**, *8*, 1633–1640.

[347] Wydro, P.; Krajewska, B.; Hąc-Wydro, K. Chitosan as a Lipid Binder: A Langmuir Monolayer Study of Chitosan-Lipid Interactions. *Biomacromolecules* **2007**, *8*, 2611–2617.

[348] Krajewska, B.; Wydro, P.; Jańczyk, A. Probing the Modes of Antibacterial Activity of Chitosan. Effects of pH and Molecular Weight on Chitosan Interactions with Membrane Lipids in Langmuir Films. *Biomacromolecules* **2011**, *12*, 4144–4152.

[349] Krajewska, B.; Wydro, P.; Kyzioł, A. Chitosan as a Subphase Disturbant of Membrane Lipid Monolayers. The Effect of Temperature at Varying pH: I. DPPG. *Colloid Surface A* **2013**, *434*, 349–358.

[350] Pavinatto, A.; Souza, A. L.; Delezuk, J. A. M.; Pavinatto, F. J.; Campana-Filho, S. P.; Oliveira, O. N. Interaction of O-Acylated Chitosans with Biomembrane Models: Probing the Effects from Hydrophobic Interactions and Hydrogen Bonding. *Colloid Surface B* **2014**, *114*, 53–59.

[351] Pavinatto, A.; Delezuk, J. A. M.; Souza, A. L.; Pavinatto, F. J.; Volpati, D.; Miranda, P. B.; Campana-Filho, S. P.; Oliveira Jr., O. N. Experimental Evidence for the Mode of Action Based on Electrostatic and Hydrophobic Forces to Explain Interaction between Chitosans and Phospholipid Langmuir Monolayers. *Colloid Surface B* **2016**, *145*, 201–207.

[352] Parra-Barraza, H.; Burboa, M. G.; Sánchez-Vázquez, M.; Juárez, J.; Goycoolea, F. M.; Valdez, M. A. Chitosan-Cholesterol and Chitosan-Stearic Acid Interactions at the Air-Water Interface. *Biomacromolecules* **2005**, *6*, 2416–2426.

[353] de Meijere, K.; Brezesinski, G.; Zschörnig, O.; Arnold, K.; Möhwald, H. Structure Studies of a Phospholipid Monolayer Coupled to Dextran Sulfate. *Physica B* **1998**, *248*, 269–273.

[354] Huster, D.; Arnold, K. Ca^{2+}-Mediated Interaction between Dextran Sulfate and Dimyristoyl-*Sn*-Glycero-3-Phosphocholine Surfaces Studied by ^2H Nuclear Magnetic Resonance. *Biophys. J.* **1998**, *75*, 909–916.

[355] Huster, D.; Paasche, G.; Dietrich, U.; Zschörnig, O.; Gutberlet, T.; Gawrisch, K.; Arnold, K. Investigation of Phospholipid Area Compression Induced by Calcium-Mediated Dextran Sulfate Interaction. *Biophys. J.* **1999**, *77*, 879–887.

[356] Miranda, P. B.; Du, Q.; Shen, Y. R. Interaction of Water with a Fatty Acid Langmuir Film. *Chem. Phys. Lett.* **1998**, *286*, 1–8.

[357] Kanicky, J. R.; Shah, D. O. Effect of Degree, Type, and Position of Unsaturation on the pKa of Long-Chain Fatty Acids. *J. Colloid Interf. Sci.* **2002**, *256*, 201–207.

[358] Bu, H.; Kjøniksen, A.-L.; Elgsaeter, A.; Nyström, B. Interaction of Unmodified and Hydrophobically Modified Alginate with Sodium Dodecyl Sulfate in Dilute Aqueous Solution: Calorimetric, Rheological, and Turbidity Studies. *Colloid Surface A* **2006**, *278*, 166–174.

[359] Marion, G. M.; Millero, F. J.; Camões, M. F.; Spitzer, P.; Feistel, R.; Chen, C. T. A. pH of Seawater. *Mar. Chem.* **2011**, *126*, 89–96.

[360] Denton, J. K.; Kelleher, P. J.; Johnson, M. A.; Baer, M. D.; Kathmann, S. M.; Mundy, C. J.; Rudd, B. A. W.; Allen, H. C.; Choi, T. H.; Jordan, K. D. Molecular-Level Origin of the Carboxylate Head Group Response to Divalent Metal Ion Complexation at the Air–Water Interface. *Proc. Natl. Acad. Sci. U.S.A.* **2019**, *116*, 14874–14880.

[361] Aida, T. M.; Yamagata, T.; Watanabe, M.; Smith, R. L. Depolymerization of Sodium Alginate under Hydrothermal Conditions. *Carbohyd. Polym.* **2010**, *80*, 296–302.

[362] Lu, J.; Yang, H.; Hao, J.; Wu, C.; Liu, L.; Xu, N.; Linhardt, R. J.; Zhang, Z. Impact of Hydrolysis Conditions on the Detection of Mannuronic to Guluronic Acid Ratio in Alginate and Its Derivatives. *Carbohyd. Polym.* **2015**, *122*, 180–188.

[363] Tang, C. Y.; Huang, Z.; Allen, H. C. Interfacial Water Structure and Effects of Mg^{2+} and Ca^{2+} Binding to the COOH Headgroup of a Palmitic Acid Monolayer Studied by Sum Frequency Spectroscopy. *J. Phys. Chem. B* **2011**, *115*, 34–40.

[364] Balzerowski, P.; Meister, K.; Versluis, J.; Bakker, H. J. Heterodyne-Detected Sum Frequency Generation Spectroscopy of Polyacrylic Acid at the Air/Water-Interface. *Phys. Chem. Chem. Phys.* **2016**, *18*, 2481–2487.

[365] Tanaka, N.; Kitano, H.; Ise, N. Raman Spectroscopic Study of Hydrogen Bonding in Aqueous Carboxylic Acid Solutions. 3. Polyacrylic Acid. *Macromolecules* **1991**, *24*, 3017–3019.

[366] Gragson, D. E.; Richmond, G. L. Investigations of the Structure and Hydrogen Bonding of Water Molecules at Liquid Surfaces by Vibrational Sum Frequency Spectroscopy. *J. Phys. Chem. B* **1998**, *102*, 3847–3861.

[367] Allen, H. C.; Casillas-Ituarte, N. N.; Sierra-Hernández, M. R.; Chen, X.; Tang, C. Y. Shedding Light on Water Structure at Air–Aqueous Interfaces: Ions, Lipids, and Hydration. *Phys. Chem. Chem. Phys.* **2009**, *11*, 5538–5549.

[368] Kundu, S.; Langevin, D. Fatty Acid Monolayer Dissociation and Collapse: Effect of pH and Cations. *Colloid Surface A* **2008**, *325*, 81–85.

[369] Tang, C. Y.; Huang, Z.; Allen, H. C. Binding of Mg^{2+} and Ca^{2+} to Palmitic Acid and Deprotonation of the COOH Headgroup Studied by Vibrational Sum Frequency Generation Spectroscopy. *J. Phys. Chem. B* **2010**, *114*, 17068–17076.

[370] Atomic Masses and Isotopic Abundances. *CRC Handbook of Chemistry and Physics*

Appendix A

Perfluorooctanoic Acid C–F Peak Assignments

A.1 Perfluorooctanoic Acid C–F Peak Assignments

Vibrational mode peak assignments of deprotonated perfluorooctanoic acid (perfluorooctanoate, PFO) were performed via geometry optimization and harmonic vibrational frequency analysis using Q-Chem v. 5.3.1.[290] Density functional theory (DFT) at the EDF2/6-31G(d) level of theory was used,[289] and a scaling factor of 0.9805 was applied to the harmonic frequencies.[291] Vibrational frequencies, intensities, and peak assignments corresponding to the C–F vibrational modes are tabulated in Table A.1.

Table A.1: Peak Assignments Corresponding to the C–F Vibrational Modes of PFO.

Wavenumber (cm^{-1})	**Intensity (km/mol)**	**Vibrational Mode Assignments**
1095.72	36.734	CF_2 and CF_3 Wagging
1104.99	70.264	CF_2 Asymmetric Stretching
1125.64	23.161	CF_2 Symmetric Stretching and Wagging
1130.98	61.766	CF_2 Symmetric Stretching and Wagging, CF_3 Wagging
1153.29	194.923	CF_2 Symmetric and Asymmetric Stretching
1173.79	15.306	CF_2 Asymmetric Stretching
1177.81	77.910	CF_2 Asymmetric Stretching
1188.97	27.910	CF_2 and CF_3 Asymmetric Stretching
1197.64	93.936	CF_2 Asymmetric Stretching
1206.15	94.093	CF_3 Asymmetric Stretching and C–C Stretching
1214.10	245.849	CF_2 Asymmetric Stretching CF_3 Asymmetric Stretching C–C Stretching
1219.89	243.765	CF_2 and CF_3 Asymmetric Stretching
1245.74	59.383	CF_3 Asymmetric Stretching and C–C Stretching
1254.89	533.145	CF_3 Asymmetric Stretching
1271.12	36.907	C–C Stretching, CF_3 Wagging
1284.95	40.870	C–C Stretching, CF_3 Wagging
1310.55	25.624	C–C Stretching, CF_3 Wagging

Appendix B

Supplementary Information for "Calcium Bridging Drives Polysaccharide Co-Adsorption to a Proxy Sea Surface Microlayer"

B.1 Mean Molecular Area Data

Mean molecular area (MMA) data of the d_{31}-palmitic acid and d_{33}-hexadecanol monolayers measured at constant surface pressure are tabulated below. Alginate consistently expands the monolayer relative to the salt water subphase, and the magnitude of monolayer expansion is greater at 5 mN/m than at 25 mN/m. Enhanced dispersion interactions between the lipid alkyl chains and increased exchange interactions likely push alginate out of the plane of the compressed monolayer.

Table B.1: Average mean molecular area values (Å^2/molecule) and one standard deviation from the mean (σ, Å^2/molecule) of d_{31}-palmitic acid (d_{31}-PA) and d_{33}-cetyl alcohol (d_{33}-CA) monolayers measured at constant surface pressures 5 mN/m and 25 mN/m.

Monolayer & Subphase	**5 mN/m**		**25 mN/m**	
	MMA	σ	**MMA**	σ
d_{31}-PA, 0.47 M NaCl, pH 8.2	22.66	0.29	20.57	0.33
d_{31}-PA, Alg[a], 0.47 M NaCl, pH 8.2	25.48	0.44	21.50	0.44
d_{31}-PA, 0.47 M NaCl, 10 mM $CaCl_2$, pH 8.2	22.36	0.16	20.92	0.11
d_{31}-PA, Alg[a], 0.47 M NaCl, 10 mM $CaCl_2$, pH 8.2	23.27	0.65	21.56	0.32
d_{31}-PA, 0.47 M NaCl, 10 mM $CaCl_2$, pH 5.8	25.21	0.24	22.67	0.20
d_{31}-PA, Alg[a], 0.47 M NaCl, 10 mM $CaCl_2$, pH 5.8	27.29	0.48	22.99	0.92
d_{33}-CA, 0.47 M NaCl, 10 mM $CaCl_2$, pH 8.2	20.62	0.15	17.85	0.09
d_{33}-CA, Alg[a], 0.47 M NaCl, 10 mM $CaCl_2$, pH 8.2	21.91	0.08	18.72	0.05
d_{31}-PA, 0.47 M NaCl, 10 mM $MgCl_2$, pH 8.2	24.27	0.04	21.40	0.14
d_{31}-PA, Alg[a], 0.47 M NaCl, 10 mM $MgCl_2$, pH 8.2	26.51	0.13	22.08	0.17
d_{31}-PA, 0.47 M NaCl, 53 mM $MgCl_2$, pH 8.2	24.17	0.10	21.80	0.09
d_{31}-PA, Alg[a], 0.47 M NaCl, 53 mM $MgCl_2$, pH 8.2	27.06	0.43	22.86	0.27

[a]50 ppm Alginate

Table B.2: The ratio of d_{31}-palmitic acid (d_{31}-PA) and d_{33}-cetyl alcohol (d_{33}-CA) MMA values ($R_{\mathrm{Alg/SW}}$) and propagated error (σ_{E}) corresponding to the 50 ppm alginate subphase MMA divided by the seawater subphase MMA.

Monolayer & Subphase	**5 mN/m**		**25 mN/m**	
	$R_{\mathbf{Alg/SW}}$	$\sigma_{\mathbf{E}}$	$R_{\mathbf{Alg/SW}}$	$\sigma_{\mathbf{E}}$
d_{31}-PA, 0.47 M NaCl, pH 8.2	1.124	0.022	1.045	0.026
d_{31}-PA, 0.47 M NaCl, 10 mM $CaCl_2$, pH 8.2	1.041	0.029	1.030	0.016
d_{31}-PA, 0.47 M NaCl, 10 mM $CaCl_2$, pH 5.8	1.083	0.020	1.014	0.041
d_{33}-CA, 0.47 M NaCl, 10 mM $CaCl_2$, pH 8.2	1.062	0.008	1.049	0.005
d_{31}-PA, 0.47 M NaCl, 10 mM $MgCl_2$, pH 8.2	1.092	0.005	1.032	0.010
d_{31}-PA, 0.47 M NaCl, 53 mM $MgCl_2$, pH 8.2	1.120	0.017	1.048	0.012

B.2 Vibrational Frequency Calculations

To distinguish between peaks corresponding to the d_{31}-palmitic acid monolayer or the co-adsorbed alginate, harmonic vibrational frequency calculations were performed using Q-Chem v. 5.3.1.[290] D-guluronic acid, an alginate monomer primarily responsible for cation binding, was selected to model the alginate vibrational modes (Fig. B.1a).[330,333,334] Both protonated d_{31}-palmitic acid (Fig. B.1b) and deprotonated d_{31}-palmitate (Fig. B.1c) were modeled, and the atomic mass of 2.01410 was used for the deuterium atoms.[370] Geometry optimization and harmonic frequency analysis were performed at the EDF2/6-31+G* level of theory.[289] Frequencies, intensities, and vibrational mode assignments within the frequency region of the carboxylic acid headgroup and the C–D bending modes (1090-1850 cm^{-1}) are tabulated in Tables B.3-B.5.

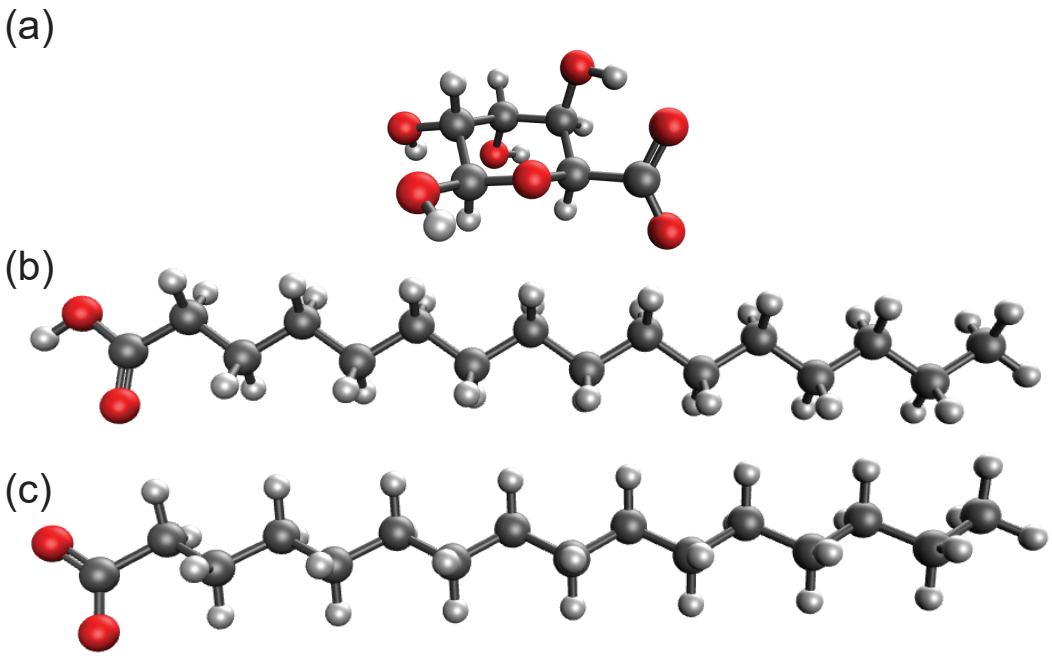

Figure B.1: Geometry optimized structures of **(a)** D-guluronate, **(b)** d_{31}-palmitic acid, and **(c)** d_{31}-palmitate.

Table B.3: Harmonic vibrational frequencies (ω), intensities, and vibrational mode assignments of D-guluronate.

ω **(cm^{-1})**	**Intensity (km/mol)**	**Mode Assignments**
1094.24	111.741	C-O-H Bending, C-O-C Stretching
1100.50	145.998	C-OH Stretching
1116.31	80.623	C-O-C Stretching, C-O-H Bending
1148.48	211.874	C-O-H Stretching, C-H Wagging
1154.90	2.637	C-O-H Stretching and Bending
1206.32	34.863	C-O-H Bending, C-H Wagging
1242.62	32.793	C-H Wagging, C-O-H Bending
1264.93	32.675	C-H Wagging, C-O-H Bending
1297.55	18.810	C-H Wagging, C-O-H Bending
1317.06	32.035	C-H Wagging, C-O-H Bending
1325.07	15.798	C-H Wagging, C-O-H Bending
1340.30	18.708	C-H Wagging, C-O-H Bending
1352.16	121.662	C-H Wagging, C-O-H Bending, COO^- Symmetric Stretching
1356.34	27.790	C-H Wagging, C-O-H Bending, COO^- Symmetric Stretching
1391.73	127.213	COO^- Symmetric Stretching, C-H Wagging
1400.35	16.914	C-H Wagging, C-O-H Bending
1411.78	25.561	C-O-H Bending, C-H Wagging
1439.87	44.051	C-O-H Bending, C-H Wagging
1474.40	2.861	C-O-H Bending, C-H Wagging
1547.29	384.253	C-O-H Bending, COO^- Asymmetric Stretching
1725.18	423.674	COO^- Asymmetric Stretching, C-O-H Bending

Table B.4: Harmonic vibrational frequencies ω, intensities, and vibrational mode assignments of d_{31}-palmitic acid.

ω (cm^{-1})	**Intensity (km/mol)**	**Mode Assignments**
1092.09	0.403	CD_3 Bending, CD_2 Bending & Wagging
1093.01	4.856	CD_3 Bending
1093.67	7.022	CD_2 Bending
1108.35	13.932	CD_2 Bending & Wagging, CD_3 Bending
1116.04	2.674	CD_2 Bending & Wagging
1117.22	0.663	CD_2 Bending & Wagging
1119.12	0.914	CD_2 Bending & Wagging
1121.34	0.634	CD_2 Bending
1123.82	1.570	CD_2 Bending
1125.90	0.640	CD_2 Bending
1127.50	11.375	CD_2 Bending
1128.73	8.575	CD_2 Bending, CD_3 Bending
1132.35	1.303	CD_2 Bending & Wagging, CD_3 Bending
1141.51	14.964	CD_2 Bending, C-O-H Bending & Stretching
1150.56	15.657	CD_2 Bending & Wagging, C-O-H Bending & Stretching
1159.16	46.521	C-O-H Bending & Stretching, CD_2 Bending & Wagging
1167.89	4.210	CD_2 Bending & Wagging, C-O-H Bending & Stretching
1177.22	4.233	CD_2 Bending, C-O-H Bending & Stretching
1189.07	65.964	C-O-H Bending & Stretching, CD_2 Wagging
1216.54	59.856	C-O-H Bending & Stretching, CD_2 Wagging
1241.05	15.368	CD_2 Wagging, C-O-H Bending
1260.91	6.855	CD_2 Wagging, C-O-H Bending
1274.81	0.569	CD_2 Wagging, C-O-H Bending
1282.93	0.528	CD_2 Wagging, C-O-H Bending
1286.54	0.032	CD_2 Wagging, C-O-H Bending
1288.46	0.160	CD_2 Wagging, C-O-H Bending
1369.64	120.711	C-O-H Bending & Stretching
1827.90	299.335	C=O Stretching, C-O-H Bending

Table B.5: Harmonic vibrational frequencies (ω), intensities, and vibrational mode assignments of d_{31}-palmitate.

ω (cm^{-1})	Intensity (km/mol)	Mode Assignments
1091.89	7.209	CD_3 Bending, CD_2 Bending & Wagging
1092.92	4.719	CD_3 Bending
1093.94	5.964	CD_2 Bending & Wagging, CD_3 Bending
1108.52	0.333	CD_2 Bending & Wagging, CD_3 Bending
1114.79	0.338	CD_2 Bending & Wagging
1116.53	0.014	CD_2 Bending & Wagging
1118.41	0.561	CD_2 Bending & Wagging, CD_3 Bending
1120.73	0.006	CD_2 Bending & Wagging, CD_3 Bending
1123.15	1.640	CD_2 Bending, CD_3 Bending
1125.37	0.002	CD_2 Bending, CD_3 Bending
1127.13	10.458	CD_2 Bending
1127.55	0.296	CD_2 Bending, CD_3 Bending
1131.37	0.628	CD_2 Bending & Wagging, CD_3 Bending
1140.96	0.701	CD_2 Bending & Wagging, CD_3 Bending
1149.66	0.109	CD_2 Bending & Wagging
1162.08	2.876	CD_2 Bending & Wagging, CD_3 Bending
1167.45	0.477	CD_2 Bending & Wagging, CD_3 Bending
1177.28	0.702	CD_2 Bending, CD_3 Bending
1198.48	0.953	CD_2 Bending & Wagging, CD_3 Bending
1228.77	0.582	CD_2 Bending & Wagging, CD_3 Bending
1250.96	1.753	CD_2 Wagging, CD_3 Bending
1265.36	0.348	CD_2 Wagging, CD_3 Bending
1275.19	0.701	CD_2 Wagging, CD_3 Bending
1281.76	0.054	CD_2 Wagging
1285.41	0.085	CD_2 Wagging
1371.58	328.038	COO^- Symmetric Stretching
1678.00	637.505	COO^- Asymmetric Stretching

B.3 Carboxylate Region Spectral Fitting

Peaks within the COOH stretching region (1150-1850 cm^{-1}) were fitted to Gaussian functions using OriginPro 9.0. The software uses the Levenberg-Marquardt algorithm to perform the nonlinear curve fitting routine. Eight points were placed along the baseline, and a 4^{th}-order polynomial function was fitted to those points and used to define the spectral baseline. Peak fitting parameters were not fixed.

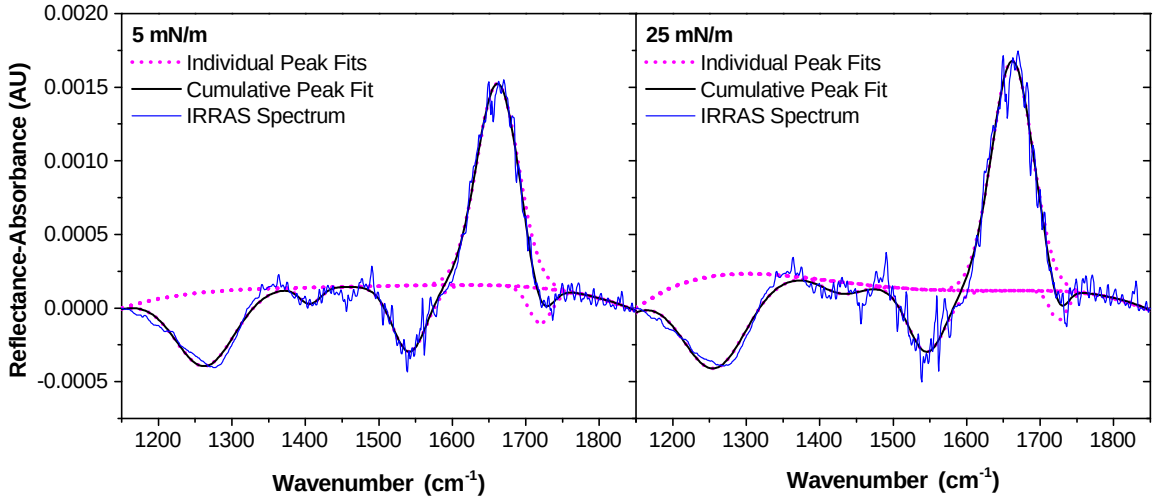

Figure B.2: IRRAS spectra and corresponding peak fits of a d_{31}-palmitic acid monolayer at 5 mN/m (left) and 25 mN/m (right) spread onto an aqueous subphase of 0.47 M NaCl at pH 8.2.

Table B.6: Center frequencies (ω, cm^{-1}), reflectance-absorbance intensities (Int.), peak areas, and full width at half maximum (FWHM, cm^{-1}) values of Gaussian fits to IRRAS spectra in the COOH vibrational mode region of a d_{31}-palmitic acid monolayer (5 mN/m and 25 mN/m) spread onto an aqueous subphase of 0.47 M NaCl at pH 8.2.

Mode	5 mN/m				25 mN/m			
	ω	Int.	Area	FWHM	ω	Int.	Area	FWHM
ν C-OH	1263.5	-5.02E-4	0.0501	93.7	1256.7	-6.31E-4	0.06895	102.7
ν_S CO_2^-	1406.3	-1.10E-4	0.00399	34.0	1429.7	-7.92E-5	0.00509	60.4
ν_{AS} CO_2^-	1541.6	-4.49E-4	0.0261	54.5	1545.6	-4.23E-4	0.0263	58.4
δ H-O-H	1661.5	0.00137	0.0975	66.9	1662.0	0.00156	0.109	66.0
ν C=O	1719.6	-2.40E-4	0.00942	36.8	1725.1	-1.96E-4	0.00586	28.1

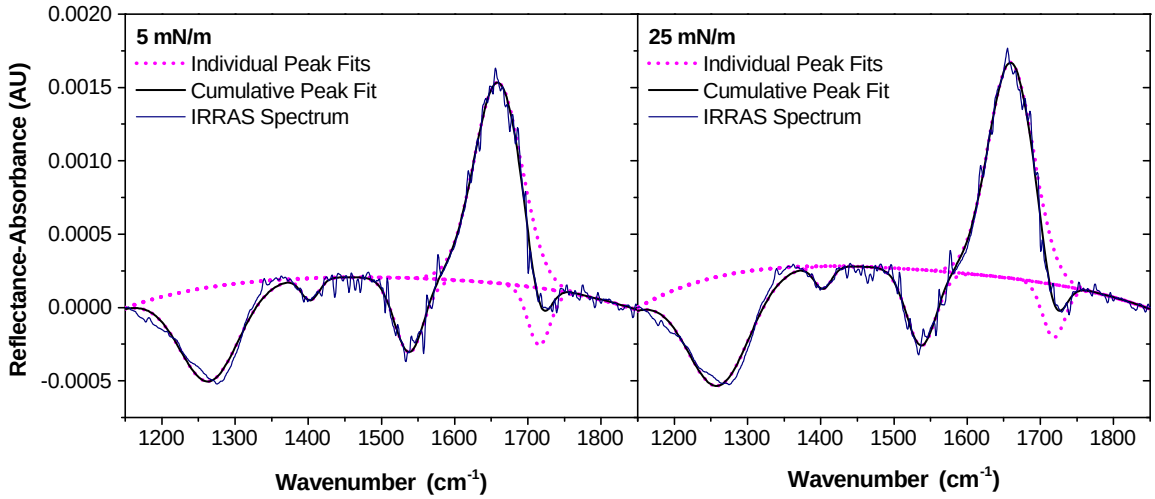

Figure B.3: IRRAS spectra and corresponding peak fits of a d_{31}-palmitic acid monolayer at 5 mN/m (left) and 25 mN/m (right) spread onto an aqueous subphase of 0.47 M NaCl and 50 ppm alginate at pH 8.2.

Table B.7: Center frequencies (ω, cm^{-1}), reflectance-absorbance intensities (Int.), peak areas, and full width at half maximum (FWHM, cm^{-1}) values of Gaussian fits to IRRAS spectra in the COOH vibrational mode region of a d_{31}-palmitic acid monolayer (5 mN/m and 25 mN/m) spread onto an aqueous subphase of 0.47 M NaCl and 50 ppm alginate at pH 8.2.

Mode	**5 mN/m**				**25 mN/m**			
	ω	**Int.**	**Area**	**FWHM**	ω	**Int.**	**Area**	**FWHM**
ν C-OH	1264.7	-6.42E-4	0.0643	94.1	1260.5	-7.46E-4	0.0789	99.3
ν_S CO_2^-	1402.6	-1.50E-4	0.00458	28.7	1402.9	-1.53E-4	0.00461	28.3
ν_{AS} CO_2^-	1537.8	-5.07E-4	0.0253	46.9	1537.3	-5.16E-4	0.0260	47.3
δ H-O-H	1658.9	0.00137	0.111	76.2	1659.6	0.00147	0.114	72.6
ν C=O	1715.4	-3.88E-4	0.0149	35.9	1718.3	-3.62E-4	0.0139	36.0

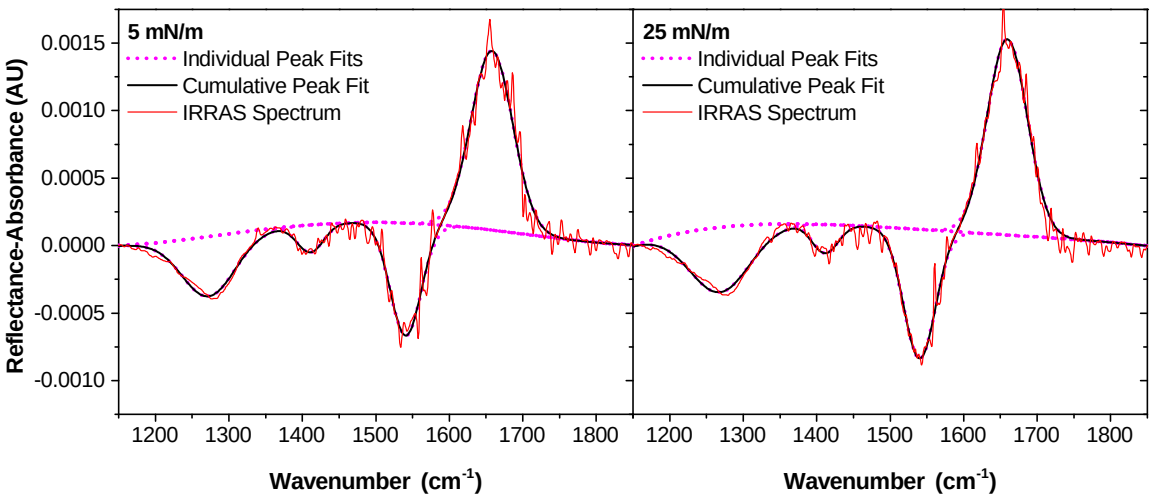

Figure B.4: IRRAS spectra and corresponding peak fits of a d_{31}-palmitic acid monolayer at 5 mN/m (left) and 25 mN/m (right) spread onto an aqueous subphase of 0.47 M NaCl and 10 mM $CaCl_2$ at pH 8.2.

Table B.8: Center frequencies (ω, cm^{-1}), reflectance-absorbance intensities (Int.), peak areas, and full width at half maximum (FWHM, cm^{-1}) values of Gaussian fits to IRRAS spectra in the COOH vibrational mode region of a d_{31}-palmitic acid monolayer (5 mN/m and 25 mN/m) spread onto an aqueous subphase of 0.47 M NaCl and 10 mM $CaCl_2$ at pH 8.2.

Mode	**5 mN/m**				**25 mN/m**			
	ω	**Int.**	**Area**	**FWHM**	ω	**Int.**	**Area**	**FWHM**
ν C-OH	1272.6	-4.42E-4	0.0401	85.0	1268.2	-4.81E-4	0.0497	97.1
ν_S CO_2^-	1410.8	-2.03E-4	0.00908	41.9	1411.5	-2.12E-4	0.00933	41.3
ν_{AS} CO_2^-	1540.6	-8.35E-4	0.0439	49.4	1539.9	-9.57E-4	0.0515	50.6
δ H-O-H	1658.0	0.00133	0.0946	67.0	1659.5	0.00145	0.0994	64.4

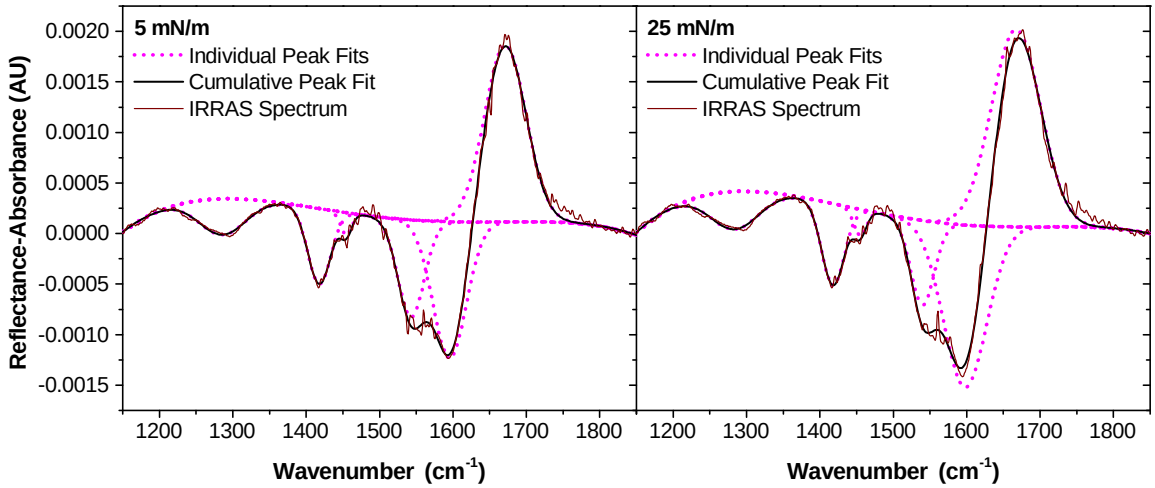

Figure B.5: IRRAS spectra and corresponding peak fits of a d_{31}-palmitic acid monolayer at 5 mN/m (left) and 25 mN/m (right) spread onto an aqueous subphase of 0.47 M NaCl, 10 mM $CaCl_2$, and 50 ppm alginate at pH 8.2.

Table B.9: Center frequencies (ω, cm^{-1}), reflectance-absorbance intensities (Int.), peak areas, and full width at half maximum (FWHM, cm^{-1}) values of Gaussian fits to IRRAS spectra in the COOH vibrational mode region of a d_{31}-palmitic acid monolayer (5 mN/m and 25 mN/m) spread onto an aqueous subphase of 0.47 M NaCl, 10 mM $CaCl_2$, and 50 ppm alginate at pH 8.2.

Mode	**5 mN/m**				**25 mN/m**			
	ω	**Int.**	**Area**	**FWHM**	ω	**Int.**	**Area**	**FWHM**
ν C-OH	1285.7	-3.58E-4	0.0291	76.3	1283.5	-3.77E-4	0.0318	79.2
ν_S CO_2^- (d_{31}-PA)	1417.8	-7.45E-4	0.0293	36.9	1417.8	-8.07E-4	0.0314	36.5
ν_S CO_2^- (Alg)	1454.3	-2.16E-4	0.00415	18.0	1454.7	-2.54E-4	0.00558	20.7
ν_{AS} CO_2^- (d_{31}-PA)	1543.0	9.58E-4	0.0432	42.3	1539.8	-8.34E-4	0.0336	37.9
ν_{AS} CO_2^- (Alg)	1595.4	0.00135	0.0768	53.6	1597.9	-0.00160	0.118	69.0
δ H-O-H	1671.3	0.00174	0.124	66.6	1667.3	0.00195	0.164	79.0

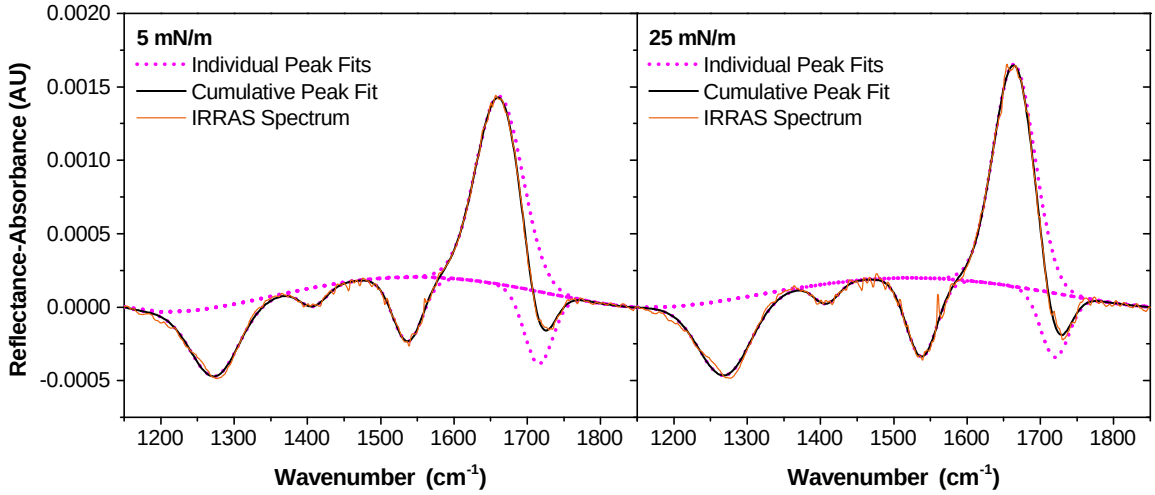

Figure B.6: IRRAS spectra and corresponding peak fits of a d_{31}-palmitic acid monolayer at 5 mN/m (left) and 25 mN/m (right) spread onto an aqueous subphase of 0.47 M NaCl and 10 mM $CaCl_2$ at pH 5.8.

Table B.10: Center frequencies (ω, cm^{-1}), reflectance-absorbance intensities (Int.), peak areas, and full width at half maximum (FWHM, cm^{-1}) values of Gaussian fits to IRRAS spectra in the COOH vibrational mode region of a d_{31}-palmitic acid monolayer (5 mN/m and 25 mN/m) spread onto an aqueous subphase of 0.47 M NaCl and 10 mM $CaCl_2$ at pH 5.8.

Mode	**5 mN/m**				**25 mN/m**			
	ω	**Int.**	**Area**	**FWHM**	ω	**Int.**	**Area**	**FWHM**
ν C-OH	1274.0	-4.67E-4	0.0377	75.8	1269.6	-5.11E-4	0.0448	82.4
ν_S CO_2^-	1408.2	-1.27E-4	0.00570	42.0	1407.9	-1.36E-4	0.00563	38.9
ν_{AS} CO_2^-	1536.9	-4.40E-4	0.0225	48.0	1538.0	-5.36E-4	0.0281	49.2
δ H-O-H	1661.6	0.00128	0.102	74.9	1664.1	0.00151	0.107	66.8
ν C=O	1715.2	-4.91E-4	0.0239	45.8	1719.7	-4.36E-4	0.0209	45.0

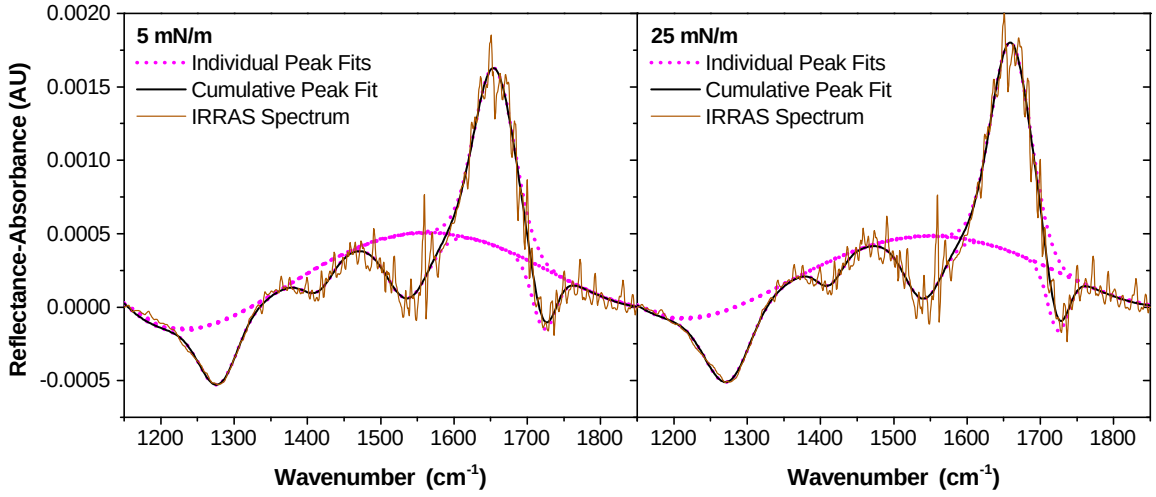

Figure B.7: IRRAS spectra and corresponding peak fits of a d_{31}-palmitic acid monolayer at 5 mN/m (left) and 25 mN/m (right) spread onto an aqueous subphase of 0.47 M NaCl, 10 mM $CaCl_2$, and 50 ppm alginate at pH 5.8.

Table B.11: Center frequencies (ω, cm^{-1}), reflectance-absorbance intensities (Int.), peak areas, and full width at half maximum (FWHM, cm^{-1}) values of Gaussian fits to IRRAS spectra in the COOH vibrational mode region of a d_{31}-palmitic acid monolayer (5 mN/m and 25 mN/m) spread onto an aqueous subphase of 0.47 M NaCl, 10 mM $CaCl_2$, and 50 ppm alginate at pH 5.8.

Mode	**5 mN/m**				**25 mN/m**			
	ω	**Int.**	**Area**	**FWHM**	ω	**RA Int.**	**Area**	**FWHM**
ν C-OH	1278.6	-4.18E-4	0.0264	59.2	1273.6	-4.86E-4	0.0363	70.1
ν_S CO_2^-	1414.3	-1.67E-4	0.00834	46.8	1412.1	-1.65E-4	0.00689	39.2
ν_{AS} CO_2^-	1536.8	-4.42E-4	0.0314	66.8	1540.6	-4.29E-4	0.0280	61.3
δ H-O-H	1654.9	0.00121	0.0829	64.6	1659.8	0.00142	0.0969	64.0
ν C=O	1722.6	-4.12E-4	0.0162	37.0	1724.1	-4.00E-4	0.0142	33.4

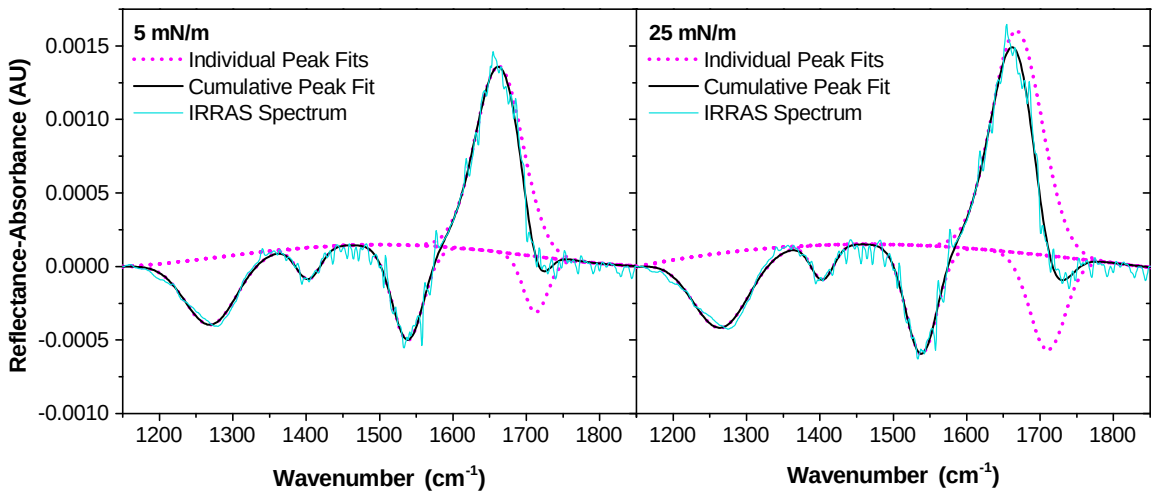

Figure B.8: IRRAS spectra and corresponding peak fits of a d_{31}-palmitic acid monolayer at 5 mN/m (left) and 25 mN/m (right) spread onto an aqueous subphase of 0.47 M NaCl and 10 mM $MgCl_2$ at pH 8.2.

Table B.12: Center frequencies (ω, cm^{-1}), reflectance-absorbance intensities (Int.), peak areas, and full width at half maximum (FWHM, cm^{-1}) values of Gaussian fits to IRRAS spectra in the COOH vibrational mode region of a d_{31}-palmitic acid monolayer (5 mN/m and 25 mN/m) spread onto an aqueous subphase of 0.47 M NaCl and 10 mM $MgCl_2$ at pH 8.2.

Mode	**5 mN/m**				**25 mN/m**			
	ω	**Int.**	**Area**	**FWHM**	ω	**Int.**	**Area**	**FWHM**
ν C-OH	1270.3	-4.53E-4	0.0398	82.6	1265.3	-5.08E-4	0.0484	89.4
ν_S CO_2^-	1403.0	-2.15E-4	0.00888	38.8	1403.3	-2.36E-4	0.00911	36.3
ν_{AS} CO_2^-	1538.4	-6.46E-4	0.0347	50.5	1538.2	-7.39E-4	0.0393	49.9
δ H-O-H	1662.6	0.00126	0.102	75.9	1668.1	0.00151	0.130	80.9
ν C=O	1712.6	-3.79E-4	0.0159	39.5	1710.1	-6.41E-4	0.0388	56.8

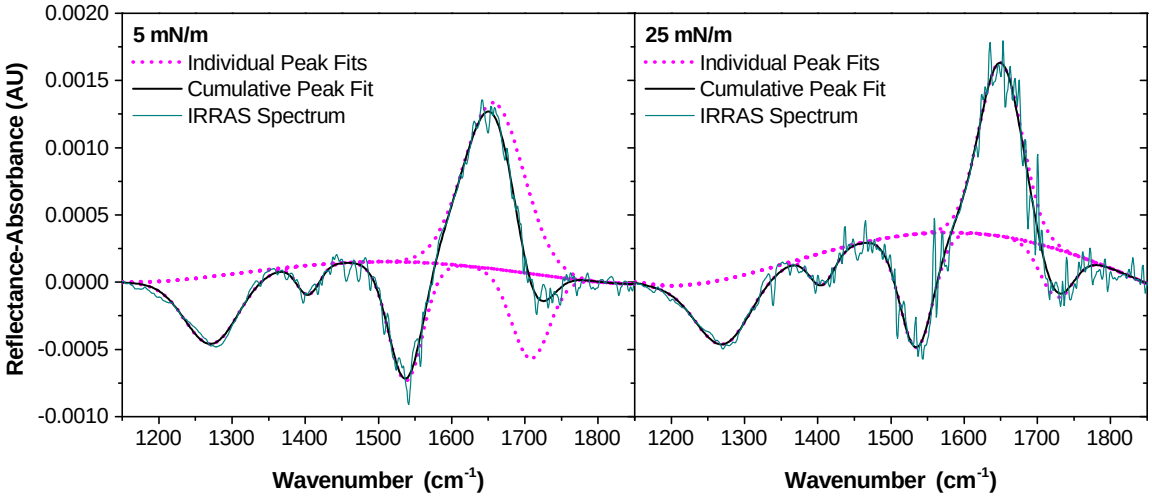

Figure B.9: IRRAS spectra and corresponding peak fits of a d_{31}-palmitic acid monolayer at 5 mN/m (left) and 25 mN/m (right) spread onto an aqueous subphase of 0.47 M NaCl, 10 mM $MgCl_2$, and 50 ppm alginate at pH 8.2.

Table B.13: Center frequencies (ω, cm^{-1}), reflectance-absorbance intensities (Int.), peak areas, and full width at half maximum (FWHM, cm^{-1}) values of Gaussian fits to IRRAS spectra in the COOH vibrational mode region of a d_{31}-palmitic acid monolayer (5 mN/m and 25 mN/m) spread onto an aqueous subphase of 0.47 M NaCl, 10 mM $MgCl_2$, and 50 ppm alginate at pH 8.2.

Mode	**5 mN/m**				**25 mN/m**			
	ω	**Int.**	**Area**	**FWHM**	ω	**Int.**	**Area**	**FWHM**
ν C-OH	1272.1	-4.99E-4	0.0455	85.5	1271.4	-4.78E-4	0.0439	86.2
ν_S CO_2^-	1404.0	-2.19E-4	0.00840	36.1	1405.7	-2.40E-4	0.0101	39.6
ν_{AS} CO_2^-	1537.3	-8.85E-4	0.0512	54.4	1534.9	-8.45E-4	0.0478	53.2
δ H-O-H	1657.2	0.00123	0.126	96.2	1649.7	0.00129	0.0944	68.7
ν C=O	1707.7	-6.31E-4	0.0405	60.3	1726.2	-3.58E-4	0.0200	52.4

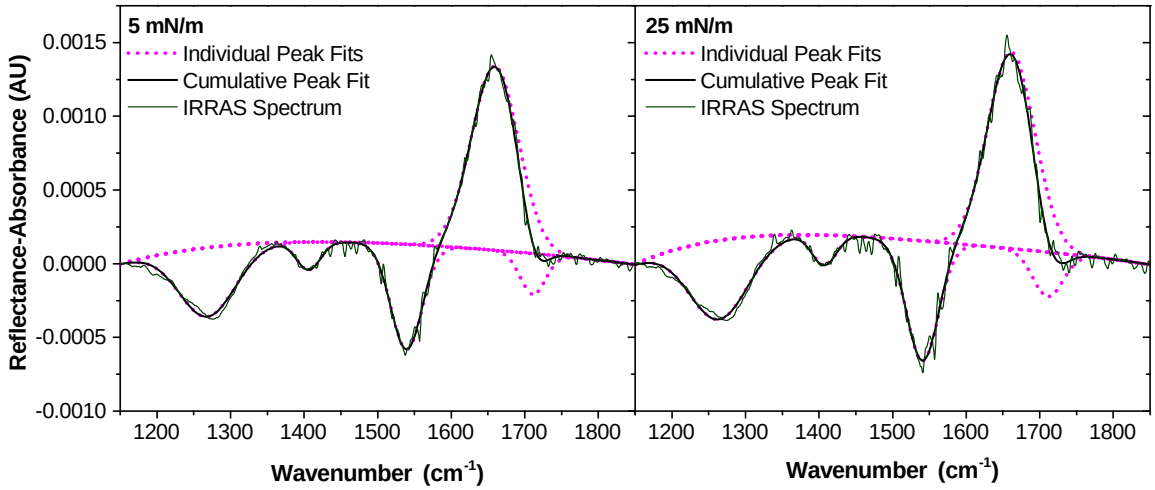

Figure B.10: IRRAS spectra and corresponding peak fits of a d_{31}-palmitic acid monolayer at 5 mN/m (left) and 25 mN/m (right) spread onto an aqueous subphase of 0.47 M NaCl and 53 mM $MgCl_2$ at pH 8.2.

Table B.14: Center frequencies (ω, cm^{-1}), reflectance-absorbance intensities (Int.), peak areas, and full width at half maximum (FWHM, cm^{-1}) values of Gaussian fits to IRRAS spectra in the COOH vibrational mode region of a d_{31}-palmitic acid monolayer (5 mN/m and 25 mN/m) spread onto an aqueous subphase of 0.47 M NaCl and 53 mM $MgCl_2$ at pH 8.2.

Mode	**5 mN/m**				**25 mN/m**			
	ω	**Int.**	**Area**	**FWHM**	ω	**Int.**	**Area**	**FWHM**
ν C-OH	1268.6	-4.69E-4	0.0447	89.6	1264.1	-5.37E-4	0.0543	95.1
ν_S CO_2^-	1406.0	-1.89E-4	0.00768	38.1	1406.8	-2.05E-4	0.00834	38.3
ν_{AS} CO_2^-	1539.3	-7.13E-4	0.0381	50.1	1540.6	-8.13E-4	0.0445	51.4
δ H-O-H	1659.5	0.00125	0.100	75.6	1661.1	0.00133	0.107	75.4
ν C=O	1711.0	-2.77E-4	0.0119	40.4	1711.1	-3.01E-4	0.0154	48.2

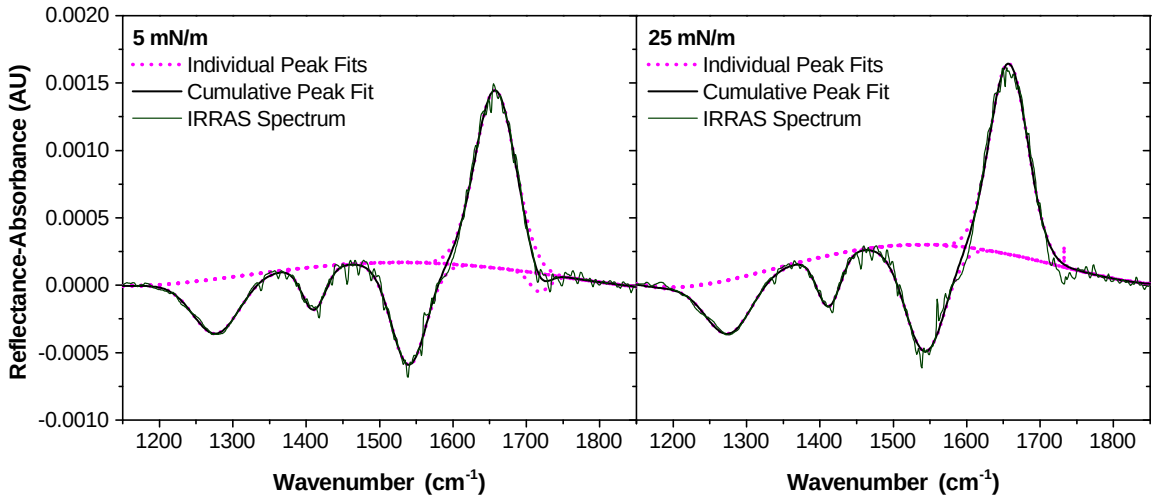

Figure B.11: IRRAS spectra and corresponding peak fits of a d_{31}-palmitic acid monolayer at 5 mN/m (left) and 25 mN/m (right) spread onto an aqueous subphase of 0.47 M NaCl, 53 mM $MgCl_2$, and 50 ppm alginate at pH 8.2.

Table B.15: Center frequencies (ω, cm^{-1}), reflectance-absorbance intensities (Int.), peak areas, and full width at half maximum (FWHM, cm^{-1}) values of Gaussian fits to IRRAS spectra in the COOH vibrational mode region of a d_{31}-palmitic acid monolayer (5 mN/m and 25 mN/m) spread onto an aqueous subphase of 0.47 M NaCl, 53 mM $MgCl_2$, and 50 ppm alginate at pH 8.2.

Mode	5 mN/m				25 mN/m			
	ω	Int.	Area	FWHM	ω	Int.	Area	FWHM
ν C-OH	1277.5	-4.05E-4	0.0322	74.7	1276.1	-3.97E-4	0.0308	72.9
ν_S CO_2^-	1410.3	-3.18E-4	0.0126	37.1	1412.1	-3.80E-4	0.0150	37.2
ν_{AS} CO_2^-	1539.9	-7.59E-4	0.0453	56.0	1543.5	-7.94E-4	0.0540	63.8
δ H-O-H	1657.6	0.00132	0.0910	64.9	1657.4	0.00141	0.0916	60.9
ν C=O	1717.7	-1.35E-4	0.00451	31.3	1732.6	1.60E-4	7.92E-7	0.00464

B.4 d_{33}-Cetyl Alcohol IRRAS Spectral Analysis

The carboxylic acid stretching region (1150-1850 cm^{-1}) was analyzed for the d_{33}-cetyl alcohol spectra to further examine the extent of alginate co-adsorption to the monolayer (Fig. B.12). Cetyl alcohol only exhibits the C-OH stretching mode, so any carboxylic acid peaks can be attributed to alginate co-adsorption. Neither the ν_S CO_2^-, ν_{AS} CO_2^-, nor the ν C=O stretches appear at either surface pressure, indicating no al-

ginate co-adsorption. The δ H-O-H mode red shifts in response to alginate within the aqueous subphase, possibly caused by alginate hydration within the probing region of IRRAS.

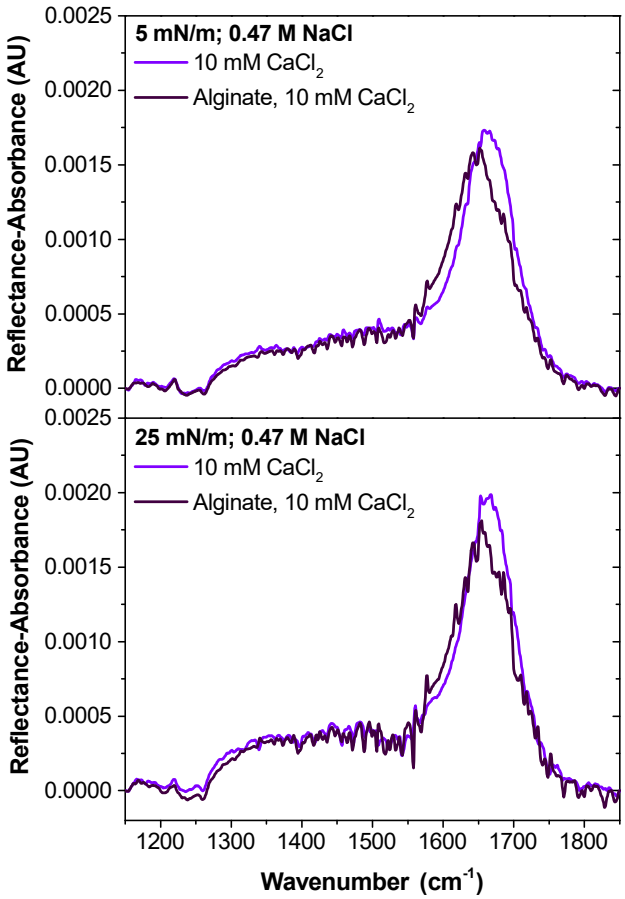

Figure B.12: IRRAS spectra of d_{33}-cetyl alcohol collected and analyzed within the COOH stretching region at constant surface pressures of 5 mN/m (top) and 25 mN/m (bottom). The light purple curves correspond to the monolayer spread onto a 0.47 M NaCl and 10 mM $CaCl_2$ subphase at pH 8.2. The dark purple curves correspond to the monolayer spread onto a 0.47 M NaCl, 10 mM $CaCl_2$, and 50 ppm alginate subphase. All spectra represent averages of at least triplicate measurements.

B.5 CD_2 Scissoring Mode Analysis

The CD_2 scissoring mode region (1070-1110 cm^{-1}) was analyzed using OriginPro 9.0. A baseline was fitted to a line between the two endpoints of the region, and then the baseline was subtracted from the spectrum. Following baseline subtraction, the

center frequency of the CD_2 scissoring mode was determined with the Peak Analyzer tool in Origin.

Table B.16: Center frequencies (cm^{-1}) of the IRRAS CD_2 scissoring (δ) mode of d_{31}-palmitic acid (d_{31}-PA) and d_{33}-cetyl alcohol (d_{33}-CA) monolayers measured at constant surface pressures 5 mN/m and 25 mN/m.

Monolayer & Subphase	δ **CD_2**	
	5 mN/m	**25 mN/m**
d_{31}-PA, 0.47 M NaCl, pH 8.2	1089.5	1089.0
d_{31}-PA, Alg, 0.47 M NaCl, pH 8.2	1089.5	1089.0
d_{31}-PA, 0.47 M NaCl, 10 mM $CaCl_2$, pH 8.2	1089.4	1089.4
d_{31}-PA, Alg, 0.47 M NaCl, 10 mM $CaCl_2$, pH 8.2	1089.4	1089.5
d_{31}-PA, 0.47 M NaCl, 10 mM $CaCl_2$, pH 5.8	1089.5	1089.5
d_{31}-PA, Alg, 0.47 M NaCl, 10 mM $CaCl_2$, pH 5.8	1089.5	1089.5
d_{33}-CA, 0.47 M NaCl, 10 mM $CaCl_2$, pH 8.2	1089.0	1089.0
d_{33}-CA, Alg, 0.47 M NaCl, 10 mM $CaCl_2$, pH 8.2	1089.0	1089.0
d_{31}-PA, 0.47 M NaCl, 10 mM $MgCl_2$, pH 8.2	1089.5	1089.0
d_{31}-PA, Alg, 0.47 M NaCl, 10 mM $MgCl_2$, pH 8.2	1089.5	1089.0
d_{31}-PA, 0.47 M NaCl, 53 mM $MgCl_2$, pH 8.2	1089.5	1089.0
d_{31}-PA, Alg, 0.47 M NaCl, 53 mM $MgCl_2$, pH 8.2	1089.5	1089.5